Mechanical strain influence on functional signaling of neurons in vitro

Doctoral Thesis

Submitted in partial fulfillment of the requirements for the degree of

Doctor rerum naturalium (Dr. rer. nat.)

to the

Mathematisch-Naturwissenschaftliche Fakultät

of the

Rheinische Friedrich-Wilhelms-Universität Bonn

By

Samar M. B. Tarazi

From

Gaza, Palestine

Bonn, October 2022

Prepared with the consent of the Faculty of Mathematics and Natural Sciences

1st referee: PD. Dr. Bernd Hoffmann

2nd referee: Prof. Dr. Jörg Höhfeld

Disputation: 08. February. 2023

Year of publication: 2023

Summary

Neuronal cells are embedded in the soft brain tissue and are protected by the thick meninges, as well as the rigid skull bones. Despite being highly sensitive and vastly protected, neurons are prone to internal and external mechanical forces. Many internal tensile loading scenarios affect neurons during development, growth and blood flow. Moreover, neurons are exposed to be strained externally by regular body movements or to be severely injured as a result of serious falls, accidents or tumor formation. In specific cases neuronal tissue could be dissected where intercellular connections get an entire cut and may cause cell death for some neurons in a network, such as the case of brain surgery to remove a tumor or to implant a neurostimulator device. However, limited experimental data is available for the mechanobiology of brain cells and it remained quite unattended.

Beside the chemical and molecular cues, some studies reported the importance of the mechanical input in nervous tissue homeostasis. Latest studies, show the key role of the physical microenvironment, such as topographical cues and stiffness alterations. Moreover, reports on physiological cyclic mechanical strain show the potential to accelerate axonal growth. While strain induced responses on the molecular and structural levels has been identified, much less is known about the consequences of these changes to neuronal functionality. As neurons are the basic functional units in transmitting information in the nervous system, the functional behavior of neurons under mechanical strain is the focus of this dissertation.

In the context of this thesis, primary cortical neurons were functionally characterized upon exposure to physiological and traumatic uniaxial stretch conditions within different developing stages. Also, spontaneous signaling events were characterized upon single cellular compartment loss induced by laser ablation. The dynamic changes in cells was determined by recording spatial and temporal changes in Ca^{2+} concentrations ($[Ca^{2+}]$) of single-cells and on synchronized network level using the Cal-590 AM Ca^{2+} indicator. The focus here is on both the immediate cell response and to their long-term adaptation to mechanical strain. This work shows that neurons are robust and can functionally tolerate cyclic stretching of up to 30% strain by keeping active communication between cells no matter if strain is applied at different periods during neuronal network formation. Simulating traumatic brain injuries using rapid stretch pulses identified a threshold for functional impairment of about 60% with a high ability to adapt and restore cellular connectivity with time. In spite of the broad range of assessed strains, cells keep maintained without further effects on cell viability, inflammatory responses or synapse formation. Co-cultures with astrocytes revealed more stable and better communicating networks while functional responses to strain remained unaffected.

Laser-induced death of single cellular compartment resulted in an increased intracellular calcium concentration [Ca^{2+}]i in neurons surrounding the ablated point. The [Ca^{2+}]i-increase was distance-dependent as closely connected neurons to the ablated cell were highly affected by Ca^{2+} inflow compared with other cells. Furthermore, the increased [Ca^{2+}]i caused a temporarily interruption in neuronal spiking activity that recovered gradually with time. In spite of the distance-dependent alterations, the overall network functionality was unaffected and the level of connectivity was maintained in the long-term analysis.

Taken together, this research work illustrates the internal dynamic responses of neurons to multiple loading conditions and to single-cell death. These data will be advantageous in developing more effective neuronal tolerance criteria to injury. Understanding and pushing the limits of nerve stretch holds tremendous potential for tissue engineering efforts to prevent nervous system injury and facilitate nerve repair.

Contents

Abbreviations

$[Ca^{2+}]i$	Intracellular calcium concentration
AM ester	acetoxymethyl ester
AP	Action potential
BSA	bovine serum albumin
CB	cytoskeletal buffer
CNS	central nervous system
CQ	Chloroquine
DIV	days in vitro
ECM	Extracellular matrix
FBS	fetal bovine serum
GFAP	glial fibrillary acidic protein
h	hour
HBSS	Hank's balanced salt solution
HEPES	4-(2-hydroxyethyl)-1-piperazineethanesulfonic acid
IL	interleukin
LSM	laser scanning microscopy
min	minutes

Pa	Pascal
PBS	phosphate-buffered saline
PDMS	Polydimethylsiloxane
PFA	Paraformaldehyde
PSD-95	Postsynaptic density protein 95
qPCR	qualitative real-time PCR
RT	room temperature
s	second
Syn	Synaptophysin
sync	synchrony
TBI	traumatic brain injury
TNF	tumor necrosis factor
Tuj1	neuron-specific class III beta-tubulin
UV	Ultraviolet

1 **Introduction**

Living systems are affected by many mechanical cues including stretch (Huang et al., 2013), stiffness (Blaschke et al., 2019) and topography (Baek et al., 2018) as illustrated in figure 1.1. Mechanical forces from the microenvironment surrounding the cells are transduced to intracellular signals. The process of mechanosensation can influence crucial biological activities such as proliferation, migration and even can have decisive consequences on differentiation (Engler et al., 2006). An early evidence that cells have elasticity-specific responses was provided by a study identifying that epithelial cells and fibroblasts on softer matrices were less spread, abnormally shaped and without focal adhesions (FA) (Pelham and Wang, 1997). Later, additional studies showed that stem cells were more willing to differentiate on surfaces with physiologically relevant rigidity for the specific cell type (McBeath et al., 2004; Venugopal et al., 2018). The rate of cell proliferation is also slowed on softer substrates, where stem cells cultured on collagen I-coated gels (250 Pa) had cell cycle halt and a decrease in DNA synthesis (Winer et al., 2008). In addition, topographic changes influence cell behavior and fate, where stem cells cultivated on 2 µm grooves differentiate into osteoblasts, and those cultured on wider grooves of 15 µm differentiate into adipocytes (Abagnale et al., 2015). The brain is also subjected to mechanical stimuli that can induce critical responses in vivo. For instance, alterations in substrate stiffness can change axonal length and branching of dendrites (Jiang et al., 2008).

Hence, not only biochemical signals and genetic factors (Kolodkin and Tessier-Lavigne, 2011; Tojima et al., 2011), but also the mechanical stimuli in the surrounding environment are recognized as controlling parameters for neuronal development and pathology (Franze et al., 2013; Estradaet al., 2021). A variety of local and global mechanical strains happens regularly in the brain during development and also due to pulsative deformations around the vasculature (Van Essen, 1997; Smith, 2009). Furthermore, the brain is exposed to other traumatic strains due to growing tumor mass, accidents and surgeries. In the next parts, some nervous tissue deformations due to physiological and pathological movements and their influence on cellular behavior are described in detail.

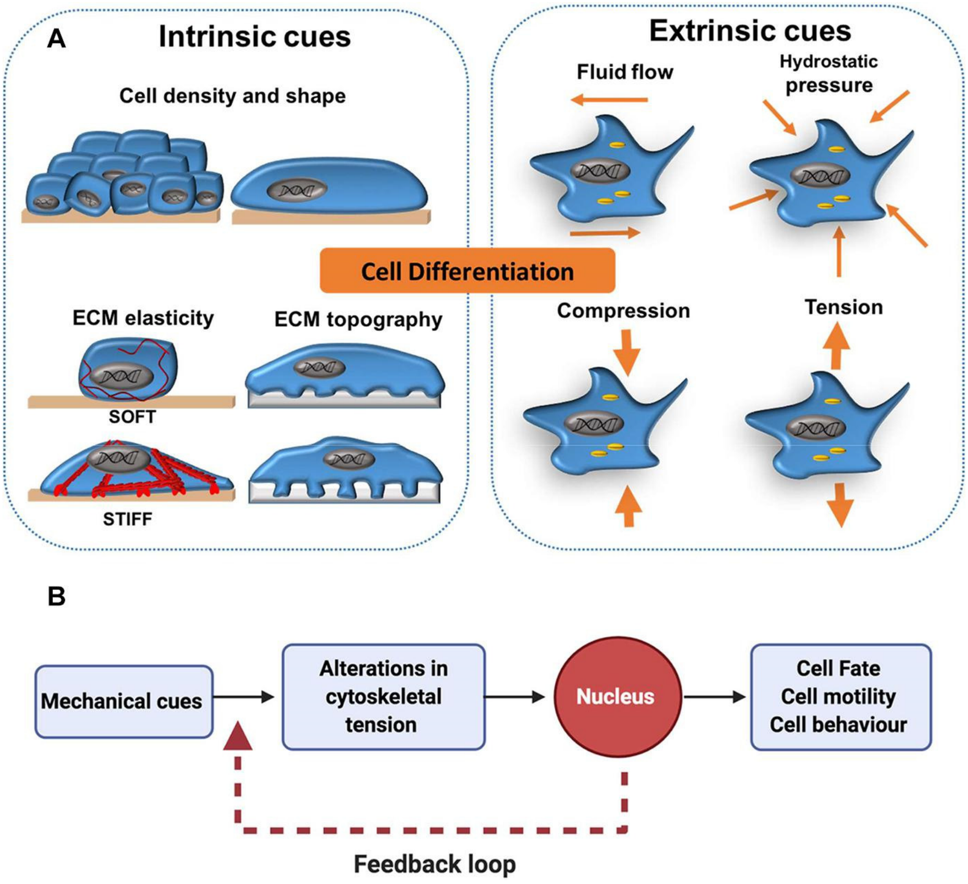

Figure 1.1 Internal and external mechanical cues in mechanotransduction
(A) Internal mechanical cues such as cell shape, density and elasticity of the extracellular matrix (ECM), as well as external mechanical forces such as shear stress induced by fluid flow has been shown to affect cell differentiation. (B) In general, the transmission of mechanical signals from the surface of the cell to the nucleus through the cytoskeleton activates a downstream signalling cascades. Subsequently, this can impact cellular decisions such as cell motility and cell fate. Additionally, a feedback loop enables cells to maintain a cytoskeletal stability that is responsive to alterations in their mechanical atmosphere. This image is taken from (Petzold and Gentleman, 2021).

1.1 Brain and mechanical forces

1.1.1 Mechanics during development

During development, the brain is affected by mechanical forces due to cortical folding (Van Essen, 1997). Due to the limited size in the skull, cortical layers fold to maximize the number of cells and reduce the space between them (Zilles et al., 2013). The main anatomic factors affecting the folding process are cortical stiffness, thickness and growth rate (Li et al., 2012). Low stiffness material is more susceptible to surface folding. The rapid growth in the nervous tissues of the brain causes mechanical tension along axons resulting in stretched axonal tracts that are already coupled to their target cell (Weiss, 1941). Similarly, in the peripheral nervous tissue, neurons grow by being stretched as a result of different growth degrees of bone and nervous tissue (Smith, 2009). Some extreme neuron stretch growth is found in the fast development of white matter tracts in the spine of blue whale, which expands at a speed of >3 cm per day. Likewise, giraffe's neck has a peak growth time when it's length increases by 2 cm per day (Dagg and Foster, 1982). This type of static mechanical tension along the axon has been shown to be an effective enhancer of neuronal growth as illustrated in figure 1.2 (Pfister et al., 2004). Despite of these findings, is still not well understood whether axons can maintain their function during extreme stretch-growth conditions.

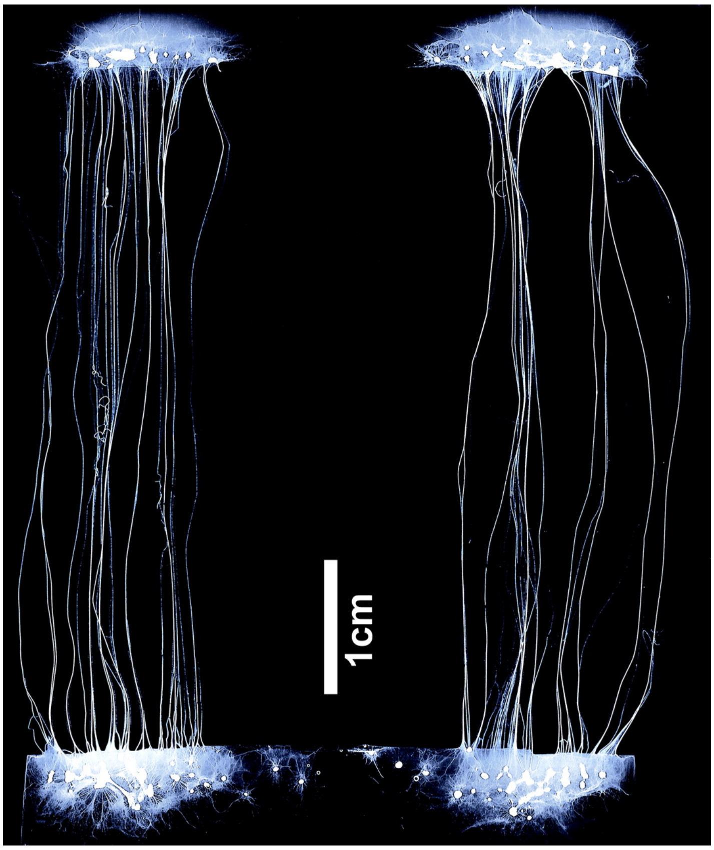

Figure 1.2 Stretch growth of axon tracts
Axon tracts, in the middle, connect two clusters of neurons, top and bottom. The axons bridging the two clusters were only ~100 µm long before the beginning of stretch growth. Gradually the cell populations were separated by applying mechanical tension on the axon tracts, causing a massive and fast axonal growth to 5 cm (colors are inverted to highlight axon tracts). Scale bar = 1 cm. Image taken from (Pfister et al., 2004).

1.1.2 Daily mechanical stimuli in the brain tissue

Blood flow across vascularized brain tissue causes continuous cyclic movements. This physiological tissue tension has an amplitude range of 2% when measured by magnetic resonance imaging (Wedeen and Ponceleti, 2007). Neural activity is able to significantly increase the deformation amplitude by changing blood flow and volume to a range of 30% as in cases of arterial dilatation in mice (Drew et al., 2011). Subsequently, these mechanical signals can be transduced by tension-derived structural modifications and changed binding affinities of proteins (Niediek et al., 2012), or by mechanically stimulated ion channels (Ranade et al., 2014).

Despite physiological brain stress, cells in the brain are exposed to regular mechanical strain by moving the brain's central mass as a result of the motion of the skull. Quick movements of the human body can generate mild accelerations that alter the brain matter with tension and compression levels of around 5% and up to 15% during extreme sportive activities (Bayly et al., 2005). There is an increased possibility of establishing a neurodegenerative diseases when these forces are happening repetitively due to initiating a mechanical memory after each extreme movement (Smith & Stewart, 2020).

1.1.3 Traumatic brain injury (TBI) and neurosurgery

TBI is a main public health problem and a major leading cause of death and disability (Dhandapani et al., 2012). More than 60 million new cases of TBI happen annually worldwide. Brain injury happens when an unexpected shock damages to the brain. Most traumatic injuries are caused by sport accidents, vehicle crashes and falls (Blennow et al., 2012). The impact of a TBI can range between mild, moderate, or severe, according to the degree of the damage to the brain. During severe injuries, brain cells experience tension, shear and compression. The destruction can be focal and concentrated to one area, or diffuse to more than one area of the brain. The most common and minor form of TBI is concussion, while the most severe type is diffuse axonal injury (DAI) which damages and disconnects some brain cells. The medical consequences associated with these injuries include dizziness, headache and loss of consciousness, in addition to deficiencies in motor skills, memory and attention (Alexander, 1995). Some symptoms could recover with time, but the microscale damage might continue and contribute to a future neurodegenerative disease (Johnson et al., 2013; McKee et al., 2009). In the past, several studies tried to determine the range of strain and strain frequencies causing TBI. In 1990, it has been hypothesized that DAI develop at shear strains of 10-50% and strain frequencies of around 10-50/s (Margulies et al., 1990). In vivo studies on tissue-level injury in the guinea pig optic nerve showed a threshold range of 0.13-0.34 for axonal injury (Bain and Meaney, 2000). Furthermore, studies in 2006 proposed that the brain cells are notably damaged at strains higher than 0.10 and strain rates above 10/s (Morrison et al., 2006).

Not only sudden accidents, but also some medical procedures cause damage to healthy cells in the brain (Travis et al., 2019). There are several types of operations in the brain or areas around it including craniotomy, biopsy, deep brain stimulation (DBS) and neuroendoscopy. Brain surgery is beneficial to treat different pathological conditions, such as tumors, blood clots, Parkinson's disease, and epilepsy. Latest developments of glioma surgery conclude that overall survival is improved by maximal tumor resection (Molinaro et al., 2020). Recent progressions in imaging technologies had minimized the probability of inducing new neurologic functional deficits in language and motor skills. However, patients continue to show some cognitive morbidity in higher-order functions after the operation restricting social life and integration back into the work (Drewes et al., 2018).

After primary brain cellular injury, some secondary consequences is caused by the physiologic reactions to the initial injury and start to evolve after hours to days from the time of the trauma. Some of these responses includes excitotoxicity, oxidative stress, demylination and neurodegeneration. Many cytokines are regulated and secreted after injury to stimulate an inflammatory response such as interleukin 6 (IL-6), the largest released quantities, interleukin 8 (IL-8) and tumor necrosis factor (TNFα) (Gopcevic et al., 2007; Lu et al., 2017). Additionally, a self-eating pathway, called autophagy and involved in degradation of proteins and organelles, could evolve to cope with various cellular stresses (Klionsky, 2007). LC3 is the most defined mammalian autophagy protein and has a critical role in initiation and construction of autophagosomes. Eventually, cell death can develop within the first hours and days by subcellular signaling causing neurological defects such as loss of neurological function, cognitive decline, psychological alterations and chronic disability (Maneshi and Hua, 2020).

1.2 Brain structure and injury

1.2.1 Head structure

The head consists of skull bones surrounding soft substances that are covered in a thin layer of fluid (Figure 1.3). The water-like fluid, called the cerebrospinal fluid, is believed to play a significant role in the shock-absorbing ability during external brain forces. The human brain is known to be the most developed mammalian brain with a mass of 1,500 g, where cerebral cortex represents over 80% of it (Herculano-Houzel, 2009). Cells in the brain are arranged into several specialized areas with different physiological functions. The mammalian cortex is constructed of an outer layer of gray matter, consisting mainly of cell bodies, and an inner center of white matter, containing mostly of axons (Wen and Chklovskii, 2005). Commonly, the external forces cause injuries at gray/white matter junctions, however, they are also detected in the deeper white matter of the cerebral cortex, brain stem, and corpus callosum (Taber et al., 2006).

1.2.2 Cellular composition of brain

The brain consists of two main cell types: neurons and glial cells, as illustrated in the zoom-in panel in figure 1.3. Adult brain with 86 billion neurons can form about 0.15 quadrillion connections (Herculano-Houzel, 2009). The major functions of neurons are processing, transmitting and storage of information. For this purpose, neurons have a unique cytoskeleton of processes that have an actin cortex surrounding bundled neurofilaments and microtubules. These processes, called neurites, can either grow to dendrites or an axon. The dendritic branches receive and incorporate synaptic signals, while axon transfer information from the soma to the next target cells.

The second major cell type is glial cells, of which astrocytes represent the most abundant fraction of cells in the adult brain besides oligodendrocytes, and microglial cells. In vivo, astrocytes have fine cellular extensions and thereby a spiky shape that start to develop during the first postnatal weeks (Farhy-Tselnicker and Allen, 2018). Astrocytes have a ‘housekeeping’ function since they give structural support for neurons, supply them with nutrients and maintain their tripartite synapses and neurotransmitter processing (Potokar et al., 2007). Besides, astrocytes regulate the blood flow and vascular diameter in CNS due to their close interaction with blood vessels (Iadecola & Nedergaard, 2007). Mechanical stability and reaction to mechanical cues are relying initially on the main cytoskeletal components actin microfilaments, intermediate filaments, and microtubules.

Cells always try to survive and adapt to physical changes by their elasticity and dynamic protein networks. Despite that astrocytes have a neuroprotective behavior during TBI, they also divide to form a glial scar around the injury site, which is preventing axonal regeneration.

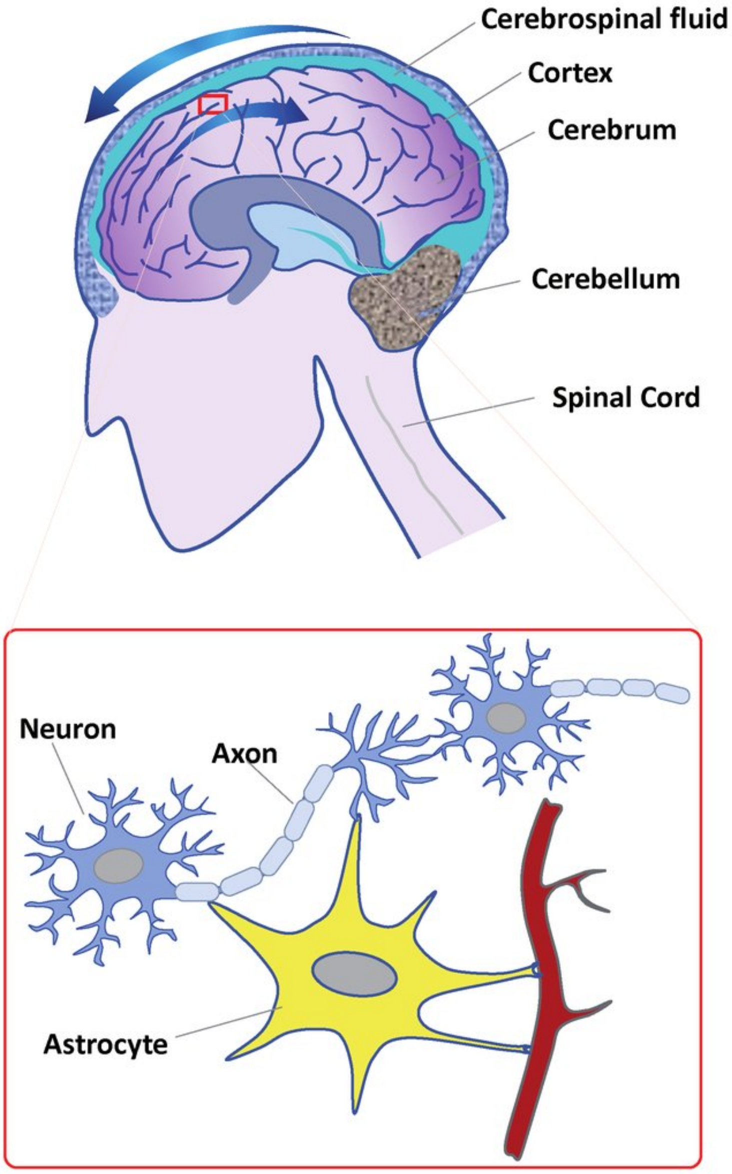

Figure 1.3 Schematic diagram of brain structure and main brain cells
An illustration of astrocyte cell connected to a both blood vessel and neurons. This figure is taken from (Maneshi and Hua, 2020).

1.3 Functional connectivity in brain and the reaction to strain

Neurons communicate through neural network formation that establish functional synapse (Colón-Ramos, 2009). Synapses regulate information flow in intercellular communication between cells of the nervous system. The functionality and connectivity of neural networks is influenced by when and where synapses are generated. Moreover, astrocytes are involved in neuronal functions and can control the number of synapses by secreting several neurotransmitters and expressing receptors for neuroactive substances (Christopherson et al., 2005). Astrocytes are interconnected by gap junctions that build multicellular networks and allow long-distance distribution of ions and metabolites (Sofroniew & Vinters, 2010). In vivo, the construction ratio of astrocytes to neurons is between 1:2 and 1:3 in the brain cortex (Herculano-Houzel, 2014); in which the combination of glial cells and neurons in networks is the center for information processing and plasticity in the brain (Araque and Navarrete, 2010; Fields and Stevens-Graham, 2002). Astrocytes and neurons are closely connected and have a coordinated activity that passes information waves through tripartite synapse (Rossi and Volterra, 2009). In adults, a single astrocyte is able to interact with around 2 million synapses at a time (Oberheim et al., 2009). The interaction between them is a bidirectional glutamatergic signaling in a Ca^{2+}-dependent process.

During brain injury, neurons propagate signals of mechanical forces to astrocytes and receive signals from them by Newton's third law. They can also transmit signals of damage by calcium waves, neurotransmitters and changed ion concentrations (Chen and Swanson, 2003). An elevation in intracellular calcium concentration is commonly detected in brain cells that have been exposed to mechanical strains despite of the force type (Weber et al., 2001). Upon physical insult, it is highly suggested that plasma membrane pores are a major route for Ca^{2+} access to cell. In vivo experiments and in vitro mechanical stretching showed an increase in neuronal membrane permeability (Pettus et al., 1994; McKinney et al., 1996), as well as instability in membrane proteins such as voltage-gated Na^+ channels (Shcherbatko et al., 1999). The increased accumulation of Na^+ in the cell leads to reverse-operation of Na^+/Ca^{2+} exchanger (Stys and Lopachin, 1998), as well as membrane depolarization, which could then activate VGCCs (Wolf et al., 2001). Depolarization of the membrane induce the release of neurotransmitters such as ACh and glutamate from presynaptic terminals. After releasing glutamate, many functionally distinct receptors are activated such as NMDA, AMPA and kainate receptors (Coutinho and Knöpfel, 2002). All these consequences contribute for building up more of Ca^{2+} inside the cell as illustrated in figure 1.4. There are several Ca^{2+}-dependent routes that are activated during injury, including cytoskeletal disruption (Tang-Schomer et al., 2010), cell swelling (Bullock et al., 1991), defected ATP-dependent membrane pumps (Davalos et al., 2005), mitochondrial dysfunction and apoptosis (Orrenius et al., 2003; Pivovarova and Andrews, 2010). These actions obviously confirm that the primary responses of neurons and astrocytes to mechanical forces are responsible for the following pathology. In vitro stretching studies, reveals that cells produce a quantifiable Ca^{2+} reaction only after they experience strong strains up to 40% (Rzigalinski et al., 1998). However, studies of shear pulses with cell deformation of around 4% was enough to induce a similar Ca^{2+} response (Maneshi et al., 2017). These findings describes the impact of type of force, magnitude and duration of outer loads on the severity of cellular response.

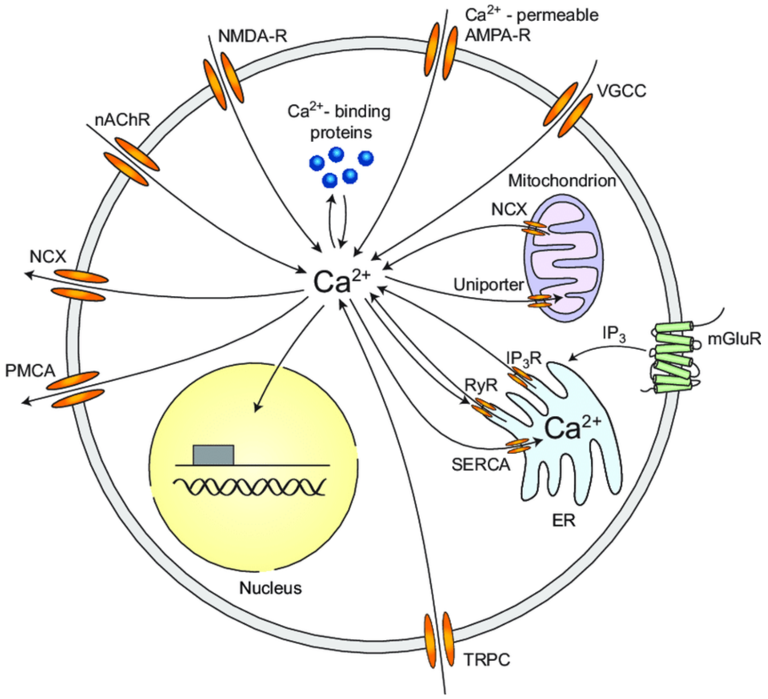

Figure 1.4 Calcium signaling in neurons
The sources of Ca^{2+} influx are N-methyl-D-aspartate (NMDA) and calcium-permeable α-amino-3-hydroxy-5-methyl-4-isoxazolepropionic acid (AMPA) receptors, transient receptor potential type C (TRPC), nicotinic acetylcholine receptors (nAChR), and voltage-gated calcium channels (VGCC) channels. Calcium release from internal stores is facilitated by ryanodine receptors (RyR) and inositol trisphosphate receptors (IP3R). Inositol trisphosphate (IP3) can be formed by metabotropic glutamate receptors (mGluR). Calcium efflux is mediated by the sodium-calcium exchanger (NCX), the plasma membrane calcium ATPase (PMCA), and the sarco-/endoplasmic reticulum calcium ATPase (SERCA). Also the mitochondria are essential for homeostasis of neuronal calcium. This figure is taken from (Grienberger and Konnerth, 2012).

1.4 Calcium action potential imaging technique

An action potential is a quick, temporary, and spreading change of the resting membrane potential. This feature is termed excitability, which is only found in neurons and muscle cells. An action potential is caused by a transitory change in membrane permeability causing diffusion of ions. This property is controlled by a threshold potential of around -50 to -55 mV. The generation of an action potential include different phases: hypopolarization, depolarization, overshoot, repolarization and hyperpolarization as described in figure 1.5.

The APs open voltage-sensitive calcium channels in excitable neurons, causing an influx of Ca^{2+} ions. The intracellular calcium concentration $[Ca^{2+}]i$ of neurons is from 50 to 100 mM during rest phase and can get 10 to 100 times higher during electrical activity (Berridge et al., 2000). Calcium is a messenger ion that has a fundamental role in most cellular functions in mammalians such as differentiation, proliferation, cell growth, signaling, gene transcription, cytoskeletal dynamics, synaptic transmission, survival, and death (Carafoli and Krebs, 2016). Thus, quantification of Ca^{2+} influx is a step to evaluate cell functionality. Over the past years, many instruments were developed to quantify calcium concentration and many calcium sensors were improved to visualize their dynamics. Calcium imaging allows the monitoring of action potential activity in a populations of neurons at the same time. Cells are loaded with fluorescent acetoxymethyl (AM) ester calcium indicators that are activated upon binding to Ca^{2+} to provide an accurate measure of APs. The key advantage of this method is enabling the identification of every active cell with a single-cell resolution.

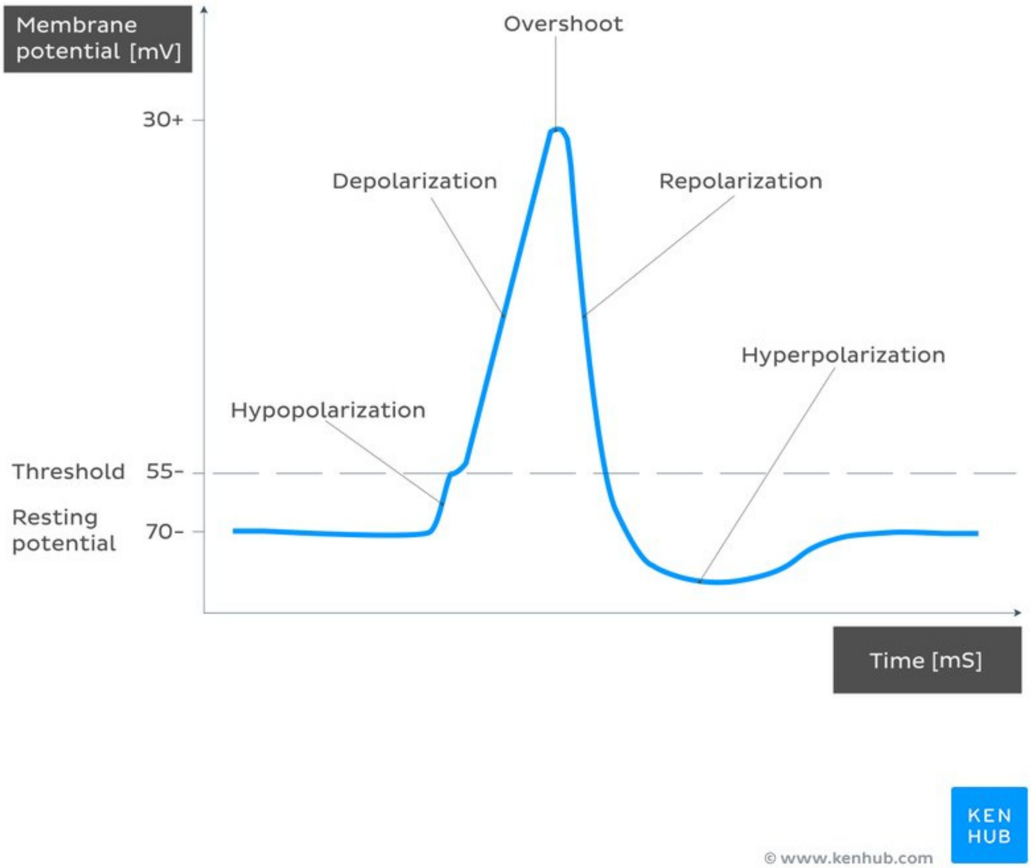

© www.kenhub.com

Figure 1.5 Representative profile of the action potential in neurons
Five phases of AP recreation are illustrated. Hypopolarization is the preliminary rise of the membrane potential to the threshold value. Then depolarization happens when threshold potential stimulates voltage-gated sodium channels to open and results in a large influx of sodium ions. In this stage, the cell becomes more electropositive until it reaches the electrochemical balance for sodium of +61 mV. This stage is termed the overshoot phase. Then, the sodium closes its channels and voltage-gated potassium channels opens, which decreases the cell's electropositivity. This part restore the resting membrane potential and it is called the repolarization phase. This leads to hyperpolarization, when the membrane potential is more negative than the standard membrane potential. (Vaskovic, n.d.)

1.5 Aim of the research

The function of neuronal cells in the brain does not comprise any obvious mechanical deformation compared with the function of osteoblasts and skeletal muscle cells. Nevertheless, neurons are exposed to physiological cyclic strain due to their location adjacent to the brain vasculature. In addition, brain cells are prone to pathological tension as a result of accidents and tumor growth, or even to direct connection cut and cell death during brain surgeries. However, the effect of cell stretch or cell death on the functionality of nervous tissues after an injury and the spontaneous reaction of connected cells are not well understood but are necessary to characterize the degree of neuronal damage.

The thesis aims to study the impact of mechanical strain and cell death on neurons by analyzing their responses based on their unique dynamic communication. Cell responses were evaluated according to changes in their calcium action potentials and formation of synapses. The techniques of cell stretching and laser ablation were chosen to strain and kill cells due to their precise stressing and disruption of cells in vitro. By combining these methods with confocal microscopy, the dynamic fluctuations in cells could be detected with a high spatiotemporal resolution. The hypothesis is that the connectivity in a neuronal network may be affected due to deformation in cell shape or complete ablation in a single cellular compartment.

Recent studies have proved that exposing neurons to a mild repetitive motion of cyclic stretch derived an adaptation process of reorientation in the cytoskeleton, increased elongation of axons and enhanced branching (Lin et al., 2020; De Vincentiis et al., 2020; Kampanis et al., 2020). Whereas, the cytoskeleton start to collapse and degrade when neurons are exposed to harsh deformation of an accident which results in loss of conscious and defects in memory and learning. Thus, it is vital to investigate how the different forms of mechanical strain is influencing the functional behavior of neurons after short and long terms.

In addition to neurons, the natural nervous tissues also consist of glial cells. Previously it had been reported that glial cells, especially astrocytes, interact and electrically couple neurons. Based on these findings, it has been proven that astrocytes have a functional significance in nervous tissues. Hence, characterization of the neuronal response to injury on cell cultures that include both neurons and astrocytes could provide valuable understanding on the communication and the nature of connection between neurons and astrocytes.

Calcium is the basis of neuronal functionality and is engaged in intracellular and intercellular signaling mechanisms. Therefore, neuronal activity and cellular connectivity can be assessed depending on the dynamic changes in intracellular calcium concentration $[Ca^{2+}]i$ in neurons before and after mechanical strain using a Ca^{2+} marker.

The main goal of this thesis is to characterize the functional behavior of neurons under strain. First, by testing physiological cyclic stretch on distinct developmental stages, as the neurons undergo several changes along the way of maturation. Then, to identify a threshold parameter that shows an immediate functional response by testing several forms and amplitudes of stretching, and also by evaluating their adaptation to long-term mechanical strains. Also, we aim to measure the secondary responses induced by mechanical loads such as immune response, and cell death. Moreover, one of the objectives of this thesis is to characterize and compare the effects of presence of astrocytes in culture on neuronal response to harsh mechanical loads. Finally, this research focuses also on analyzing the effects of single cell-compartment (neurite/soma) ablation in a well-connected neuronal network on the spontaneous activity of the surrounding cells.

The mechanical stimulus is a critical factor in the development and growth of CNS and could lead to dementia in severe cases. Here, the analysis of events following mechanical strain or single-cell death can be convenient to characterize the spontaneous behavior of connected cells, accompanying signals and the nature of intercellular connectivity between the cells.

2 Material and Methods

2.1 Material

2.1.1 Consumable materials

Consumable	**Company**
Cell culture dish 35 x 10 mm	Greiner Bio-one, Frickenhausen, Germany
Cover slip ø 12 mm #1; 25 mm #0	Menzel, Braunschweig, Germany
Immersions oil 518 F	Carl Zeiss, Jena, Germany
Microscope slides, plain	Brand, Werlheim, Germany
Parafilm	VWR, Darmstadt, Germany
PCR plates and seals	VWR, Darmstadt, Germany
Petri dishes with 18 mm hole	Cell E&G, San Diego, USA
Pipette tips (10 µL, 200 µL, 1000 µL)	StarLab, Hamburg, Germany
Reaction tube 0.2 mL, 1.5 mL, 2 mL	Eppendorf, Wesseling/Berzdorf, Germany
Centrifuge tubes 15 mL, 50 mL	Greiner Bio-one, Frickenhausen,Germany
Whatman, Lens cleaning tissue 100 x 150 cm	GE Healthcare, Freiburg, Germany
Sterile surgical scalpels	Braun, Kronberg, Germany
Dumont forceps	Fine Science Tools, Heidelberg, Germany
Glass coverslips (1.5#, high-precision, 170 ± 5 µm thickness)	Paul Marienfeld, Lauda-Königshofen, Germany
Falcon® cell scraper	Corning, Arizona, USA
Pipettes 5 ml, 10 ml, 50 ml	VWR, Radnor, PA
Latex gloves (Gentle skin)	Meditrade, Kiefersfelden, Germany
Nitrile gloves (Kimtech pure G3)	Kimberly-Clark, Irving, TX

2.1.2 Chemicals

Chemical	**Company**
Glycine	Sigma, Taufkirchen, Germany
Sylgard 184 Silicone elastomer kit (PDMS)	Dow Corning, Wiesbaden, Germany
Dry milk powder	Carl Roth, Karlsruhe, Germany
Triton-X-100	Sigma, Taufkirchen, Germany
Formaldehyde solution (37%)	Merck, Darmstadt, Germany
2-[4-(2-hydroxyethyl)-1-piperazinyl]-ethanesulfonic acid (HEPES)	Sigma, Taufkirchen, Germany
B-27 Supplement	Thermo Fisher Scientific, Massachusetts, USA
Bovine serum albumin	Merck, Darmstadt, Germany
Dulbecco's modified eagle medium (DMEM)	Thermo Fisher Scientific, Waltham, USA
Ethanol, absolute	Merck, Darmstadt, Germany
Fluoromount Aqueous	Sigma, Taufkirchen, Germany
GAPDH rattus norvegius (Rn01775763_g1)	Thermo Fisher Scientific, Waltham, USA
Gentamicin (50 mg/mL)	Sigma, Taufkirchen, Germany
GlutaMAX Supplement (100X)	Thermo Fisher Scientific, Waltham, USA
Hank's Balanced Salt Solution (HBSS)	Thermo Fisher Scientific, Waltham, USA
Hibernate-E Medium	Thermo Fisher Scientific, Waltham, USA
Isopropanol (2-propanol)	Merck, Darmstadt, Germany
IL-6 Fam rattus norvegius (Rn01410330_m1)	Thermo Fisher Scientific, Waltham, USA
LIVE/DEAD™ Fixable Red fluorescence assay	Life Technologies, Darmstadt, Germany
Methanol	VWR, Radnor, USA
Neurobasal Medium (1X)	Thermo Fisher Scientific, Waltham, USA
Phosphate-Buffered Saline (PBS) pH 7.2	Thermo Fisher Scientific, Waltham, USA
Poly-L-lysine solution Mol wt 150,000-300,000; 0.01%	Sigma, Taufkirchen, Germany
QuantiTect Reverse Transcription Kit	QIAGEN GmbH, Germany
RNeasy Plus Mini kit	QIAGEN GmbH, Germany
Trypsin-EDTA, 0.05% trypsin 0.2% EDTA	Sigma, Taufkirchen, Germany

TaqMan master mix	Thermo Fisher Scientific, Waltham, USA
Magnesium chloride (MgCl2)	Sigma, Taufkirchen, Germany
Sodium chloride	Sigma, Taufkirchen, Germany
Potassium chloride	Sigma, Taufkirchen, Germany
Calcium chloride	Sigma, Taufkirchen, Germany
Pluronic acid	Sigma, Taufkirchen, Germany
Penicillin-Streptomycin	PAN-Biotech, Aidenbach, Germany
MES (2(N-Morpholino)-ethanesulfonic acid)	Sigma, Taufkirchen, Germany
Ethylene glycol tetra-acetic acid (EGTA)	Sigma, Taufkirchen, Germany
Fetal Bovin Serum (FBS)	Thermo Fisher Scientific, Waltham, USA
L-Glutamine	PAN-Biotech, Aidenbach, Germany
ECM Gel from Engelbreth-Holm-Swarm murine sarcoma	Merck, Darmstadt, Germany

2.1.3 Media and buffers

Neurobasal media

Components	**Concentration**
Neurobasal medium	48.8 mL
B-27 Supplements	1 X
GlutaMAX Supplement (100 X)	10 X
Gentamicin	50 µg

Astrocyte culture media

Components	**Concentration**
DMEM	50 mL
L-Glutamine	1%
FBS	10%
Gentamicin	50 µg

Neurons-astrocytes co-culture media

Components	**Concentration**
Neurobasal medium	50 mL
FBS	2%
B-27 Supplements	2%
GlutaMAX Supplement (100 X)	1%
Gentamicin	50 µg

Cytoskeletal buffer (1x CB), pH 6.1

Components	**Concentration**
EGTA	5 mM
Glucose	5 mM
MES (2(N-Morpholino)-Ethansulfonacid)	1.95 g/L
$MgCl_2$	10 mM
NaCl	150 mM
Streptomycin	1.72 mM

Epatch media in milliQ water, PH = 7.2

Components	**Concentration**
NaCl	120 mM
KCl	3 mM
$MgCl_2$	1 mM
HEPES	10 mM
$CaCl_2$	2 mM

HEPES Buffer in HBSS, PH = 7.2

Components	**Concentration**
HEPES	0.02 M
Pluronic acid	0.04%

2.1.4 Dyes and antibodies

a. Primary antibodies			
Antibody	Host species	Dilution	Company
Anti-Synaptophysin 7H12 (9020)	Mouse	1:500	Cell Signaling Technology
Anti-PSD95 (3450)	Rabbit	1:500	Cell Signaling Technology
Anti-Tubulin YL ½ (MAP1864)	Rat	1:500	Millipore
Anti-Tuj-1 (MAB1195)	Mouse	1:200	R&D systems
Anti-GFAP (G9269)	Rabbit	1:500	Sigma Aldrich
Anti-LC3B (2775)	Rabbit	1:200	Cell Signaling Technology
b. Secondary antibodies			
Alexa Flour 633, anti-mouse	Goat	1:1000	Invitrogen by Thermo Fisher
Alexa Flour 488, anti-rabbit	Goat	1:1000	Invitrogen by Thermo Fisher
Phalloidin Atto 488		1:500	Sigma Aldrich
Cyanine Cy^{TM}3, anti-rat IgG	Goat	1:200	Jackson
Alexa Flour 488, anti-mouse IgG	Goat	1:1000	Thermo Fisher
Alexa Flour 568, anti- rabbit IgG	Goat	1:1000	Thermo Fisher
Alexa Fluor^{TM} 488, anti-rabbit IgG	Goat	1:500	Thermo Fisher
c. Dyes			
NucBlue (R37606)			Thermo Fisher Scientific
Cal-590 AM dextran (20510)			AAT Bioquest
4′,6-Diamidino-2-phenylindole			Invitrogen

2.1.5 Instruments

Hardware	**Company**
Centrifuge 3-16K	Sigma, Osterode,Germany
Centrifuge 5415R	Eppendorf, Wesseling/Berzdorf,Germany
CFX Connect™ Real-Time PCR Detection System	BIORAD, Düsseldorf, Germany
Clean bench HeraSafe	Heraeus, Osterode, Germany
CO_2 - Incubator Typ B12	Heraeus, Osterode, Germany
Desiccator	Duran Group GmbH, Wertheim/Main, Germany
Guava EasyCyte flow cytometer	Merck Millipore, Darmstadt, Germany
Hemocytometer	Hecht Glaswarenfabrik GmbH, Sondheim vor der Rhön, Germany
Megafuge 1.ORS	Heraeus, Osterode, Germany
Motor-driven stretch apparatus	IBI-2, research center Jülich, Jülich, Germany
Nanodrop One	Thermo Fisher Scientific, Waltham, USA
Neo 5.5 sCMos camera	Oxford Instruments (Andor)
Osmomat 030	Genotec, Gangelt, Germany
Pulsed UV laser (diode pumped solid state laser)	RAPP optoelectronics GmbH, Wedel, Germany
StepOne Real-Time PCR System	Thermo Fisher Scientific, Waltham, USA
Delta 10 TT spin coater	Suss-Micro Tec, Garching, Germany
UGA-Firefly point scanning device	RAPP optoelectronics GmbH, Wedel, Germany
Vacuum Pump RC6	Vacuumbrand, Wertheim, Germany
Vortex mixer	VWR, Radnor, USA
Water bath WNB-22	Memmert, Schwabach, Germany

2.1.6 Microscopes

Microscope	Company
Laser Scanning Microscope (LSM) 880	Carl Zeiss, Jena, Germany
Microscope Axiovert Imager-M2	Carl Zeiss, Jena, Germany
Microscope Axiovert 40 CFL	Carl Zeiss, Jena, Germany

2.1.7 Objectives

Objective	Company
20x Plan-Apochromat objective (NA 0.8)	Carl Zeiss, Jena, Germany
20x plan-Apochromat water immersion objective (NA 1.0)	Carl Zeiss, Jena, Germany
63x plan-Apochromat oil immersion objective (NA 1.4)	Carl Zeiss, Jena, Germany

2.1.8 Software

Software	Company
GraphPad Prism	GraphPad Software, San Diego, USA
Image J	Wayne Rasband, U.S. National Institutes of Health, Bethesda, USA
Matlab	MathWorks, Massachusetts, USA
StepOne Software (version2.0.2)	Thermo Fisher Scientific, Waltham, USA
Python	Python Software Foundation, Wilmington, USA
ROE-SysCon	Rapp Optoelectronics, Wedel, Germany
Solis	Oxford Instruments (Andor)
Zen black 2012	Carl Zeiss, Jena, Germany
Zen blue 2012	Carl Zeiss, Jena, Germany

2.2 Methods

2.2.1 Fabrication of culture surfaces

Deformable elastomeric chambers are suitable for cell culture studies, because they are stretchable for applying mechanical forces and transparent for cell imaging by upright and inverse microscopes. Polydimethylsiloxane (PDMS) is silica-based polymer used for biocompatible soft elastomers fabrication without harmful effects on cells. Stiffness of elastic polymer can be adjusted by the ratio used for mixing the vinyl-terminated polydimethylsiloxane and its cross-linker (methylhydrosiloxane-dimethylsiloxane copolymer). The stiffness of produced substrates from PDMS Sylgards 184 can range from 0.6 kPa to a number of GPa making it possible to mimic the physiological stiffness of 10-40 kPa surrounding cells in CNS (Qiu et al., 2010). The systems were frequently calibrated to guarantee stable material stiffness in the fabricated substrates. Since the elastomeric chambers have linear elastic response, their resistance to deformation over a range of strains is constant, and their mechanical stress is proportional to strain (Faust et al., 2011).

For the fabrication of 50 kPa PDMS Sylgard 184 for our study, a ratio of 1:40 (cross-linker: base polymer) was mixed for 10 min. To avoid the interference of air bubbles with the transparency of the substrate, the mixture was degassed via a vacuum pump for 30 min. Then the mixture was poured into home-designed molds (Figure 2.1A), which are composed of a base plate, a polystyrene mold for chamber shape, a polystyrene frame, and four acrylic glass pins for small holes formation. These molds produce substrates with an area of 4 cm^2 surrounded by walls with a thickness of 0.5 cm and a bottom thickness of 0.4 mm, giving a volume capacity of 550 µL of media (Figure 2.1B). To enable cross-linking of the elastomer, substrates were incubated for 16 hours at 60 °C.

A stiffer elastomeric system of 300 kPa from Sorta Clear was used for harsh and rotated deformations to avoid rupture and make it easier to handle. These stiffer substrates were fabricated by mixing the base and crosslinker in a 1:1 ratio and allowed to cure overnight in room temperature. These chambers were coated with a thin layer of 100 µm from 50 kPa Sylgard PDMS to guarantee comparable settings. For that reason, chambers were spin-coated with a volume of 150 µL of 50 kPa Sylgard 184 PDMS layer at 900 rpm for 8 seconds using Delta 10 TT spin coater, and followed by incubation for 16 hours at 60 °C. The thin PDMS layer was sufficient for generating a soft culture environment, while cells were unable to feel the lower hard Sorta Clear surface.

To stabilize the elastomeric chambers during cell growth period and to ensure identical cell stretching, substrates were mounted in holders after being washed with isopropanol (Figure 2.1C). Chamber holders were prestretched by 1.5 mm to avoid sacking. Drying champers at sterile conditions in 37 °C incubator for at least 4 hours until complete evaporation of isopropanol is critical for efficient surface coating and cell adherence. Chambers were sealed using a cover glass and parafilm to protect the media inside the chamber from evaporation and contamination.

For applying uniform laser to ablate cells, a flat homogenous surface is required. A culture dish of 35 mm with a pre-drilled 18 mm hole was used in the company of a glass surface of a defined thickness of 90 µm to 100 µm (#0, Ø 25 mm, Menzel). The glass surface was stuck around the hole of the dish using 1:10 mixture of PDMS, thus, generating cell culture dishes with a flat and transparent bottom for constant working distance with inverse microscopes. Before cell seeding, all fabricated elastomeric and glass surfaces were coated with 10 µg/ml of 0.01% poly-L-lysine (150,000-300,000 MW) and 100 µg/ml ECM Gel from Engelberth-Holm-Swarm murine sarcoma at room temperature overnight and washed twice with PBS.

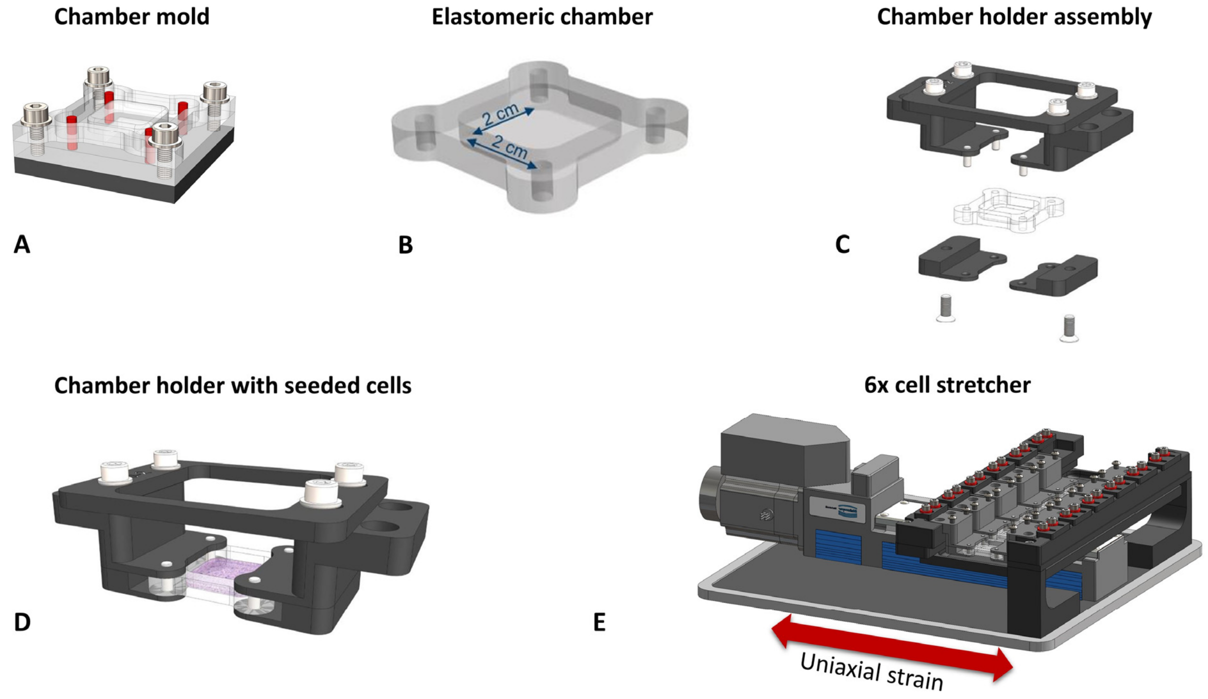

Figure 2.1 In-house fabrication and handling of PDMS elastomer chambers
Special fabrication molds were used to cure PDMS (A). An elastomeric chamber has a cultivation bottom area of 2 x 2 cm (B). The assembly of chamber holder (C) used to stabilize the elastomeric chamber during cell cultivation (D). In-house customized 6x cell stretcher is able to stretch the elastomeric chamber uniaxially (E). Pictures were created with the Inventor software by Jens Konrad, IBI-2.

2.2.2 Primary rodent cell culture

2.2.2.1 Embryo cortical neurons cell isolation and culture

Embryonic rat cortical neurons were obtained from pregnant rats (Wistar, Charles River, Sulzfeld) at day 18 of gestation (Animal testing license: 84-02.04.2015.A173, LANUV NRW, Germany). Before decapitation, rats were anesthetized with CO_2. The embryos were surgically removed from the adult rat via cervical dislocation and kept in ice-cold Hanks' Balanced Salt Solution (HBSS). Cortices were isolated from embryonic head by cutting the meninges and skeletal skull tissue with a micro scissor, then the cortex was removed using tweezers. After that the cortical tissue was separated from the striatum and hippocampal tissue and moved to 2 mL ice-cold HBSS. Subsequently, all the isolated cortices were trypsinized in 0.05% trypsin-EDTA solution (ethylenediaminetetraacetic acid) for 15 min at 37 °C. The tissue was transferred to pre-warmed neurobasal media (NB), supplemented with 1% GlutaMAX, 2% B-27, and Gentamicin. To remove remaining trypsin solution, cortices were washed three times with NB media. Subsequently, cortical cells were separated by trituration with up and down pipetting for 20-30 times and centrifuged at 900 rpm for 3 min. Counting vital bright cells was done on a hemocytometer counting-chamber using trypan blue stain for dead cells. A suitable number of cortical cells were seeded in 500µL of neurobasal media on coated surfaces. For stretching experiments on single neurons level, 85,000 cells/cm^2 were seeded on stretching chambers (Figure 2.1D) whereas 125,000 cells/cm^2 were used for neuronal network formation. For ablation experiments on neuronal networks, a concentration of 125,000 cell/cm^2 was placed on glass dishes. Other characterizing experiments used different cell concentrations that are described later. Half of the medium within the stretching chamber was changed every 2 days with fresh pre-warmed NB media. Cells were allowed to grow on the elastomeric substrates at least for 9 days before measuring calcium activity to ensure cell to cell connection and growth of axonal and dendritic branches.

2.2.2.2 Postnatal astrocytes cell isolation and culture

Rat pubs were provided by the Institute of Anatomy in Medical Faculty at the University of Cologne. Astrocytes were isolated from cortices of neonatal Wistar rats (P1 to P3) (Animal testing license: 84-02.04.2011.A169, LANUV NRW, Germany). After decapitation cortices were removed from postnatal rat head using scissor and tweezers, and afterward trypsinized for 15 min at 37 °C and 5% CO_2. Then, cells were transferred to pre-warmed media for astrocytes containing DMEM and supplemented with 10% fetal bovine serum (FBS), L-glutamine and Gentamicin. After washing the tissue twice with culture media, it was despaired by repeated pipetting up and down and then centrifuged at 1200 rpm for 2 min. Medium was exchanged on the third day after isolation. To get a pure astrocytes cell culture without microglia, on the tenth, thirteenth and sixteenth days after isolation, microglia were gently removed by shaking the cell culture flask for 1 h at 250 rpm in 37 °C. Astrocytes were trypsinized for 10 min and afterward centrifuged for 3 min at 1200 rpm, to be seeded on PDMS chambers in a suitable number. For seeding cells in a co-culture, astrocytes were either mixed directly with neurons in 1:4 ratio or rested for 3-5 days before adding primary cortical neurons for layered co-culture experiments in ratios of 1:4 or 1:1. The stretching experiments with co-culture contained different concentrations of astrocytes while the cell number of neurons was kept constant at 125,000 neurons/cm^2. Other characterizing experiments used different cell concentrations that will be described later. In co-culture chambers, media were changed to pre-warmed neurobasal media as described previously, with additional supplementation with 2% FBS.

2.2.3 Live cell calcium imaging of cortical cells in culture

To monitor the dynamic temporal and spatial changes in concentration of intracellular calcium ($[Ca^{2+}]i$) in cultured rat cortical neurons and astrocytes, cells were labeled with the red fluorescent calcium ions indicator Cal-590 acetoxymethyl ester (AM) dextran. Cal-590 is an organic cell membrane-permeable dye with a single-photon excitation peak wavelength of 570 nm and emission peak wavelength of 590 nm (Tischbirek et al., 2017). When the dye binds to Ca^{2+} ions in cells, it results in an increased fluorescence that allows detection of intracellular Ca^{2+} fluctuations. This red fluorescent Ca^{2+} indicator is suitable for imaging neuronal activity due to high signal-to-noise ratios and many other advantages as being rapid, linear response kinetics and the ability to stain any kind of neuronal tissue. Therefore, it is suitable for staining astrocytes along with neurons (Nimmerjahn *et al.* 2004; Tischbirek *et al.* 2015). However, it also has some limitations making it limited only for acute experiments due to the short recording time.

Labeling was performed by incubating cultured cells in dark at 37 °C with 0.5 µM Cal-590 AM in HEPES buffered HBSS media for 2.5 hours. Then HBSS media were exchanged to Epatch media and further incubated in dark for 10 min at 37 °C prior to imaging to let the intracellular esterases denature the AM esters to get a stable Ca^{2+}-fluorescence imaging. For signaling characterization and cell stretching experiments, live cell calcium imaging was performed with an upright microscope (Imager M2) equipped with a 20× 1.0 NA water immersion Plan-Apochromat DIC M27 75 mm objective. The microscope is equipped with an incubation system to keep the temperature at 37 °C. Images were acquired with an AndorNeo 5.5 sCMos camera with a frame rate of 66 fps for one minute. To minimize bleaching, the lowest light power was used. A 4 × 4 camera binning was used to boost recording sensitivity. Five to ten different positions were imaged for each substrate (100-300 cells/field).

Due to the requirement of laser ablation instruments, Ca^{2+} imaging for cell ablation study was performed under a confocal microscope (LSM880) with appropriate sittings. Ca^{2+} changes in cells were recorded by continuous imaging at a frame capture time of 0.63 s per frame using 20x Plan-Apochromat objective with a numerical aperture (NA) of 0.8 and a pixel size of 0.83 µm. All time-series images were analyzed using a custom-written python script.

This python program first distinguishes all cells within the image. For this purpose, the first 100 images were averaged over time to get rid of noise in the image. After that, the resulting images were smoothed by a gaussian filter (sigma=1). Then a threshold was calculated using Otsu's method. The entire image was subtracted by the threshold and each negative value was set to zero. Afterwards a binary mask was created where each value above zero was labeled as cell mask. This mask was post processed via binary opening. The image that was used for binarization was also used for the watershed algorithm to get the watershed basins (for the watershed algorithm the image was multiplied by -1). The watershed basins and the cell mask were multiplied to separate cell clusters. Cell labels with a size smaller than 20 pixels were discarded. In the next step, the average gray values for all cell labels over time were extracted from the images. Constantly, 20 time points were averaged in order to reduce noise in the data. To ensure that all the signals have a flat baseline, the slow varying signal for each cell signal was detected (Eilers, 2003; Eilers and Boelens, 2005; Boelens et al., 2005) and deducted from the original signal. Now the range of gray values (maximum – minimum) for each new cell signal was computed and cells exceeding the value of 1000 were labeled as active cells. For the next analysis, only active cells were taken into consideration. If fewer than 10 cells are active at all, the further analysis was aborted. Also if the active cells are less than 25% of all detected cells, the proceeding was not proceeded. Additionally, all peaks of every cell were detected using Pythons sycipy.signal.find_peaks function (prominence=[mean signal value], minimum height=[1000]). Moreover, the 75% width was calculated for each peak. Subsequently, the total number of peaks at each time point was calculated and all time points where the number of peaks is more than 40% of all possible peaks (number of active cells) were marked as synchronized time points. At this point, the total number of peaks at each synchronized time points is counted. The number of peaks at one and two time points before and after synchronized time point was also considered. In the same way, all cells with a peak at the time point (+-2 time points) with the most counts were considered as synchronized cells.

2.2.4 Calcium signaling characterization in cultured neurons and astrocytes

To characterize the action potentials of calcium in cultured primary rat embryo cortical neurons, a number of 85,000 neurons/cm^2 and 125,000 neurons/cm^2 were cultivated and checked for calcium intensity changes at day seven, nine and eleven. In the same way, postnatal rat pups astrocytes were seeded in different concentrations of 30,000 astrocytes/cm^2, 60,000 astrocytes/cm^2 and 125,000 astrocytes/cm^2 and tested at day fourteen. To monitor calcium spiking of neurons when co-cultured with astrocytes, a total number of 125,000 cell/cm^2 in a ratio of 1:1 were seeded for single cells level. While for network level, a total number of 250,000 cell/cm^2 were used in a ratio of 1:1 and a number of 155,000 cell/cm^2 were seeded in a ratio of 1:4 (astrocytes: neurons) and tested at day fourteen.

2.2.5 Uniaxial stretch of cultured cells

For uniaxial deformation experiments, one side of the chamber holder is moved when mounted into a custom made stretching device developed by Wolfgang Rubner as described before (Faust et al., 2011) (Figure 2.1E). Different strain parameters (amplitudes, frequencies and periods) could be set to the motor-operated stage using the in-house developed software by Werner Hürttlen. When the cultivation chambers are deformed, the attached cells on top of the elastomer matrix were also stretched by the strain and sense mechanical stress. The central regions of the substrate were examined to ensure that almost similar strains are applied. During stretching, medium was changed every 24 h. All stretch experiments were performed under sterile conditions in a humidified environment containing 5% CO_2. In addition, control experiments were done in which the cells were seeded on PDMS chambers but not stretched.

Early cyclic stretch experiments to mimic developmental deformations were performed with neurons after 24 h of cultivation to allow the cells to recover and to adhere after isolation. All other stretch experiments to mimic physiological and injury-like deformations were performed after 8-9 days of cultivation to allow the cells to grow and form a network. For the early stretch experiments a uniaxial strain amplitude of 15% and a repeat frequency of 300 mHz was applied for 24 h, 48 h or 192 h on low and high cell concentration substrates. For experiments on neuronal networks also strain amplitudes of 20% and 30% were applied. Stretching pre-aligned neuronal networks were performed by applying a uniaxial stain of 15% cyclically for 192 h until the neurites were aligned perpendicular to the strain direction (Abraham et al., 2019; Hayakawa et al., 2001). Subsequently, elastomeric chambers were rotated by 90° and stretching continued (parallel to cells) for additional 2 hours. Between each stretch and release cycle the stretcher paused for 0.417 seconds.

Static tumor-like deformation was applied with 30% or 60% amplitudes with a speed of 0.05 mm/s and the cells were kept for 24-72 h in strained position. The high speed injury-like strain experiments were performed on neurons, astrocytes and co-cultures of both cell types by applying one complete stretch and release cycle of 30% or 60% amplitudes with a speed of 80 mm/s. After stretch, the stretcher was stopped at prestretch position and the chamber holders were removed from the stretch apparatus. Calcium imaging was performed directly after straining or after a relaxing period of 24 h-72 h. Other, cells were fixed for further immunostainings or were analyzed as follows:

A) Cell viability analysis

To evaluate cell viability, flow cytometry was performed 24 hours post stretching using the LIVE/DEAD™ Fixable Red stain fluorescence assay. Principally, living cells react with the fluorescent reactive dye in the kit showing a weakly fluorescent signal while dead cells with compromised plasma membrane result in a bright signal integrating the dye within the cytosol. To quantify all dead cells, the supernatant of the chamber was collected and centrifuged before trypsinizing the cells. However, all cell viability staining was performed as stated by the suppliers' given protocol. The staining was incubated in RT for 30 mins on stretched samples, unstretched controls and 70% ethanol treated samples as positive control.

B) Immune response analysis

For measuring and analyzing the immune reactions possibly induced by mechanical deformation, RNA was isolated with the RNeasy Plus Mini kit 24 hours after stretching. RNA concentration was measured by Nanodrop UV absorption A260 nm and diluted to 0.5 – 1.0 µg with RNase free water. Synthesis of cDNA was performed by QuantiTect Reverse Transcription Kit. After cDNA synthesis, 0.5 – 1.0 µg of cDNA was diluted to a suitable concentration with RNase free water to characterize cDNA amounts of interest by using TaqMan Assay with specific primers and TaqMan master mix. For cytokine response quantification IL-6 Fam rattus norvegius (Rn01410330_m1) was used as Taq-Man assay primer and GAPDH rattus norvegius (Rn01775763_g1) was used as an endogenous control. As a positive control, some samples were treated with E. coli (lipopolysaccharide) for two hours before RNA isolation. Using a StepOne Real-Time PCR System the analysis for quantifying the amount of eGFP-mRNA transfer and measuring the immune response by expression of pro-inflammatory cytokines was accomplished. StepOne Software (version2.0.2) was used for data evaluation.

C) Autophagy marker analysis

LC3B immunocytochemistry was performed on stretched neurons and unstretched controls in the PDMS elastomer chamber. To ensure neuron's ability to express stress marker, some samples were treated with 100 µm chloroquine (CQ) for 1 hour as a positive control. After stretching cells were fixed by ice cold methanol at -20 °C for 10 min, afterwards rinsed with cytoskeleton buffer twice at RT. Cell membrane was permeabilized with 0.5% Triton-X-100 in CB for 10 min and washed with CB three times. After permeabilization cells were blocked with 5% milk powder for 1 h then removed and incubated with 0.5% primary monoclonal anti-LC3B antibody in CB with 1% milk powder overnight at 4 °C. After discarding unbound antibody cells were washed with CB three times for 5 min each and incubated for 1 h with 0.2% of the secondary antibody Alexa FluorTM 488 goat anti-rabbit IgG in CB with 1% skim milk powder. For nuclei staining 0.1% 4′,6-Diamidino-2-phenylindole was added to the mix. Next, cells were washed three times with CB for 5 min each and rinsed once with H2O (MilliQ) before adding 18 µl of Fluoromount Aqueous Mounting Medium. Immediately, a micro slide was attached on the bottom of the chamber and a glass cover slip was added on the top. After keeping the samples overnight for desiccation, chamber walls were removed by a scalpel to facilitate imaging under microscope. LC3B proteins as well as nuclei were analyzed upside down through the coverslip with confocal laser scanning microscopy with a 63x Plan Apochromat 1.4 NA oil immersion objective with appropriate settings for excitation and emission. Z-Stacks for each image to detect the whole cell body were performed. Then a maximum intensity projection was created using Zen software. Next, intensity projections of the signals were smoothed and a cell mask was designed based on the mean gray value as threshold. The manually selected threshold was kept constant for all experimental groups. The watershed algorithm was used to distinct spots in clusters. LC3B spots were counted from 2-6 cells per image and 45-49 images per group.

2.2.6 Targeted killing by laser ablation

2.2.6.1 Laser ablation technique

The technique of laser ablation could induce a high precision cut in the range of nanometers to facilitate single-cell death or even a subcellular compartment disruption. A selective manipulation is done by directing a laser beam on the cells through a microscope objective. The severity of laser ablation could be controlled by changing the used parameters such as pulse energy, duration, and frequency. Also, the selection of the beam wavelength is critical. Laser wavelengths in the range of 315-400 nm are suitable for ablation of cells, whereas lower wavelengths are absorbed by DNA and turbid media and need special optical elements. The ability to alter all of these parameters makes it a very flexible system that can be applied at different sizes and patterns at any cellular location. Thus, it was effectively used to apply mechanical injuries in many studies in order to follow cellular responses (Morsch et al., 2017; Narciso et al., 2015).

In vitro laser irradiation to selectively kill or remove a cell from a tissue or a cluster of living cells is followed by many events (as described by Kanitz et al., 2019). When short laser pulses are directed on a cell in the liquid medium by an objective lens the light is partially absorbed and reflected depending on the dielectric function of the target material. This leads to free the bound electrons which start an impact ionization cascade that accelerates the electrons by inverse-Bremsstrahlung absorption. Continued absorptions cause high kinetic energy sufficient for ionizing other molecule. Following repetitive generation of photoelectrons, a plasma plume is formed in a time scale of nanoseconds. Subsequently, the material could be ruptured and a cavitation bubble is formed when the pressure is increased. Later, the cavitation bubble could be expanded by a shockwave into surroundings.

2.2.6.2 Setup of laser ablation experiments

Targeted cutting of cultured neuronal cells was carried out using a pulsed UV laser attached to a confocal imaging setup (Figure 2.2a). The microscope was equipped with a micro-incubator system to preserve cell's viability. The ablation is performed using diode-pumped solid-state laser (DPSS) of safety class 3B with emitted radiation of wavelength (λ) 355 nm and a frequency of 1.2 kHz, a pulse duration of 1.4 ns and a peak power of 42 μJ. Coupling the UGA-firefly point scanning device to the microscope by dichroic mirrors allowed simultaneous imaging and ablation. The ROE-SysCon software is integrated to the microscope to control the ablation process. Before ablation, calibration in x, y, and z axes is done to ensure precise cutting on an empty petri dish with fluorescent marked glass coverslip (Figure 2.2b). Calibration in x and y directions was done using a manual calibration mode from the software and calibration in z-axes was performed to center the laser light on to the preferred focal plane. The desired laser power and repetitions were selected based on the experimental setup. Neuronal dense networks cultured on glass dishes were selectively irradiated by a laser intensity of 15% with total laser duration of 1-2 s to reach 1000-2000 short pulses. The high increase of Ca^{2+} -induced fluorescence intensity by Cal-590 labeling confirms the laser cut along with the rupture in cells or axons observed by continuous phase-contrast images. Instant effects of single-cell or axon ablation were recorded using imaging mode for ~ 15 min for short-term experiments. While for long-term effect experiments, continuous time-series imaging was performed for ~ 5 min after 24 hours of ablation.

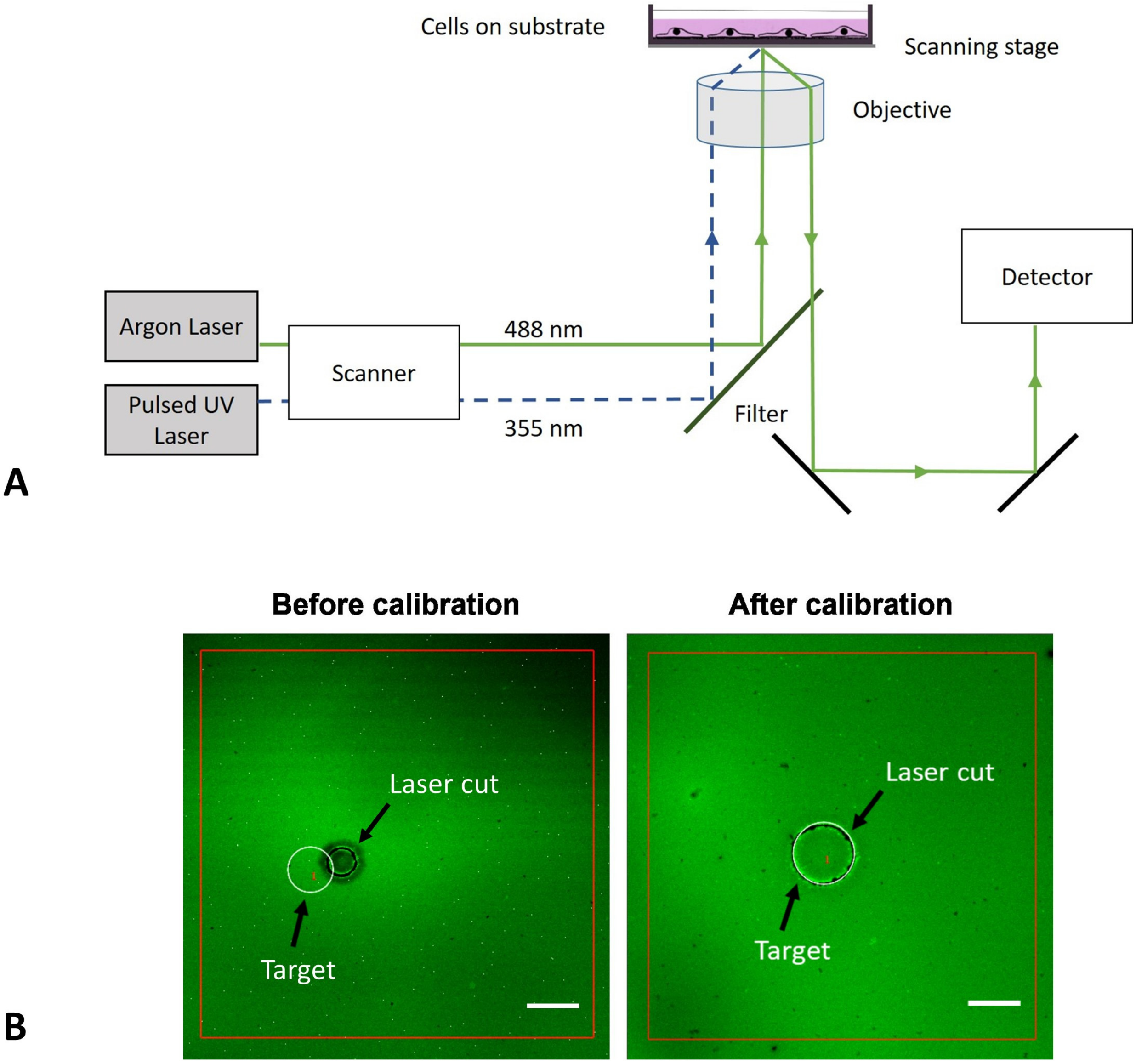

Figure 2.2 Graphic sketch of laser ablation setup:
A simple illustration of laser ablation operation, displaying the confocal setup combined with a pulsed UV laser for targeted killing of single neuronal compartment in culture (A). Two images representing the laser cut at well-defined circular target marked with a green fluorescent on a glass substrate, before calibration of the UV laser beam (left) and after (right), prior to performing laser ablation experiments (B). Scale bars: 50 µm. Images were taken from (Sridhar, 2021) PhD thesis.

2.2.6.3 Analysis of intracellular Ca^{2+} changes in cells after ablation

Ablation of cells/axons caused particular Ca^{2+} signals changes in their region. To determine these changes, algorithms were applied using Matlab (R2017; written by Georg Dreissen (Institute of Biological Information processing, IBI-2: Mechanobiology, Forschungszentrum Jülich)), to quantify fluorescence intensity of the Ca^{2+} indicator Cal-590 AM in each position. To start the analysis, the spot and the time-point of ablation were labeled manually. Ablation of the targeted spot was confirmed from the immediate rise of Ca^{2+} indicator intensity after laser irradiation. Next, concentric rings of 20 µm uniform width were created starting from the ablation point, as illustrated in figure 2.3A. The average intensity of each ring was measured at all time-points (Figure 2.3B). Depending on these quantified curves, the increase in Ca^{2+} intensities with its propagation speed induced by ablation and how long it took until Ca^{2+} intensities and beating synchrony recovered were calculated.

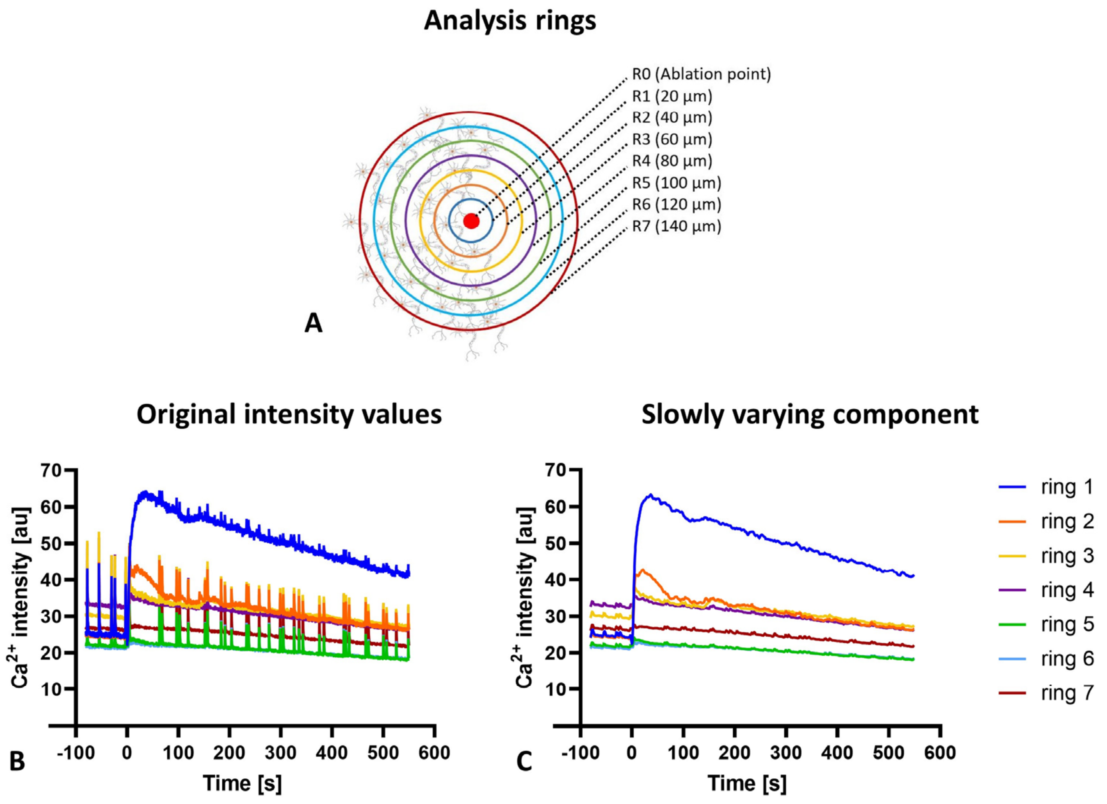

Figure 2.3 Analysis of Ca^{2+}-intensity changes over time
A Sketch of analysis rings (R1 – R7) drawn around the point of ablation as the center (R0) to monitor the fluorescence intensity changes in Ca^{2+} in neurons before and after ablation. The order of rings begins from

the central ring which contain the ablated cell (R1) and then increase until the last selected ring (R7) (A). The original plot of Ca^{2+}-intensity changes with time during and after ablation in each of the analysis rings (B). An equivalent slowly-varying signal of calcium intensity plotted against time shows the local minimal value for every peak in the original intensity plot (C).

a) Calculating Ca^{2+} propagation speed along cultured cells after ablation

In order to determine the radial propagation speed of Ca^{2+} increase, the time point of maximum reached intensity was measured for each analyzed ring. Then, the speed was measured as a ratio of the distance between the ablation point and the ring to the time consumed from ablation until the maximum fluorescence intensity reached in the ring ($\Delta x / \Delta t$). Due to the rapid waves of neurons, an additional algorithm proposed by Eilers and Boelens (Eilers and Boelens, 2005) was used to extract the slower signal of the calcium wave (Fig 2.3C). This supplementary algorithm contains a Whittacker smoother of second-order (Eilers, 2003) with asymmetric least square fitting (Boelens, Eilers, and Hankemeier, 2005). This algorithm efficiently suppressed the short calcium spikes while the slowly changing signal was well represented. Rings were selected for this analysis only if a threshold value of at least one-fold $[Ca^{2+}]i$-increase was satisfied.

b) Calculating fold-change in Ca^{2+} intensity after ablation

The change in Ca^{2+} intensity of cultured neurons after cell/axon ablation was calculated first by measuring slowly varying Ca^{2+} signal intensities from each surrounding ring before ablation then once again at the maximum reached intensities after ablation. Then, the number of fold-change in each ring is determined by calculating the ratio of maximum Ca^{2+} intensity after ablation to the original intensity before ablation.

c) Calculating $[Ca^{2+}]$ recovery times in cultured cells after ablation

As mentioned before, the intensity of Ca^{2+} signal is rapidly increased upon ablation. After some time, the intensity is recovered to levels comparable to initial values. To measure the time consumed by rings to recover to their initial intensities, an in-house written Python program was used. The script calculates the signal intensity average for each ring before ablation as reference values. Afterwards, an average of the signal after ablation was calculated by a sliding window with a block of 20 time points. The recovery time point was defined as the earliest time point when a block of the sliding window was lower than initial value.

d) Calculating neuronal network activity and synchrony after ablation

The detection of intracellular Ca^{2+} fluctuations was analyzed in two ways. The first way is by observing the overall network function changes as described in details in section 2.2.3. The other way is using the centralized rings analysis and calculating the average gray value of each ring over time then again corrected by Eilers and Boelens (Eilers, 2003; Eilers and Boelens, 2005; Boelens et al., 2005). The signals of all rings were then cross correlated and the maximum of each cross correlation was plotted.

2.2.7 Immunocytochemistry

Prior to immunocytochemistry staining, in-culture cortical cells were fixed using a solution of 3.7% formaldehyde in cytoskeletal buffer (CB) at 37 °C for 15 min. Subsequently, cells were washed twice with 10 mM Glycine-CB and stored at 4 °C until immunostaining was performed (Hersch et al., 2016). The first step of staining is cell membrane permeabilization using 0.1% Triton-X in CB for 10 min then washed with CB buffer three times. To avoid unspecific binding, cells were treated with 5% dry milk powder in CB for 60 mins. After that, cells were incubated overnight at 4 °C in 1% milk powder with a suitable dilution of primary antibody as described in table number 2.1.4.a. On the following day, cells were washed with 1% milk powder in CB. Next, cells were incubated with secondary antibody (for dilutions see table 2.1.4.b) for 1 hour in RT. For nuclear staining, chambers were incubated with two drops of NucBlue per milliliter of CB for 10 mins after secondary antibody incubation. To reduce the unspecific binding antibodies cells were washed three times with CB and followed by one time washing with Milli-Q to reduce salt crystals formation. After washing, the chambers were fixed on a glass slide and 18 µL of fluoromount was added on it, then a 15 mm glass cover slip were placed on top. Champers were kept to dry at RT for at least 24 hours, then the silicon edges were removed using a scalpel (culture dishes were treated the same). Cells were observed with an inverted laser scanning confocal microscope LSM 880.

2.2.7.1 Confocal laser scanning microscopy

The observation of fixed samples were performed upturned through the coverslip with an inverse confocal microscope equipped with a 63x/1.4 M27 OIL DIC Plan-Apochromat objective and a Plan-Apochromat 20x/0.8 M27 objective for overview images. The fluorophores of secondary antibodies with an excitation wavelength of 561 or 633 were excited with a helium/neon laser at 561or 633 nm, respectively. Secondary antibodies with an excitation wavelength of 488 were excited with an argon laser. The mean beam filter 488/543/633 was used to spot two fluorophores in one scan. The laser and gain settings were kept constant to compare intensities between samples of each specific experiment. Furthermore, a pinhole of 1 airy unit was used for all experiments. Five to ten different positions were imaged for each sample.

2.2.8 Microscopy data analysis

2.2.8.1 Cell culture purity analysis

To determine monocultures purity, a low cell density of 20,000 cells/cm^2 were used to facilitate cell distinguishing. To differentiate between cell types, neurons were labeled with Tuj-1 marker and astrocytes were labeled with GFAP marker. The fraction of cell impurity was calculated by counting the number of stained astrocytes in neurons culture or number of stained neurons in astrocytes culture and then divided by the total cell nuclei number stained with NucBlue.

2.2.8.2 Co-culture construction analysis

To investigate the structural composition of the cellular meshworks for both types of co-cultures, Tuj-1 and GFAP markers were used. For co-culture samples, Z-stack images of 1 μm each were taken for around 15 layers. All images were evaluated by a homemade python script. The program calculate the average gray value of each channel in each slice to analyze the z-shift of the maximum intensity between the two channels in co-culture samples. In the same way, z-stack images were taken for around 50 layers to calculate the z-shift between the maximum intensity of monoculture samples and the surface reflection.

2.2.8.3 Synapsis formation Analysis

Active synapses were marked by both Synaptophysin (SYP), the main synaptic vesicle protein p38 and commonly used as presynaptic terminals indicator, and postsynaptic density 95 (PSD-95), is an abundant multi-domain postsynaptic scaffolding protein that forms at the end of the spine head and organizes synaptic functions and strength. All microscopic images were analyzed by a homemade python script. First, the immunofluorescence signals in each image channel were detected. For that the images were normalized by calculation of the z-score (that is (value-mean)/(standard deviation)). For the binary mask (only the immunofluorescence signal) a threshold was calculated by adding the mean and one standard deviation. To cut out noise and artifacts, small objects with a size threshold of 10 pixels or less were discarded from the mask. Small holes with a size of 100 pixels or less were filled. To distinct signal areas, the watershed segmentation algorithm by topographic distance were used. Large objects with a size more than 300 pixels were deleted to exclude artifacts. The sum over all binary values in each image equals the whole amount of the immunofluorescence signal in every channel. The union and the intersection of both channels were determined by the same logical operations between the images. The colocalization ratio were calculated by the proportion of intersection and union.

2.2.8.4 Cell cytoskeleton and synapsis rings analysis after ablation

To observe ablation effect on cytoskeletal (Actin and Tubulin) and functional (Synaptophysin and PSD95) markers, the rings analysis system was used (described in 2.2.6.3). Then, the average gray values of each channel in each ring was calculated. For active synapsis, the average gray value of the colocalized (Synaptophysin and PSD95) parts of the two channels in each ring was calculated.

2.2.9 Statistical analysis

For all experiments, at least four separate culture substrates were used for each studied group. Independent cell isolations were analyzed to avoid cell isolation bias. The measured responses were ensured to be the result of mechanical strain as at no time cells detached from the membrane during the experiments. The measurements of Ca^{2+} activity detected after 24 hours were not done on premeasured chambers, due to cytotoxicity of Cal-590 stain that affects cell viability with time.

To compare datasets and evaluate the significance in difference between datasets, one-way analysis of variance ANOVA and Tukey’s test were performed using Graphpad Prism version 8.4.3 for Windows. All graphed data is reported as mean ± standard deviation. For all the analyses, statistical significance was set to <5% level ($p < 0.05$), where the highest p value was indicated with * for p-values ≤ 0.05, ** for ≤ 0.01, *** for ≤ 0.001, and **** for ≤ 0.0001.

3 **Results**

The spongy mass of nerve cells in the brain is exposed to a variety of internal and external mechanical stretches and stress. Some of these mechanical strains are physiological normal stretches that usually happen during embryogenesis, development and body movement. Other possible strains could have higher traumatic amplitudes, such as brain injuries from accidents. The mode of strain could be repeated cyclically as stretch induced within every heartbeat, or in a static slow rate as cases of growing brain tumors, or even as an injury that cause cell death during brain surgeries. Spontaneous signaling events following strain and the response of connected cells to these signals are studied in this thesis. The chosen cyclic strain was between 15 to 30% with a constant deformation rate of 300 mHz, while the amplitudes of 30 and 60% were used to study one static or rapid force effect. Targeted killing of neurons was performed using a pulsed UV laser beam to follow network behavior after a disconnection.

The part of results in this thesis consists of three subchapters:

3.1 The first results chapter focuses on the effect of various modes of mechanical stretching on the activity of primary neurons in monocultures. Here, the influence of strain is studied on both single cells and connected networks levels and in early and late maturation stages as well.

3.2 The second chapter highlights the influence of the astrocytes presence in co-cultures with neurons on spontaneous functionality in relaxed situations and under mechanical strains. Here the short and long-term impact of extreme mechanical injury on astrocytes and co-cultures of primary neuronal cells and astrocytes is described.

3.3 The third part characterize spontaneous signaling events in networks of cultured rat neurons upon neurite cut or single-cell death triggered by laser ablation. The impact of network disconnection on structural and functional levels is analyzed for short and long terms as well.

3.1 Effect of mechanical stretch on neurons

3.1.1 Spontaneous calcium activity is growth and cell-density dependent

To analyze the functional behavior of neuronal networks under strain, the optimal parameters for active network formation were identified. For this purpose two concentrations of primary neurons were loaded with calcium indicator then imaged and analyzed after the first week in vitro. Calcium activity is defined here as the percentage of firing cells while network connectivity is the percentage of synchronously firing cells. From analyzing the microscopic time-series images, it was found that neuronal activity had a random pattern and with a range of 10 to 25% when a low concentration of 85,000 cell/cm^2 is seeded for 7 and up to 11days *in vitro* (DIV). While, more dense cultures of 125,000 cell/cm^2 had an activity of around 40% and connectivity with synchronously firing pattern of less than 20% of the cells at 7 DIV. The activity measurements duplicated to 80% at 9 DIV and started to have a connectivity of more than 75% (Figure 3.1A, B). Furthermore, the shape of calcium signal of connected neurons had fast rise and decay times (Figure 3.1C) in the range of 1-3 seconds. From these results, day 9 was chosen to determine if neuronal function change with strain in the following experiments.

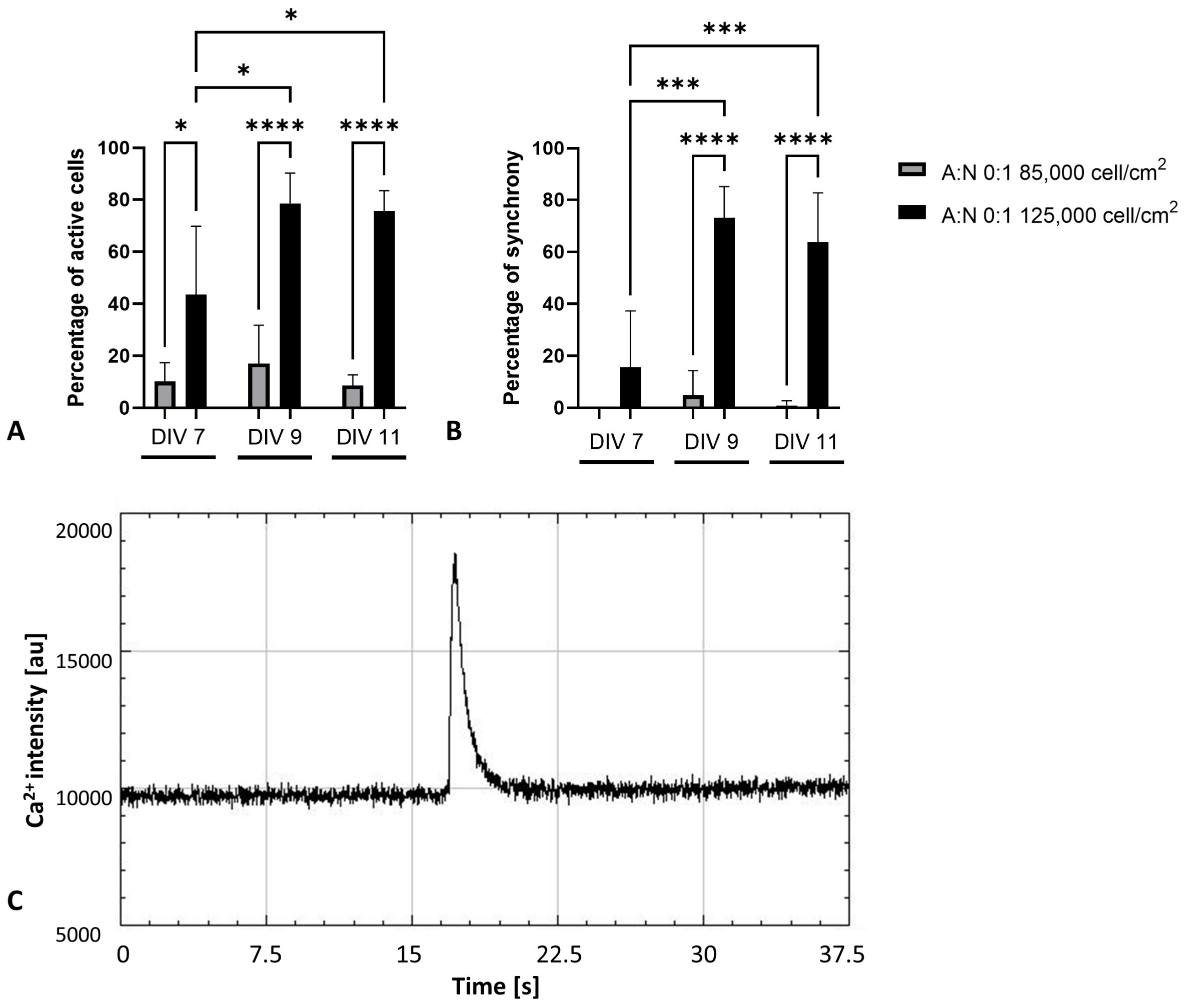

Figure 3.1 Characterization of Ca^{2+} activity of neurons in culture
A plot showing the percentage of active neurons (low concentration of 85,000 cell/cm^2 and high concentration of 125,000 cell/cm^2) after seven, nine and eleven days in vitro, N = 4 (The values represent the average, and the error bars the standard deviation) (A). The neurons spontaneous activity is vastly increased with high cell concentrations and with increased days in culture. The percentage of synchrony in different concentrations of cultured neurons is plotted over time, N = 4 (B). Plot of fluorescence intensity-changes in a neuron with time in a culture of high cell concentration is showing a behavior of fast rise and decay of calcium (C).

3.1.2 Early-stage stretching affect neuronal growth but not the functionality

To investigate if stretch-induced growth has a positive influence on cortical neuronal functionality when applied during first stages of growth, cultured cortical neurons were stretched cyclically after the first day of seeding with a mild amplitude of 15% for 24, 48 and 192 hours. An example representing early-stage stretched low-concentration neurons for 192 h and their activity is illustrated in figure 3.2A, B and C. Calcium action potentials at day 9 revealed that unstretched control samples with the low cell concentration had around 26.3% active cells (Figure 3.2D, E). Most of them were in a random pattern with a frequency mean of 3.1 peaks/minute and each event lasted for around 3.8 seconds. Similarly, early stretched neurons had a random pattern activity in 29.4%, 25.9% and 24.8% of the cells when stretched for 24, 48, and 192 hours, respectively (Figure 3.2D, E). The rate of firing in all the differently stretched neurons was about 3.4 peaks/minute and each signal lasted for around 3.7 seconds (Figure 3.2F).

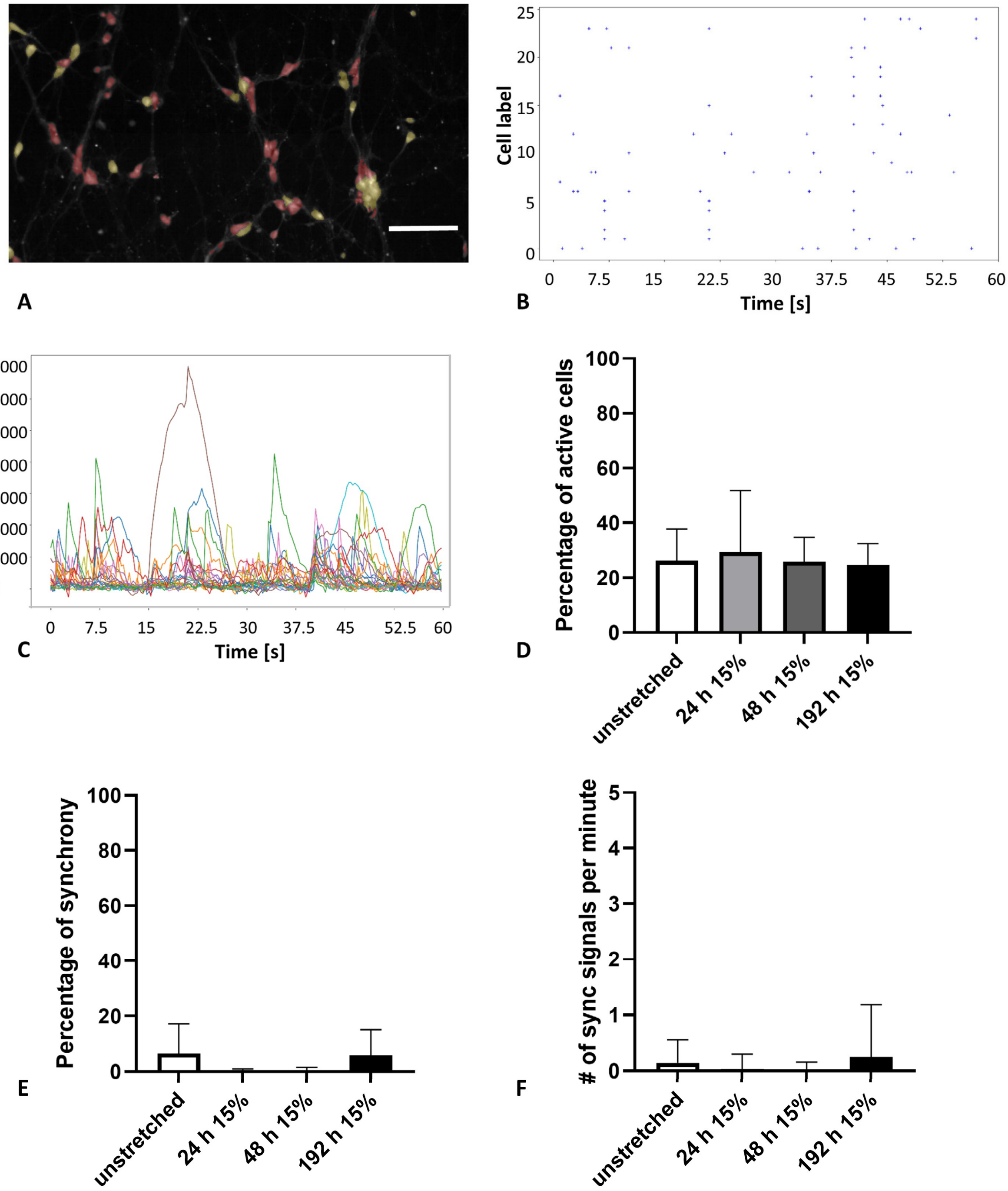

Figure 3.2 The effect of early-stage stretching on single-neurons level
A microscopic image showing culture of neurons (85,000 cell/cm^2) at DIV 9 after 192 h of cyclic 15% stretching with a frequency of 300 mHz, scale bar = 100 µm (A). The colors in the image are presenting the activity state of the cells, where active cells are represented in yellow and inactive cells are marked in red. Every signal of each active cell (25 active cells out of 76 cells) is plotted (represented by a cross) over time (sec) (B). The gray value changes in Ca^{2+} intensity (signal peaks) of all active cells is plotted over time, each cell is represented with a different color, showing a random spiking behavior (C). The graph is

comparing the percentage of active cells in early-stretched single-neuron level after 24, 48, 192 h of 15% stretching amplitude (D). The percentage of cells having synchronized peaks is plotted for unstretched, 24 h, 48 h and 192 h stretched single neurons (E). A graph of the average spiking frequencies is plotted for unstreched, 24 h, 48 h and 192 h stretched single neurons (F). The values of the graphs represent the average, and the error bars are the standard deviation, N = 5.

To examine how early cyclic stretching affects neurons activity in a network, elastomeric chambers with high cell concentration were cyclically stretched with the same magnitude. An example showing early-stage stretched high-concentration of neurons for 192 h and their activity is illustrated in figure 3.3A, B and C. Calcium fluctuations of 9 DIV neuronal networks had almost 90% active cells from total cells in culture (Figure 3.3D). Close to 85% of the cells were synchronously firing (Figure 3.3E) with a frequency of 5.5 peaks/minute where each event lasted for about 2.3 seconds. However, there was no notable difference in activity or connectivity when networks were stretched cyclically during growth with physiological amplitude neither when applied for 24 h, 48 h nor when stretched for the whole period of growth. Noting that firing frequencies for all samples were scattered between 3 to 10 peaks/minute, the synchronous firing frequency increased to 7.7 peaks/minute in samples stretched for 48 hours. Oddly, it was decreased to 2.9 peaks/minute when samples were stretched for 192 hours (Figure 3.3F).

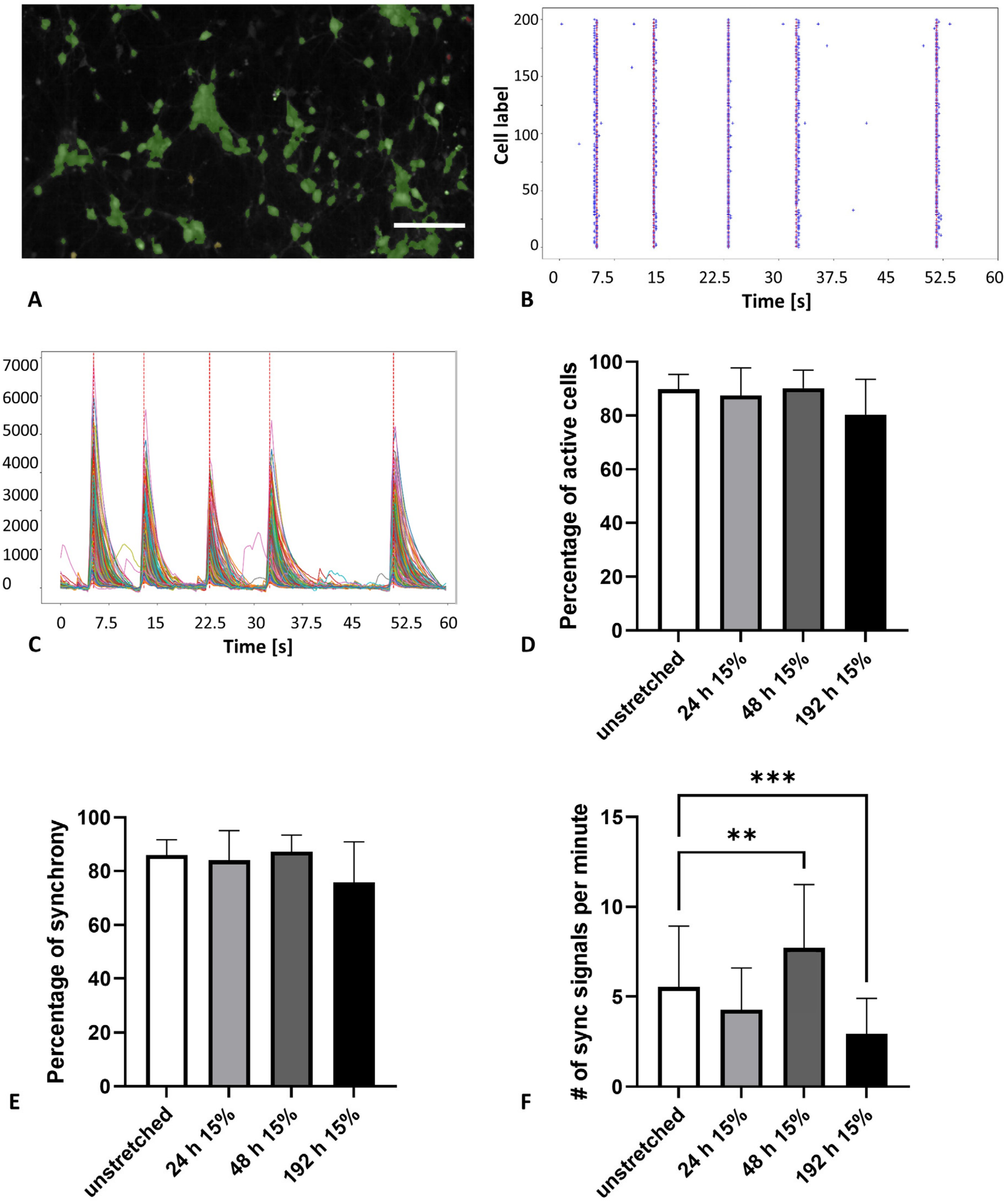

Figure 3.3 The effect of early-stage stretching on neuronal network level
A microscopic image for a culture of neurons (125,000 cell/cm^2) at DIV 9 after 192 h of cyclic 15% stretching with a frequency of 300 mHz, scale bar = 100 µm (A). The colors in the image are representing the activity state of the cells, where inactive cells are represented in red, active cells are marked in yellow and cells with synchronized activity are in green. Every signal of each active cell (201 active cells out of 203 cells) is plotted (represented by a cross) over time (sec) (B). The gray value changes in Ca^{2+} intensity

(signal peaks) of all active cells is plotted over time, each cell is represented with a different color, showing a synchronized spiking behavior (C). A graph is comparing the percentage of active cells in early-stretched neuronal network level after 24, 48, and 192 h of 15% stretching amplitude (D). The percentage of cells with synchronized peaks is plotted for unstretched, 24 h, 48 h and 192 h stretched neuronal networks (E). A graph showing the mean synchronized spiking rates in unstreched, 24 h, 48 h and 192 h stretched high concentration of neurons (F). The values of the graphs represent the average, and the error bars are the standard deviation, N = 4.

3.1.3 Cyclic stretching after network formation is functionally tolerable

To examine the effect of stretching induced by regular body movement in adult brain, amplitudes of 15, 20 and 30% were applied cyclically after neuronal network formation for 24 hours from day 8 to day 9. Fluorescent calcium imaging of 15 and 20% magnitudes revealed that most of the neurons were synchronously active when imaged directly after stretch and kept the same activity when imaged 24 hours after stretch (Figure 3.4A, B). The harsh stretching amplitude of 30% caused a reduction in synchronously firing cells from 86.5% to 60.5% directly after stretch (Figure 3.4B), moreover, firing rate decreased from 8.2 to 4.0 peaks/minute (Figure 3.4C). However, this result disappeared when calcium activity was imaged 24 hours after stretch. Notably, the firing rate of 15% stretched samples at the next day after stretch dropped to an average of 3.6 peaks/minute. It is worth mentioning here that not only cyclic stretching but also cyclic compressing was applied on some other samples with the amplitude of 15% continuously for 24 hours. Similar to cyclic stretching, mild cyclic compressing had no influence on neuronal network activity and connectivity, even when monitored after 5 days.

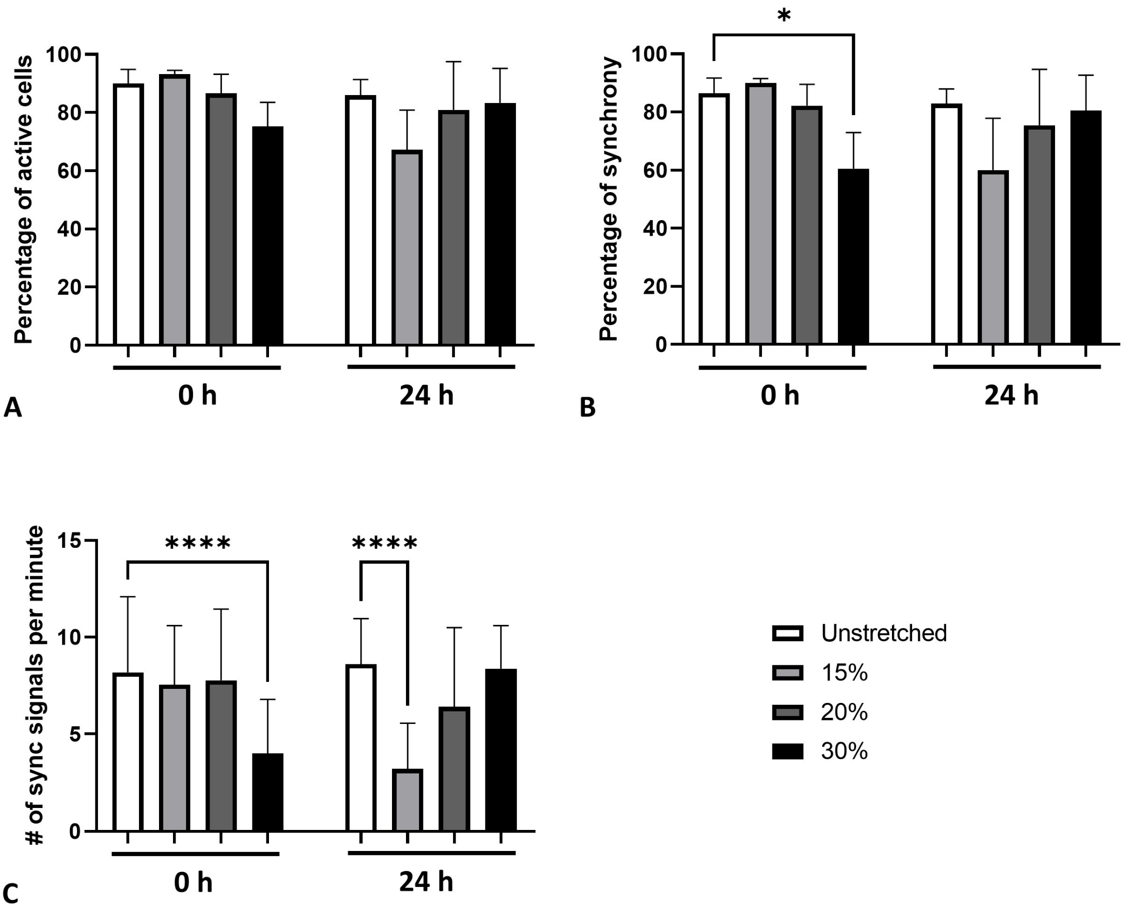

Figure 3.4 Functional behavior of cyclically stretched pre-formed neuronal networks
A graph comparing the percentage of active cells in 24-hour cyclically stretched neurons after networks formation (at day 9) with different amplitudes of 15%, 20% and 30% and a constant frequency of 300 mHz and their relative activities after 24 hours of stopping the stretching tensile (At day 10) (A). The measurement of connectivity between neurons were plotted as percentage of cells joining in the synchronized peaks in unstretched, 15%, 20%, and 30% cyclically stretched mature networks with a rate of 300 mHz and after 24 hours later (B). A graph of the average synchronized spikes frequencies in unstreched, 15%, 20% and 30% cyclically stretched neuronal networks is plotted for 24 hours and after 24 hours further (C). The values of the graphs represent the average, and the error bars are the standard deviation, N = 4.

3.1.4 Directing the stretch onto neurites is functionally resistible

As cells in the cortex are arranged in a layer of cell bodies and a layer of aligned neurites, some external forces focus on the inner layer of neurites. In the previous experiments, stretch was applied on randomly oriented neurons. To ensure that stretch is applied on neurites, neurons were aligned perpendicular to the stretch direction by prestretching (15%, 300 mHz) continuously for the whole period of growth, before rotating the chamber to be stretched in the other direction for 2 hours with the same amplitude and frequency. This method was proved to reorient the actin bundles to be almost perpendicular to the stretch direction to avoid being overstrained. Despite that strain was directly applied to neurites, the activity and connectivity were in the range of 75 to 90% and the synchronized spikes had an average rate of 5 spikes/minute (Figure 3.5A, B and C). There was no evidence of any change in network spiking activity and connectivity when cells were tested directly after stretch or when they were imaged 24 hours after stretch.

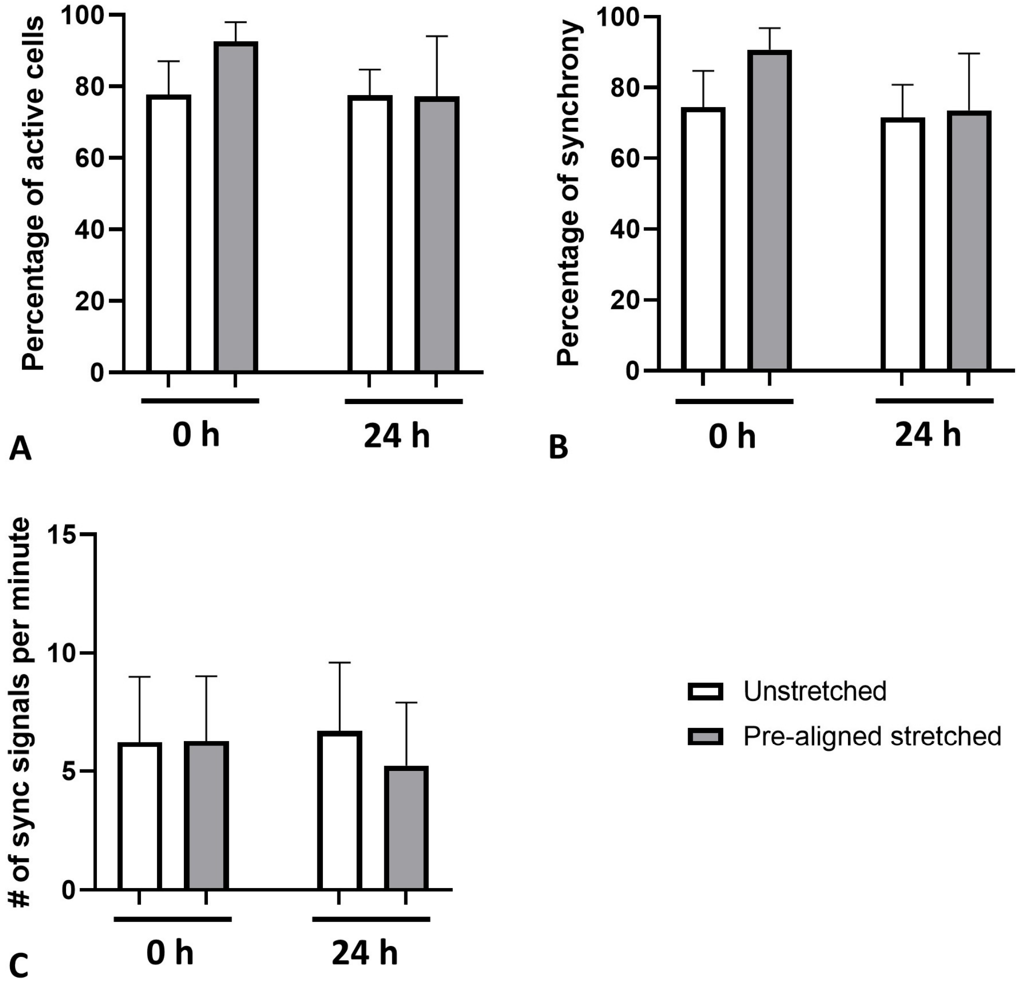

Figure 3.5 Neuronal functionality with neurite-focused stretching
Using calcium-fluctuations imaging, the percentage of active neurons (A), the percentage of synchronously active neurons (B) and the frequency of synchronized spikes (C) were plotted for unstretched and 15% stretched networks with aligned cells (in the direction of stretch) for 24 hours with a frequency of 300 mHz and their measurements after 24 hours later. The values of the graphs represent the average, and the error bars are the standard deviation, N = 4.

3.1.5 Neurons show functional resilience to constant stretch

To simulate stress created by the growth of nodular tumor mass, slow and static deformation amplitudes of 30% and 60% were applied with a low speed of 0.05 mm/s on mature neuronal networks. As shown in figure 3.6A and B, cells were still attached on champers and were stretched with the same magnitude as the elastomers. Neurons were kept in the constant stretched state for 72 hours. As a result, 60% deformed networks had a considerable loss in their functionality where active cells number reduced to the half and more than the half were unable to fire synchronously (Figure 3.6C, D), while 30% static stretch was tolerable. In addition, rate of synchronous firing was reduced in 30 and 60% statically stressed substrates to 3.8 and 1.2 peak/minute, respectively (Figure 3.6E). But these changes disappeared when calcium oscillations were recorded over a longer term of 24 and 72 hours while keeping substrates in constant stretch position.

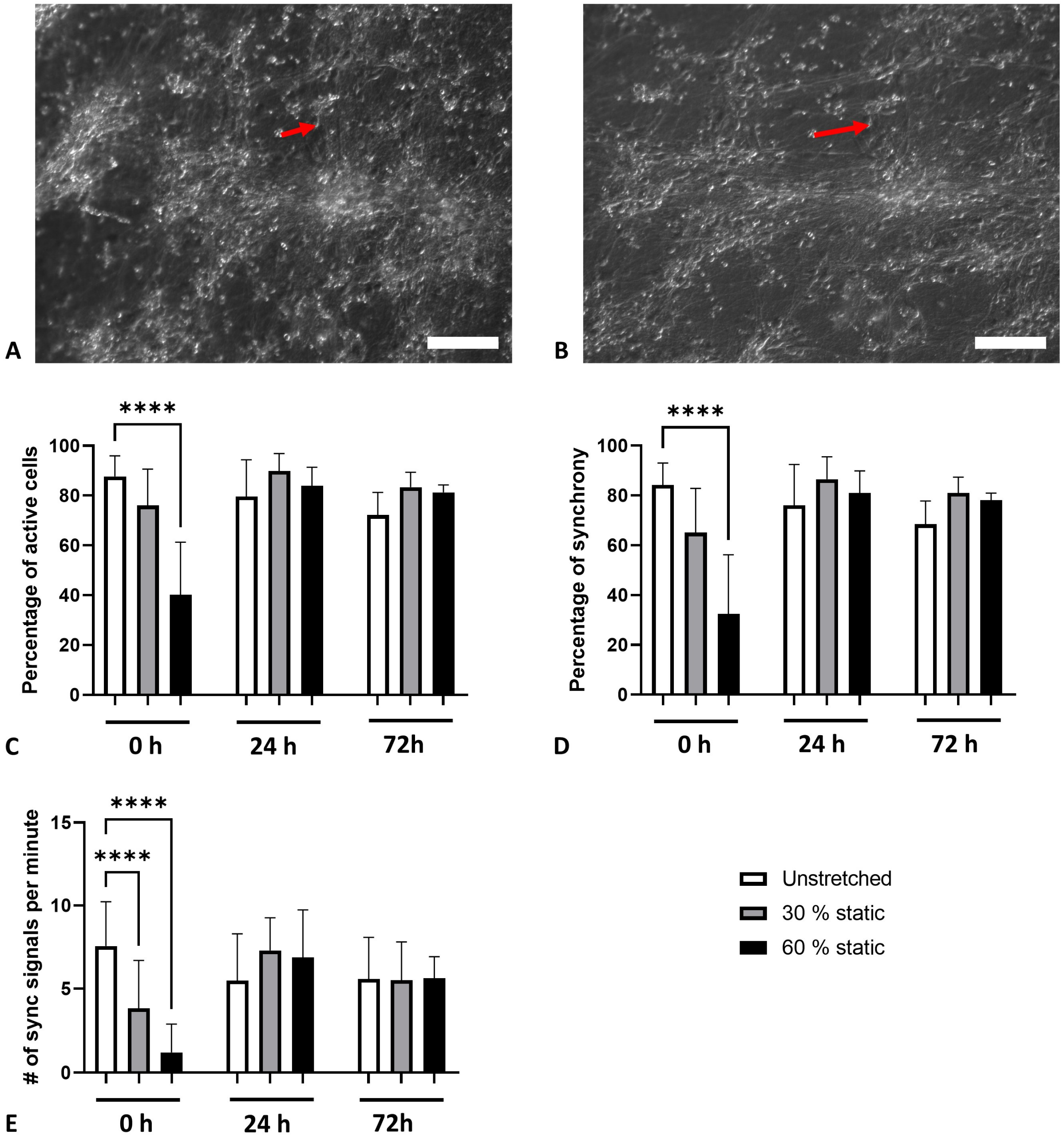

Figure 3.6 Constant-stretch state effect on neuronal networks function
A microscopic bright-field image of cultured cortical neurons at day 9 before (A) and after (B) a slow (increased by 0.05 mm/s) static stretch that kept constant at an amplitude of 60%. The red arrow shows the stretch direction and the distance difference before and after stretch, scale bar = 100 µm. Using calcium imaging, the percentage of active neurons (C), the percentage of synchronously active neurons (D) and the frequency of synchronized spikes (E) were plotted over time for unstretched, 30% and 60% slowly and statically stretched networks. The values of the graphs represent the average, and the error bars are the standard deviation, N = 4.

3.1.6 Rapid traumatic stretch-injuries are recoverable

To inspect neuronal network functional reaction during and after injury, one cycle of fast stretch was applied with harsh amplitude of 30% and very severe amplitude of 60% with a high speed of 80 mm/s. Right away after strain only extreme deformation of 60% showed failure in communication between neurons. Following severe injury, the percentage of cells having calcium signals decreased from 83.9% to 42.1% (Figure 3.7A) and the percentage of cells joining in synchronous firing changed from 81.1% to barely 31.7% (Figure 3.7B). As well, firing rate became slower by shifting from 6.6 peaks/minute in unstretched samples to 1.4 peaks/minute in 60% rapidly deformed neurons (Figure 3.7C). However, this loss in connectivity was repaired within 24 hours after stretch injury and maintained in normal communication levels even after 72 hours. It is noteworthy that rapid compressing-injury was also applied, as samples were stretched to 30% before cell seeding then a rapid one cycle of 30% compressing was performed. Compressing deformation with a high-speed showed no effect on neuronal network dynamics, even when checked after 120 hours. However, the results were not plotted in a graph due to lack of sample replicates.

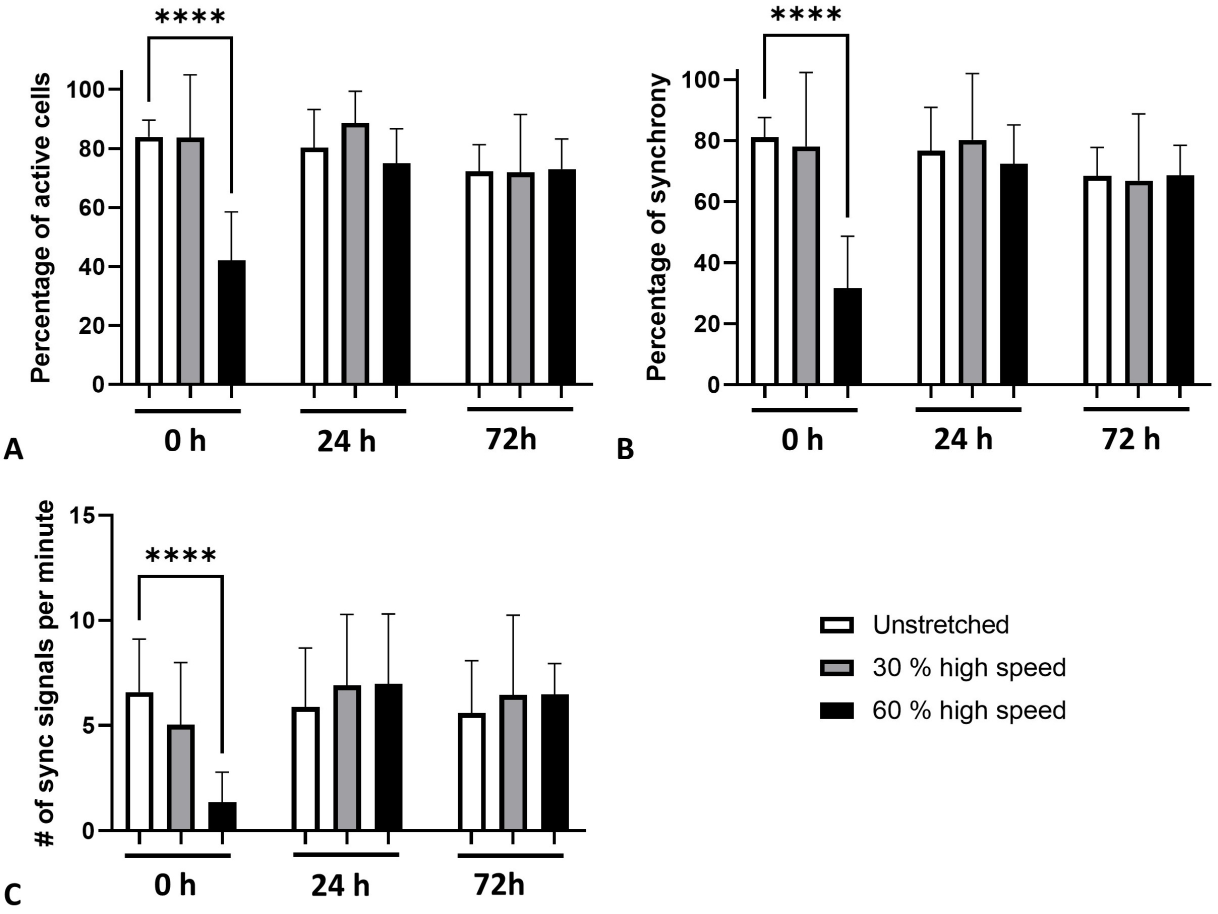

Figure 3.7 The influence of rapid stretch injury on neuronal functionality
By recording changes in calcium intensities, the percentage of active neurons (A), the percentage of synchronously active neurons (B) and the frequency of synchronized spikes (C) were plotted for unstretched, 30% and 60% stretched networks with a high speed of 80 mm/s for one cycle and their measurements after 24 and 72 hours later. The values of the graphs represent the average, and the error bars are the standard deviation, N = 4.

3.1.7 Secondary complications are limited after stretch injury

Numerous responses can occur immediately or over a period of hours or days after the initial brain injury. These secondary reactions include phases of cellular and chemical changes that could lead to further consequences starting from headache and loss of consciousness, as well as disabilities in attention, and memory that could lead to a neurodegenerative disease in the future, or even to death. Here are the results of some of the tested secondary changes:

3.1.7.1 Stretching has an insignificant influence on chemical synapses formation

To observe how mechanical tensile loading is affecting the formation of active neuronal synapses, labeling by immunostaining was used. Active synapses are marked by both Synaptophysin (SYP) and postsynaptic density 95 (PSD-95) (Figure 3.8A). The results of colocalized pixels analysis from microscopic images showed that the percentage of active synapses was almost the same when cortical single neurons and networks were stretched cyclically with physiological mild amplitude of 15% for 24 and 48 hours during the early stage of growth (Figure 3.8B, C). Likewise, the detected difference when neuronal network was exposed to 15% cyclic stretch for 24 hours after network formation and even after longer term when active synapsis were imaged 24 hours post stretch was insignificant (Figure 3.8D). Not only mild strain but also moderate and severe rapid deformations had no immediate effect on synapses activity or after 24 hours as well. The average of 6.1% of colocalized pixels in unstreched controls were nearly the same directly after the deformation of 30 and 60% and for 24 hours post deformation (Figure 3.8E).

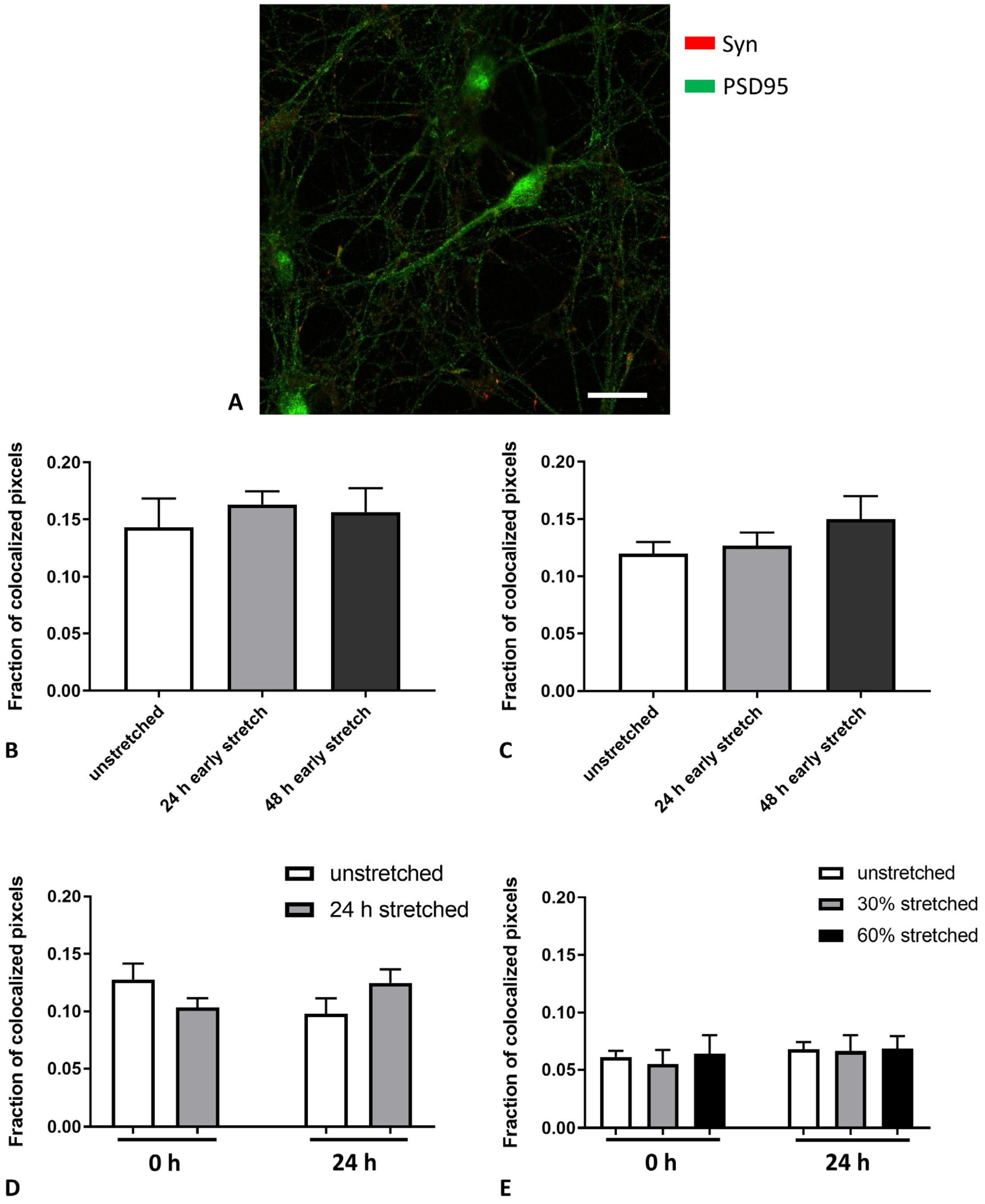

Figure 3.8 The effect of stretching on synapses formation
Stretched cortical cells were stained against Syn and PSD-95, pre-synapses are indicated in red while post-synapses are indicated in green, scale bar = 20 µm (A). From the immunofluorescence imaging and the analyses of colocalized staining of pre and post- synapses, the fraction of active synapses were quantified and plotted for early-stage stretched neurons in single-cell level (B) and network level (C) with an amplitude of 15% for 24 h and 48 h (N = 3). The fraction of active synapses was plotted for 24 hours stretched cells at day 9 after network formation at 15% and 24 hours later (N = 3) (D) and for rapidly deformed mature networks with one cycle of 30 and 60% amplitudes and 24 hours later (N = 6) (E). The values of the graphs represent the average, and the error bars are the standard deviation.

3.1.7.2 Strained neurons are unable to stimulate inflammatory reaction

To evaluate the inflammatory reaction of neurons with mechanical strain, the expression of IL-6 was measured 24 hours after stretch. The quantification of IL-6 response in cultured neuronal networks after a range of mechanical strains starting from mild cyclic deformation to harsh quick deformation revealed that there was only a slight increase of around 1 to 2 folds (Figure 3.9). However, treating the neurons with E-coli for 2 hours, as a positive control, resulted in an increase of 290-folds in IL-6 expression.

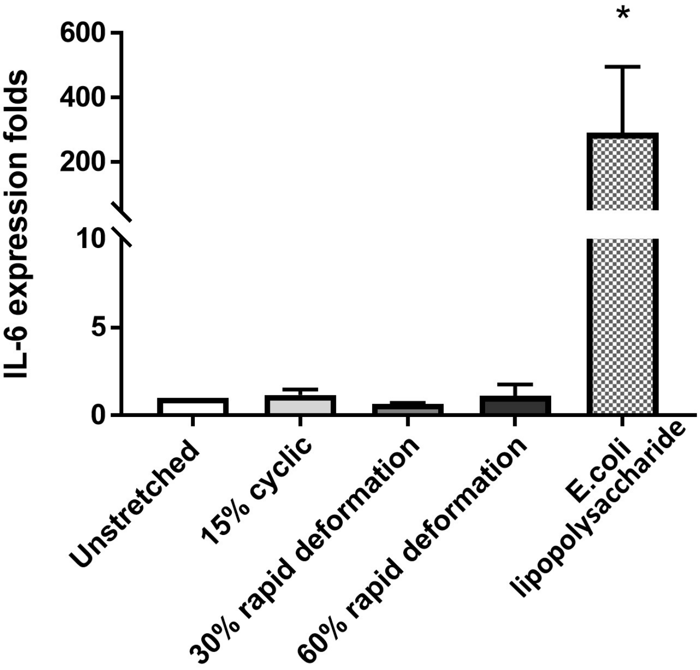

Figure 3.9 Inflammatory response of neurons to mechanical strain
By testing the mRNA levels of IL-6, the folds of IL-6 expression after 24 hours of deformation were plotted for unstretched, 15% cyclically stretched neurons for 24 hours, one cycle of 30 % and 60% rapidly stretched neurons and neurons treated with E-coli (a positive control to confirm the efficiency of the protocol). The values of the graph represent the average, and the error bars are the standard deviation, N = 3.

3.1.7.3 Autophagosome formation is stretch-mode dependent

To monitor signals of cellular stress, the accumulated spots of LC3B protein to autophagosomes were detected and analyzed. The quantity of LC3B spots were calculated after 1 hour, by comparing stretched neurons in culture with unstretched controls and with chloroquine (CQ) treated neurons (Figure 3.10A). The data indicated that 15% cyclically stretched neuronal networks had a significant rise in percentage of LC3B (Figure 3.10B). However, the number of LC3B spots in 30 and 60% fast stretching groups remained unchanged. Despite the fact that repetitive stretching had a lower deformation amplitude, it showed a remarkable increase in LC3B spots compared to unrepeated, faster and higher stretching amplitudes.

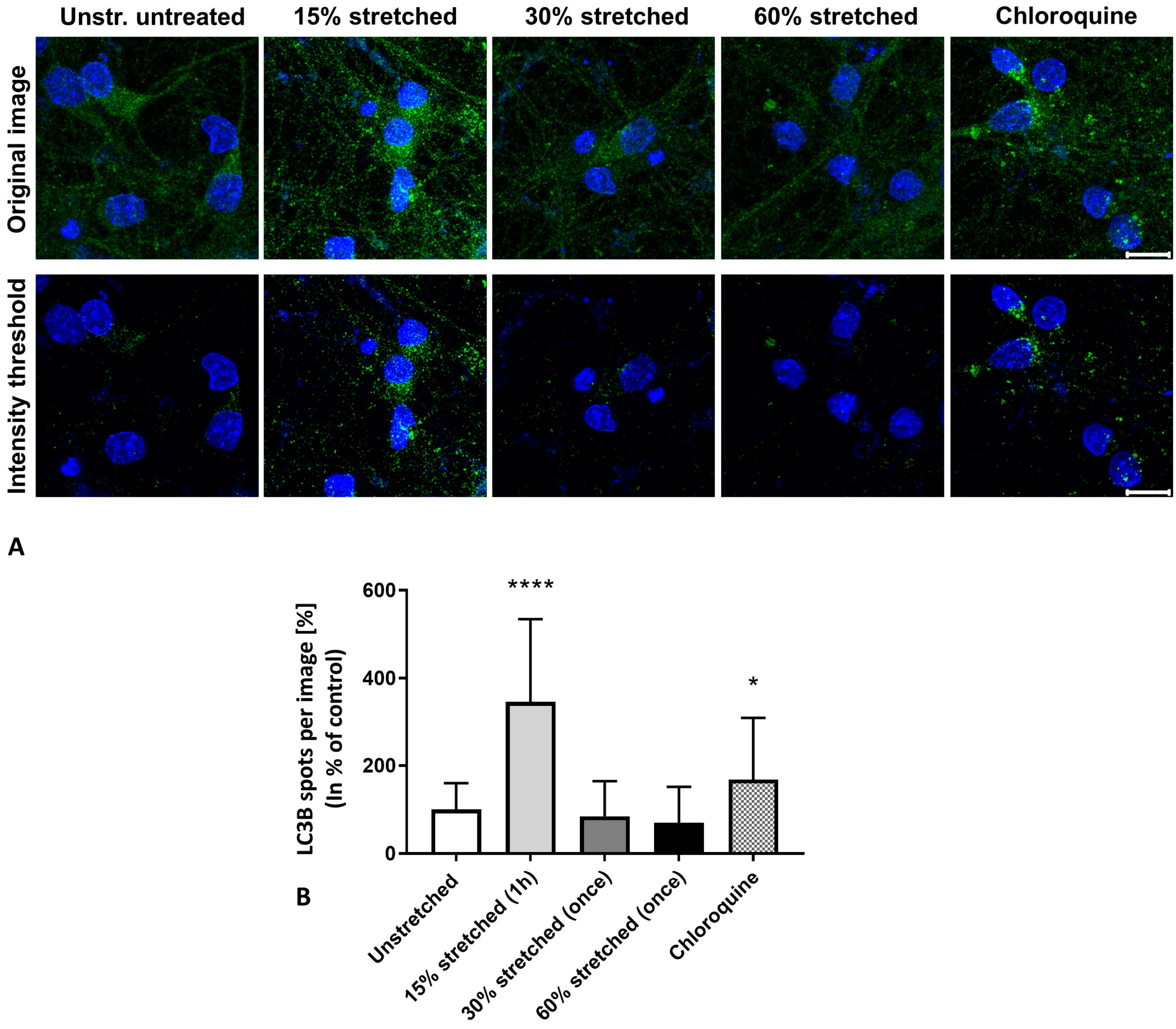

Figure 3.10 Autophagosome formation with mechanical deformation
Stretched cortical neurons were stained against autophagy protein (LC3B) which is indicated in green, and nucleus were stained with DAPI and indicated in blue. The original detected LC3B spots are illustrated in the upper images while the lower images represent the detected spots after a cell mask designed based on the mean gray value as threshold, scale bar = 10 µm (A). LC3B protein spots were quantified after 1 hour of strain and were plotted for unstretched, 15% cyclically stretched neurons for 1 hour, and one cycle of 30 % and 60% rapidly stretched neurons and neurons treated with chloroquine (B). The values of the graph represent the average, and the error bars are the standard deviation, N = 3.

3.1.7.4 Neuronal viability is unaffected after stretching

To check if any type of uniaxial deformation cause alteration in cultured neuronal viability in the period of 24 h after strain, the number of dead cells was calculated by flow cytometry. The percentage of dead cells had no significant change after 15% cyclic stretch or 30 and 60% rapid stretch. These results were evaluated by comparing them with unstretched networks which had a mean of 14.7% dead cells, and ethanol treated controls with an average of 66% dead cells (Figure 3.11).

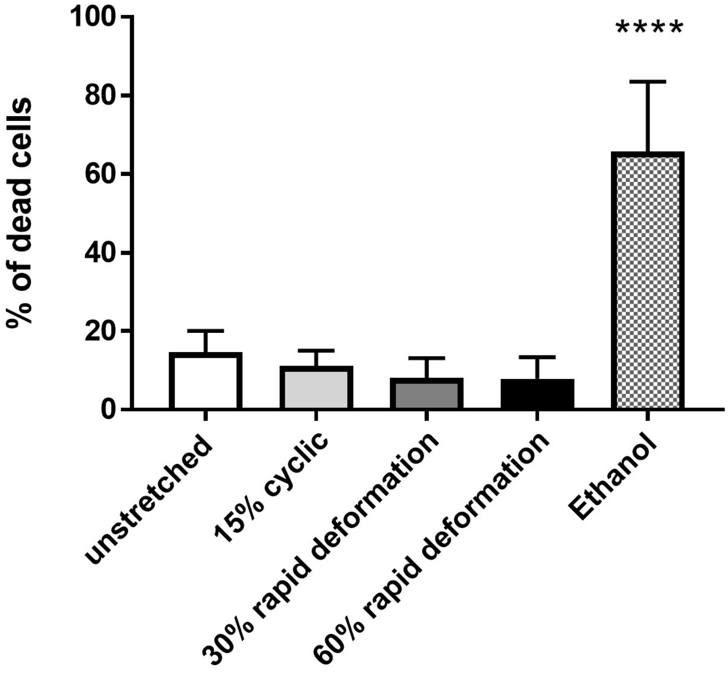

Figure 3.11 Viability of neurons with mechanical strain
Using flow cytometry analysis, the percentage of stained dead cells were plotted for unstretched, 15% cyclically stretched neurons for 24 hours, and one cycle of 30 % and 60% rapidly stretched neurons and neurons treated with ethanol (to confirm the efficiency of live/dead stain). The values of the graph represent the average, and the error bars are the standard deviation, N = 6.

3.2 The influence of astrocytes on neuronal activity

For accurate brain function other glial cells are essential such as astrocytes, the most abundant type of glial cells. Monitoring the influence of astrocytes on the behavior of neurons facilitates understanding the environment of the brain and how it is regulated in relaxed states and under stressing situations. Before performing experiments on monocultures and co-cultures of neurons or astrocytes, a cellular purity check for isolated cells is mandatory. To differentiate between the two cell types, a green fluorescently labeled antibody against Tuj-1 in neurons and a red fluorescently labeled antibody against GFAP in astrocytes were used as seen in figure 3.12A and B (refer to section 2.2.8.1). The results of counting stained cells showed that both isolated neurons and isolated astrocytes cultures had a high purity concentration above 90%. Monocultures of neurons contained some astrocytes that occupied a percentage of 5.3% of the cultured cells. Similarly, cultures of astrocytes had an impurity percentage of 7%.

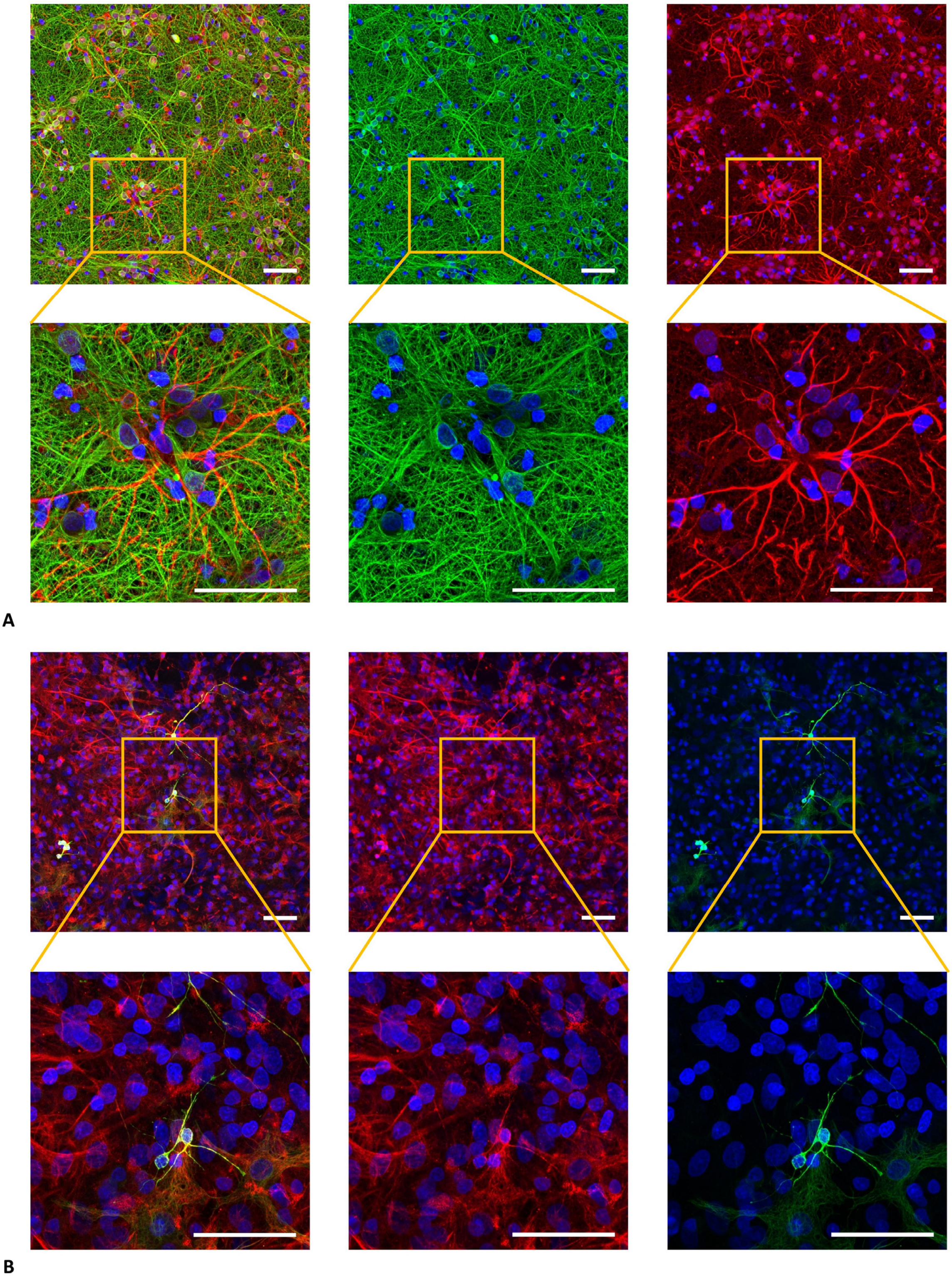

Figure 3.12 Cell culture purity of isolated neurons and isolated astrocytes
Using immunofluorescent staining, monocultures of neurons (A) and astrocytes (B) at day 8 have a high purity percentage (N = 4). The Tuj-1 in neurons is indicated in green and GFAP of astrocytes is indicated in red while the nuclei is stained in blue, scale bar = 50 µm.

3.2.1 Astrocytes are less active and have a slow waving signals in culture

To spot the *in vitro* calcium fluctuations between cells in pure astrocytes cultures, calcium intensity changes were monitored under microscope. Astrocytes had less activity *in vitro* compared with neurons. As reflected in figure 3.13A, random firing activities in the range of 5, 20 and 40% of the cells were detected after 14 DIV in the different astrocytes concentrations of 30,000, 60,000 and 125,000 cell/cm^2, respectively. The calcium signal in half of the samples had long rise and decay times and appeared like non synchronized slow waves spreading from one cell to the other (Figure 3.13B), in a relatively slow period of 5 to 7 seconds.

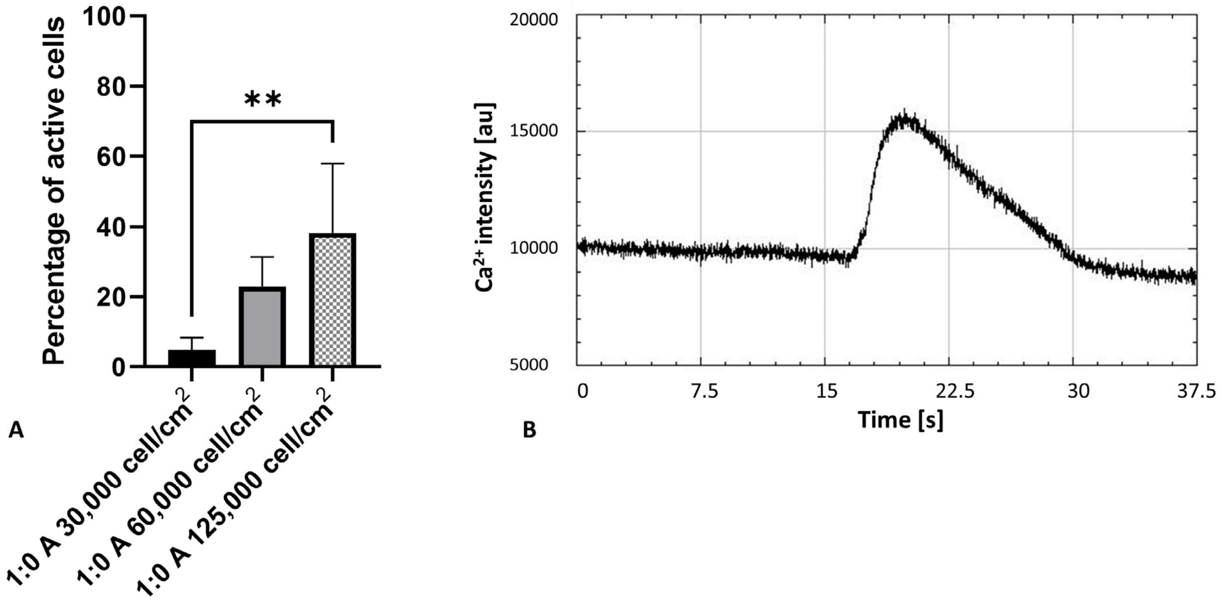

Figure 3.13 Calcium signal of astrocytes in culture
A plot showing the percentage of active astrocytes cultured with different concentrations of 30,000 cell/cm^2, 60,000 cell/cm^2 and 125,000 cell/cm^2 after 14 days in vitro. The values represent the average, and the error bars the standard deviation, N = 4 (A). Plot of fluorescence intensity-changes in an astrocyte with time in a culture of high cell concentration is showing a behavior of slow rise and decay of calcium (B).

3.2.2 Astrocytes enhance connectivity between neurons in low density cultures

To explore how calcium rise and fall is influenced by the presence of astrocytes in culture, different cellular ratios were tested. Here, the results revealed that low density neurons in monocultures had activity of approximately 12% and astrocytes in monocultures had activity of about 22%. On the contrary, when both cell types were co-cultured together with the same cell number the activity enhanced to reach more than 70% of the cells (Figure 3.14A) and cells signaling established a synchronized firing pattern in around 65% of the cells (Figure 3.14B) with a peaking rate of 4 peaks/minute (Figure 3.14C). Furthermore, when the activity of high density mono and layered co-cultures were compared, they resulted in around 95%, 40%, 65% and 68% for monoculture of neurons, monoculture of astrocytes, 1:1 and 1:4 co-cultures, respectively (Figure 3.14D). Also, the average connectivity in high density cultures had a percentage of 97% in monoculture of neurons, 60% in both layered co-culture ratios and 6% in monoculture of astrocytes (Figure 3.14E). In addition, there were no significant changes between monoculture of neurons and co-cultures neither in synchronized peaks frequency (Figure 3.14F) nor time length.

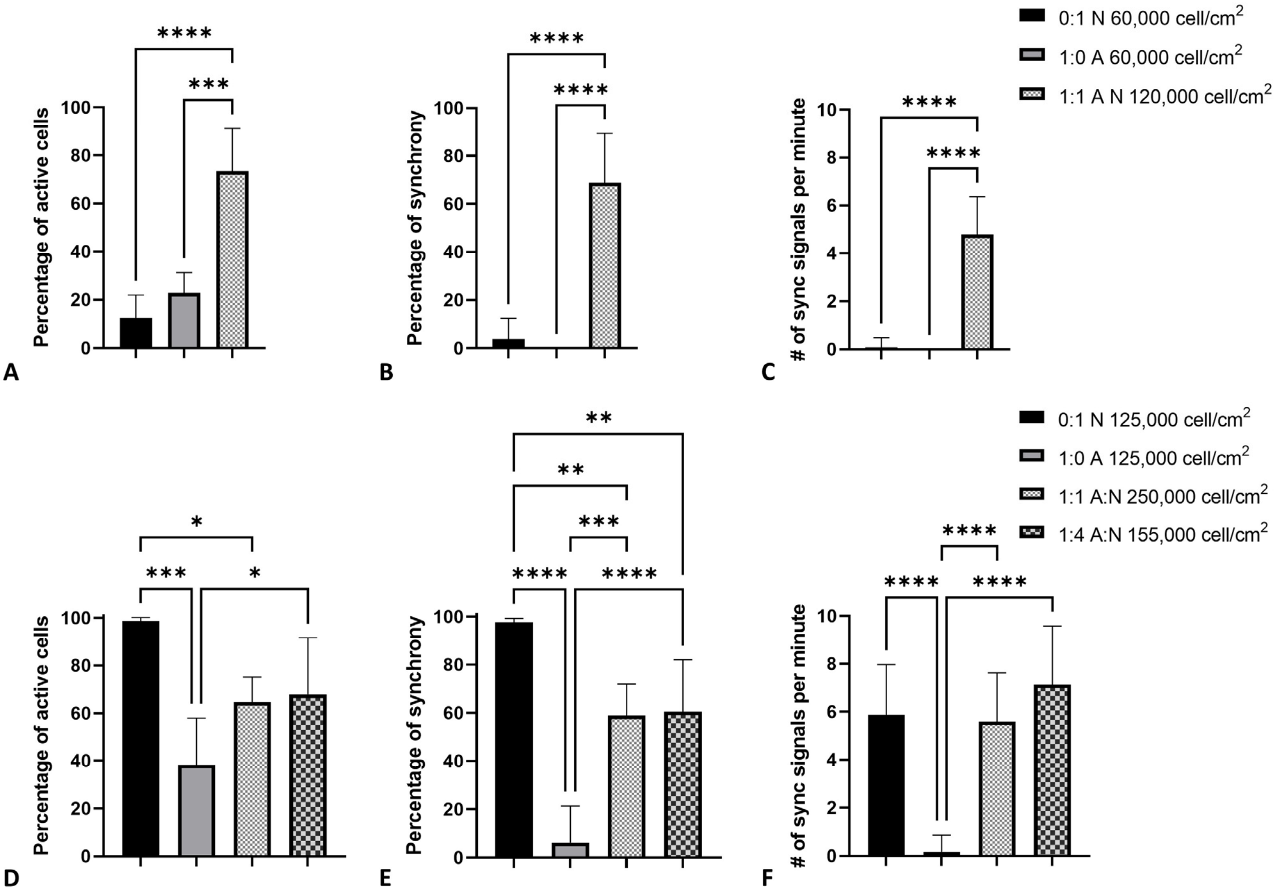

Figure 3.14 The influence of astrocytes on neuronal network functionality
Using calcium staining monitoring, the activity (A), connectivity (B) and peaking rate (C) were plotted for cells in monoculture of low density neurons, monoculture of low density astrocytes and 1:1 co-cultures of low density neurons and astrocytes at day 14 of astrocytes and day 9 of neurons in culture (N = 4). The quantification of calcium fluctuations were plotted for the activity (D), connectivity (E) and peaking rate (F) of high cellular concentrated cultures of monocultured neurons, monocultured astrocytes, 1:1 co-cultures of neurons and astrocytes and 1:4 co-cultures of astrocytes and neurons (N = 5). The values of the graphs represent the average, and the error bars are the standard deviation.

3.2.3 Neurons prefer to grow on soft astrocytes

Here, immunostaining was used to monitor cell construction in different types of co-cultures in order to understand the interaction between brain cell types (Figure 3.15A). Calculated average gray values in co-cultures seeded in layers showed that neurons (Tuj-1 positive) maximum intensities located 2 µm above astrocytes (GFAP positive) (Figure 3.15C). Similarly, neurons maximum intensities in pre-cultivation mixed co-cultures were arranged 1 µm above astrocytes (Figure 3.15D). This prompted us to look furthermore to observe how far monocultures grow away from the substrate surface. As seen in Figure 3.15B, the maximum intensity of GFAP in monocultures of astrocytes was arranged 31.7 µm from surface while the maximum intensities of Tuj-1 marker in monocultures of neurons were located 36.9 µm from the surface.

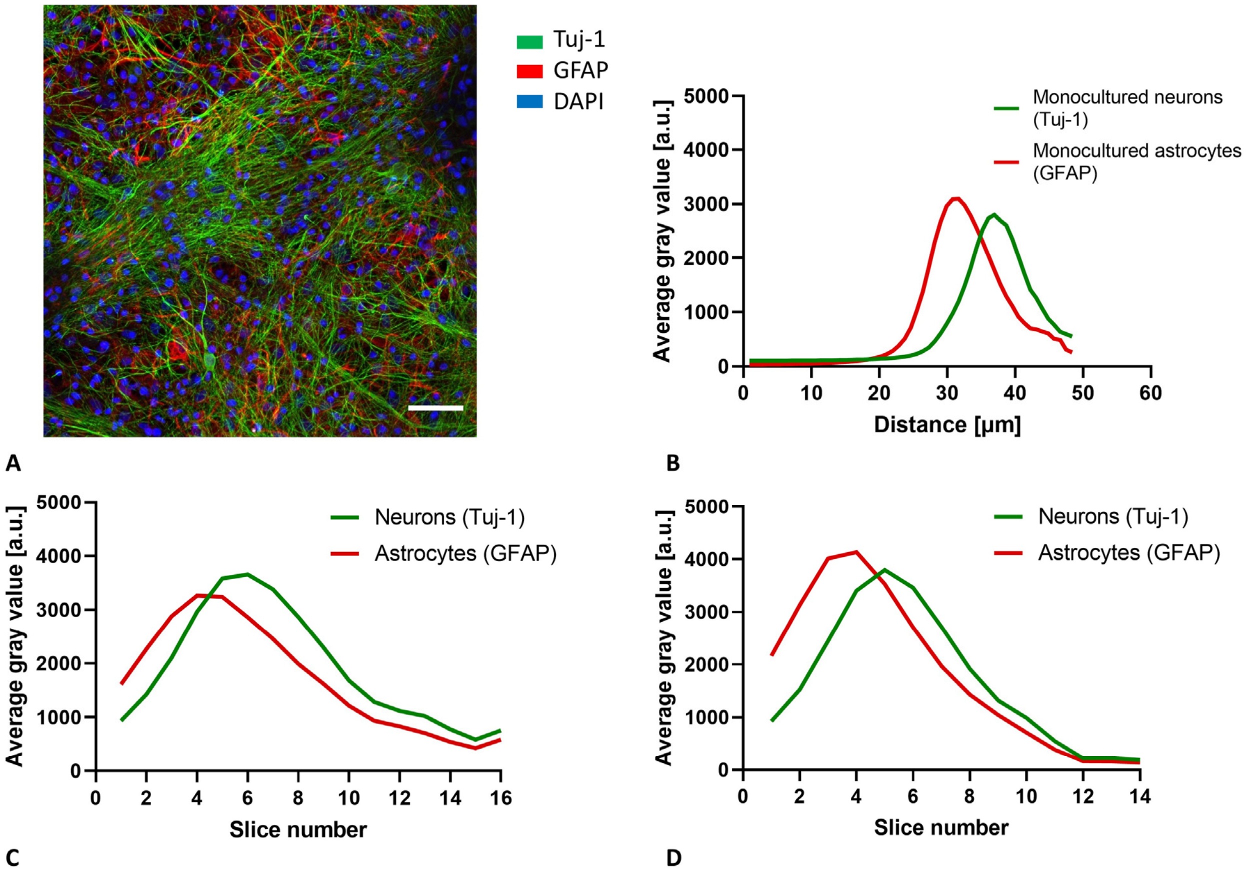

Figure 3.15 Co-cultured neurons and astrocyte construction
Co-culture of astrocytes and neurons in a ratio of 1:4 was fixed at day 9 and labeled by immunostaining antibodies against GFAP (red), Tuj-I (green) and nucleus (blue), scale bar = 50 µm (A). By calculating average gray value in every imaged slice (slice thickness = 1 µm), the maximum intensities of astrocytes and neurons were plotted with distance from culture bottom surface (detected by surface reflection) for

monocultures of neurons and astrocytes (N = 4) (B). Using the same immunolabeling, the maximum intensities of astrocytes and neurons markers were plotted over slices for 1:4 layered co-cultures (N = 7) (C) and 1:4 mixed co-cultures (N = 5) (D).

3.2.4 Co-cultures bear TBI deformation and can adapt to it

To study cell type-specific interactions and their post-injury effects, astrocytes were added to neurons in strained culture. After applying rapid stretch deformation on monoculture of astrocytes, the activity was not significantly changed directly or 24 h after stretch and kept in a range between 40 to 60% (Figure 3.16A). However, after 72 h the activities of both unstretched and stretched samples were strongly decreased to 10 and 18%, respectively. In contrast, immediately after neurons and astrocytes in a layered co-culture were exposed to rapid deformation the activity was changed from 57% in unstretched samples to 17% after stretch and the connectivity was entirely gone (Figure 3.16B, C). The activity recovered after 24 h but it took 72 h for the connectivity to regain significantly. Whereas, mixed co-cultures had more stable activity with severe stretch but the connectivity was immediately lost after rapid stretch and the complete recovery took 72 h. It is worth noting that the rate of synchronized firing peaks was two times higher in layered co-cultures compared with the mixed co-cultures frequencies.

To observe how cell viability is affected one day after extreme rapid stretch injury, a live/dead staining was assessed by flow cytometry. By looking at figure 3.16D, it is illustrated that cellular viability was stable and none of the different cell type cultures was altered in terms of percentage of dead cells compared with controls from unstretched cell-type.

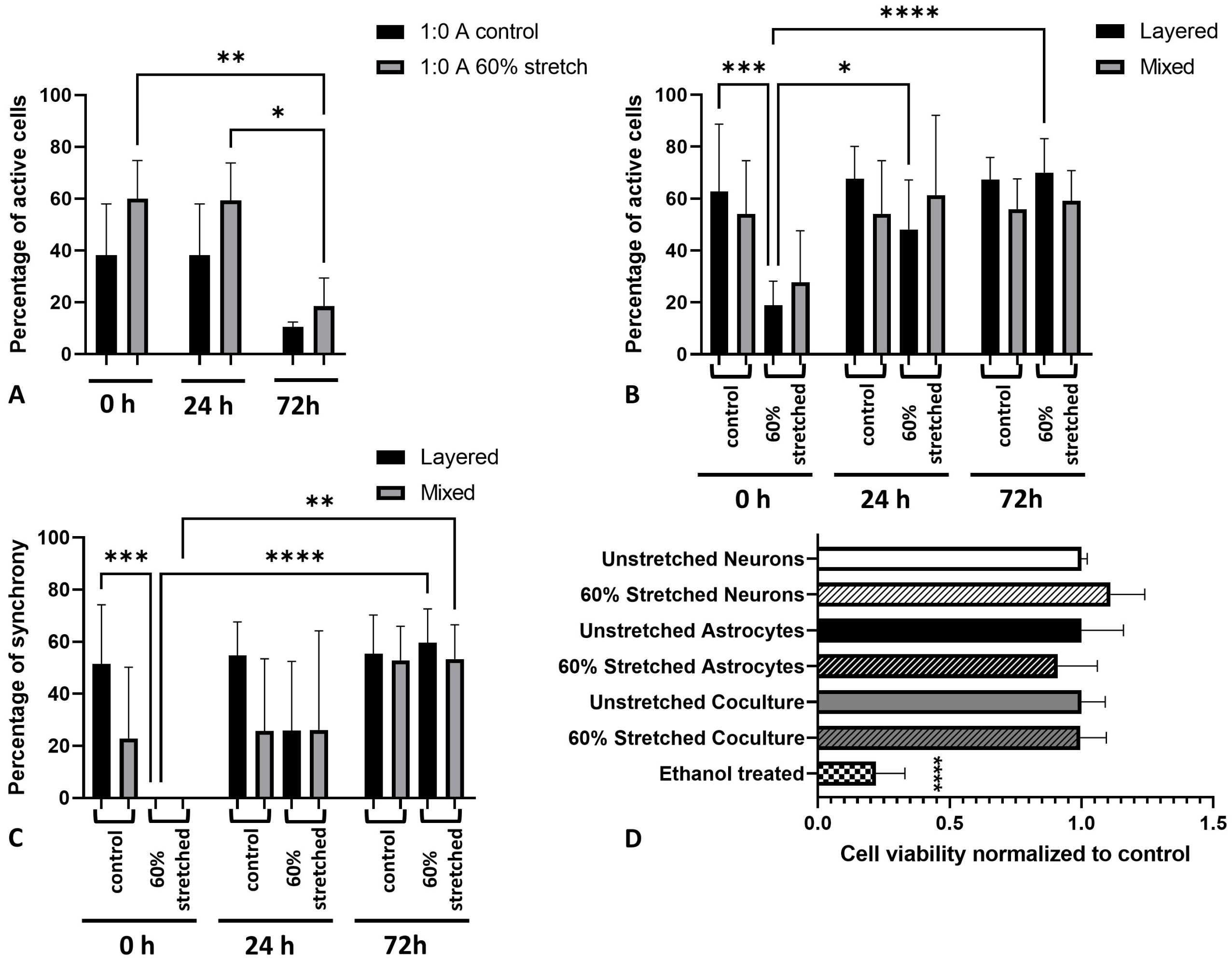

Figure 3.16 The behavior of co-cultured neurons with astrocytes towards TBI

Using calcium imaging, the calcium intensity changes were plotted for the activity of monocultures of astrocytes (125,000 cell/cm^2) (A), the activity (B) and connectivity (C) of 1:4 layered and mixed cultures (30,000 cell/cm^2 of astrocytes and 125,000 cell/cm^2 of neurons) with their changes immediately, 24 and 72 hours after a single 60% rapid stretch. Using flow cytometry analysis, the relative cell viability was plotted after 24 hours of a single 60% rapid deformation for monocultures of neurons, monocultures of astrocytes and co-cultures of neurons and astrocytes (D). The efficiency to the test was confirmed by death detection in ethanol-treated cells. The values of the graphs represent the average, and the error bars are the standard deviation (N = 4).

3.3 Evaluation of cell/neurite ablation effects on neuronal circuits

To study the impact of minimally invasive laser nano-surgery in neuronal tissue on the reaction of spontaneous spiking events of the surrounding cells, a pulsed UV laser was used on 9 DIV primary neuronal cultures to trigger selective single neuron or single neurite (axon or dendrite) death. The ablation of cell/neurite induced by laser was confirmed from the mechanical disruption of the target cell as seen in phase contrast channel in figures 3.17A and B. Also it is confirmed by the sudden change in intracellular Ca^{2+} intensity upon ablation as illustrated in fluorescence images in figures 3.17C and D. The networks were continuously monitored before and after the ablation to give a robust assessment of the induced changes in the network activity, connectivity, Ca^{2+} intensity change and recovery times, as well as detection of changes in immunofluorescence functional and cytoskeletal markers.

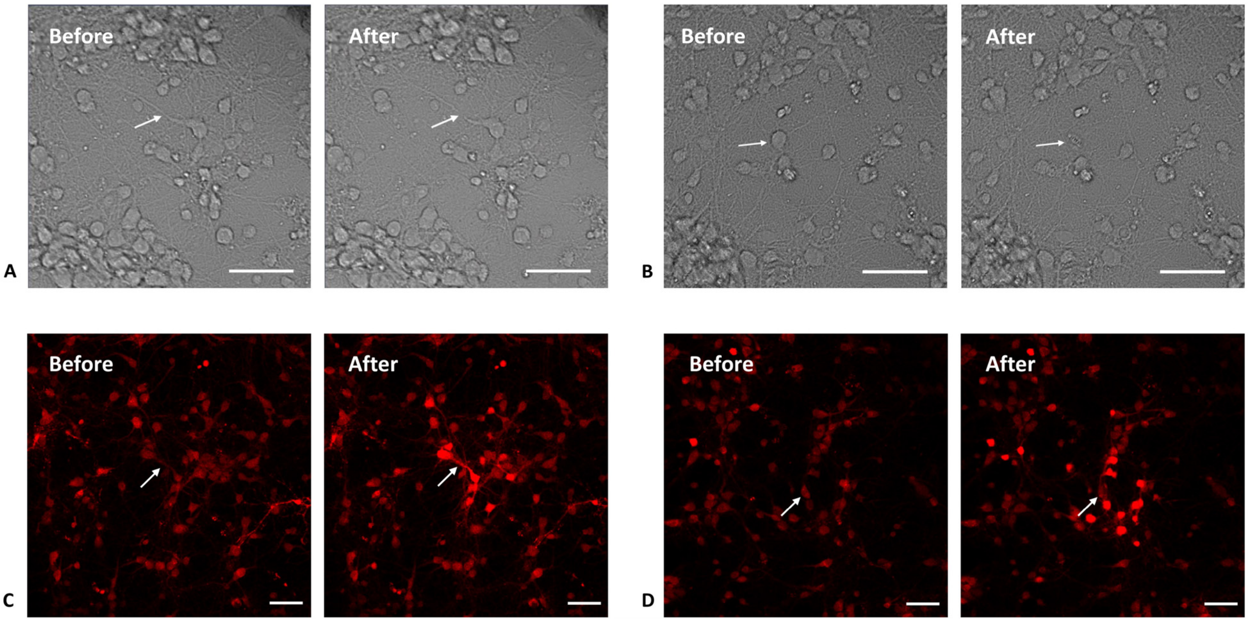

Figure 3.17 Laser-induced cellular ablation resulted in [Ca^{2+}]i-increase in surrounding neurons
Microscopic bright-field imaging of neuronal networks at day 9 in culture is showing before and after images of neurite disconnection (A) and soma ablation (B) induced by pulsed UV laser. Microscopic fluoresces imaging of calcium in neuronal networks (in red), stained with Cal-590, before and after neurite (C) and soma (D) ablation. Ablation points are indicated with white arrows. Scale bar = 50 µm

3.3.1 Single neuron/neurite ablation results in increased [Ca^{2+}]i

To detect functional changes of neuronal network upon ablation, [Ca^{2+}]i-changes in neuronal cells were recorded and quantitatively evaluated. Upon binding of Ca^{2+} to cells, fluorescence intensity of Cal-590 indicator was displayed as grey values averaged from all neurons in each 20 µm ring for every time point (Figure 3.18A). Plotting the changes in fluorescence intensity over time for each analysis ring (Ring 1-10) showed a solid increase in [Ca^{2+}]i in surrounding cells over time. This elevated Ca^{2+} spike was induced irrespective of whether cells soma or neurite was ablated in the culture, as seen from the time series fluorescence images in figure 3.17. This suggested an increase in basal [Ca^{2+}]i after ablation, particularly in cells in the vastly affected region.

3.3.1.1 [Ca^{2+}]i propagates rapidly post-ablation

To quantify how fast the increase of intensity wave travels away from the cut spot, the time-point of maximum intensity (t[Ca^{2+}]max) for each ring was determined as illustrated in red squares in figure 3.18B and C. Since spiking activity of neurons hindered the precise determination of the maximum intensity time-point as explained in section 2.2.6.3.a, propagation speed was quantified from slowly varying signal of Ca^{2+} intensity. Ca^{2+} spreading speeds were calculated across a distance of up to 200 µm (Ring 1-Ring 10) from the ablation point. Only the rings affected by ablation with at least one-fold increase in [Ca^{2+}]i were selected for propagation speed analysis. Thus, only the cells within 100 and 120 µm away from the ablation could be selected in soma and neurite ablation analysis, respectively. Ploting radial Ca^{2+} propagation speed with distance evidently showed the difference in Ca^{2+} propagation behavior between cutting a neurite and a cell. By following the maximum intensity time-point (t[Ca^{2+}]max) for surrounding rings after neurite ablation, we noticed a time delay between one ring and the next ring. Ring 2 reached its maximum intensity after 8 seconds while ring 6 requires 24 seconds, proposing that Ca^{2+} propagated along the rings started from the ablation point. The radial Ca^{2+} propagation speed across each ring was measured with speed unit of µm/s, and it ranged from 4 µm/s to 7.5 µm/s in single-neurite ablated cultures (Figure 3.18D). On the contrary, laser-induced neuron soma ablation resulted in an intensity increase in the neighboring rings with a nearly similar time range of between 8 to 13 seconds independent of distance from the point of ablation. Figure 3.18E shows that the propagation speed after soma ablation was faster, as it started with a speed of 3 µm/s in ring 2 and increased to 12 µm/s in ring 5.

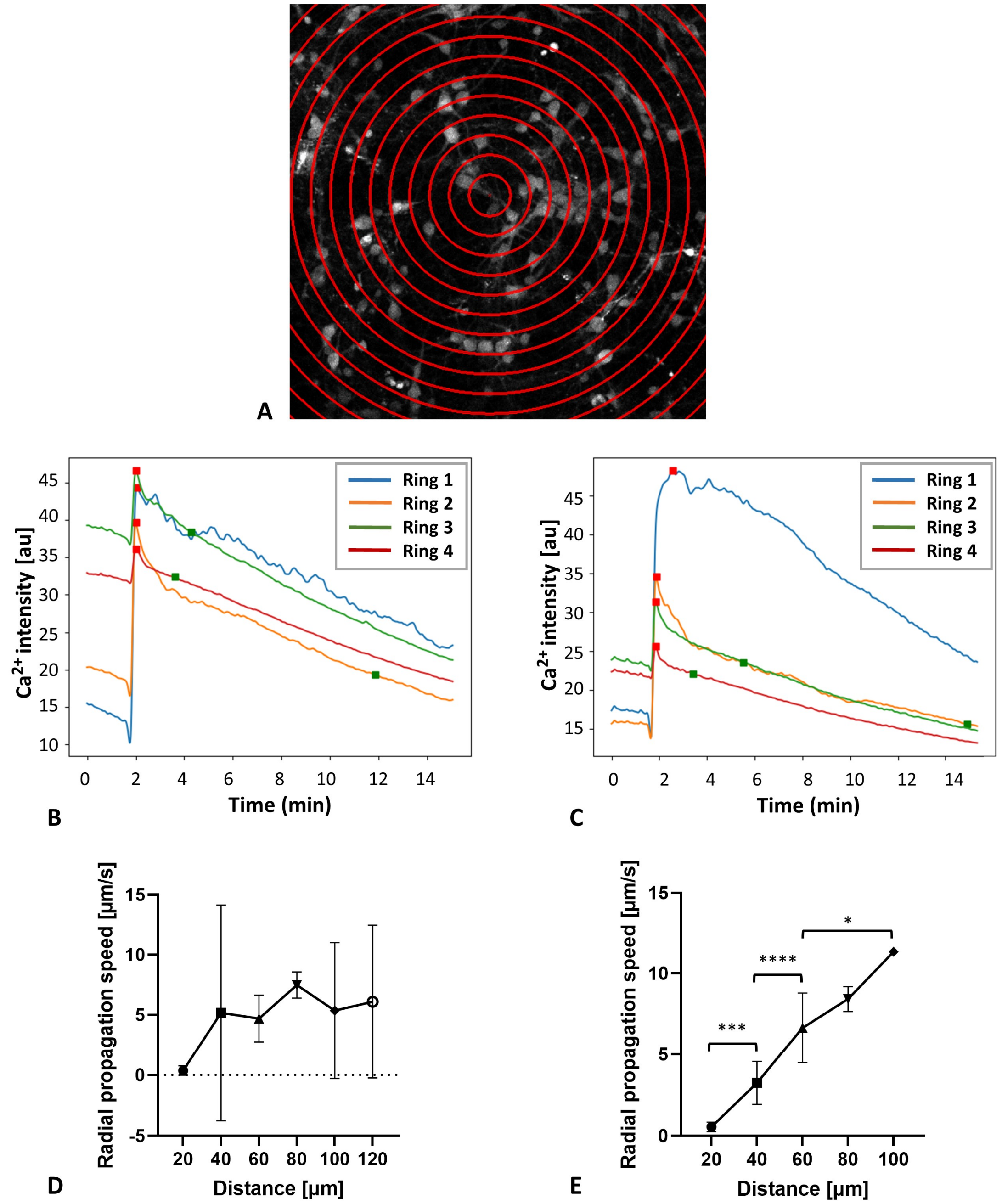

Figure 3.18 Ablation-induced radial Ca^{2+} propagation speed in neuronal network
A microscopic image of cultured neurons showing the rings used for analysis of Ca^{2+}-induced fluorescence intensity-changes. Concentric rings of 20 µm width were generated around the ablation point (in red) (A). Ca^{2+} intensity average gray values (slowly varying fluorescence signals) in neurons were plotted over time showing the changes before and after neurite (B) and soma (C) ablation. The time-point of maximum fluorescence intensity after ablation is marked with a red square for each analysis ring. The time-point of Ca^{2+} intensity full recovery is marked with a green square for each analysis ring. Plots represent mean radial Ca^{2+} propagation speed along neurons with distance from the ablated neurite (D) and soma (E). Ca^{2+} propagation speed is plotted only for the significantly affected cells due to Ca^{2+} inflow. Error bars represent the standard deviation (N = 11).

3.3.1.2 Ablation-induced [Ca^{2+}]i increases more in surrounding cells

Laser ablation resulted in an immediate loss of Ca^{2+} intensity in ablated spot, followed by a sharp increase in Ca^{2+} intensity observed in surrounding neurons up to 120 µm away (Ring 1 to 6) with time. To determine the number of fold-change in each neighboring ring of neurons, the fraction of maximum Ca^{2+} intensity after ablation to the previous mean intensity before ablation was calculated. The intensity change assessment indicated that the increase was higher in cells adjacent to the ablated point compared with the cells located farther. From figure 3.19A and B it is illustrated that the first 20 µm ring showed the highest induced concentration increase of 3.5 folds and 2.3 folds in ablated neurite and soma, respectively. The level of rise in Ca^{2+} concentration was less with distance. Additionally, the magnitude of ablation-induced Ca^{2+} increase was almost comparable in all the further rings in both types of ablation, with a rise between 1 to 2 folds.

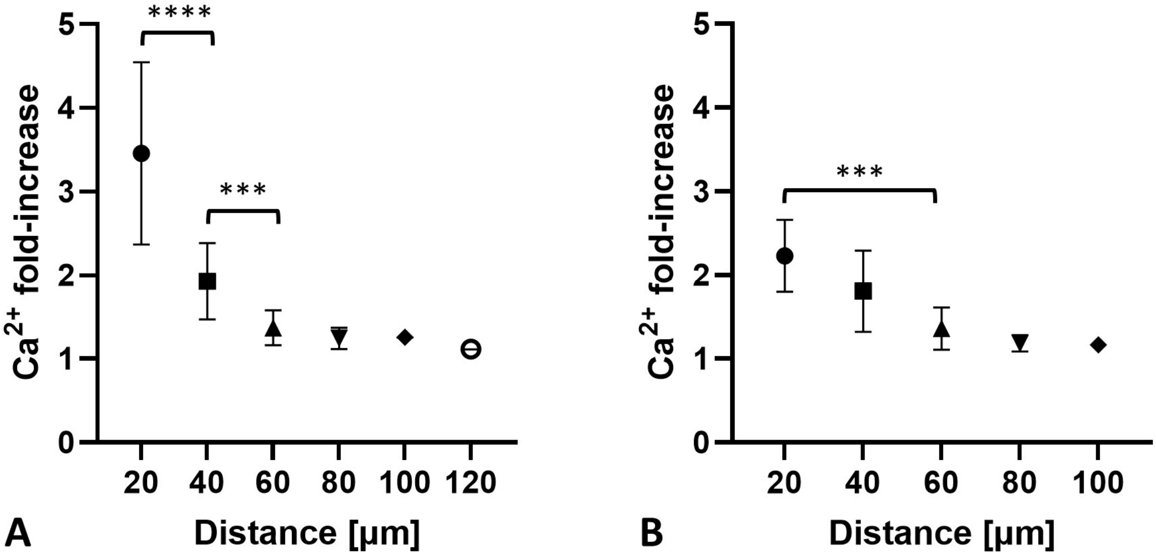

Figure 3.19 Ablation-induced increase in Ca^{2+} intensity
Graphs showing mean [Ca^{2+}]i-increase in cultured neurons with distance from ablated neurite (A) and soma (B). Ca^{2+} fold-increase is plotted only for rings which increased by 1 fold at least. Error bars represent the standard deviation (N = 11).

3.3.1.3 [Ca^{2+}]i of neurons recover gradually after ablation

The increase in intracellular calcium levels was found to be temporary. With time, it is observed that ca^{2+} intensity started to decrease beginning with distantly affected neurons first towards the ablated spot. To estimate the time-point of full intensity recovery, a python script was used to detect the earliest time point after ablation when each ring intensity is identical to its initial value before ablation (described in 2.2.6.3.c), as illustrated in green squares in figure 3.18B and C above. The results graphed in figure 3.20B shows that after soma ablation the [Ca^{2+}]i recovered gradually with time starting from further cells to closer cells adjacent to ablated cell. Within 15 mins of soma ablation, around 65% of samples showed a recovery in the area of 20 µm around dead cell, while almost all the samples showed an earlier recovery of cells in further areas between 40 and 100 µm (Ring 2-5) around ablated soma. In contrast, cells in the area between 40 and 120 µm (Ring 2-6) around ablated neurite required longer times to recover compared with soma ablated samples (Figure 3.20A). Besides that none of the neurite-ablated samples recovered their initial calcium intensities in the area of 20 µm around neurite ablation point. Taken together, these outcomes evidently suggested a higher degree of [Ca^{2+}]i-increase with a slower recovery to original levels in the closely connected cells compared with farther located cells in both neurite and soma ablation. Besides that the propagation speed after neurite ablation was scattered between samples and slower than the fast propagation detected after soma ablation.

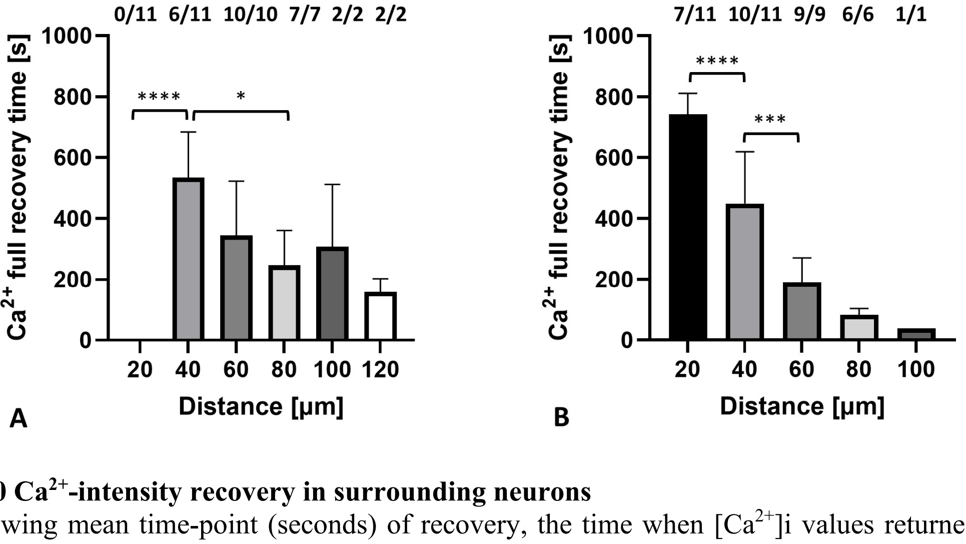

Figure 3.20 Ca^{2+}-intensity recovery in surrounding neurons
Graphs showing mean time-point (seconds) of recovery, the time when [Ca^{2+}]i values returned to mean values before ablation, in neurons at different distance from the ablated neurite (A) and soma (B). The error bars show standard deviation (N = 11). The numbers above each column represents the number of recovered samples to the number of affected samples in terms of Ca^{2+} intensity changes.

3.3.2 Calcium spiking activity is recoverable after ablation

Imaging of calcium changes with ablation showed an increase in calcium intensity in adjacent neurons upon ablation, followed by a briefly interrupted spiking activity. However, neurons located far from the ablation point continued spiking without disruption. To explore this behavior in details, Ca^{2+} intensity in cells was plotted with time before, during and after ablation, also cells were monitored for the long-term impact after 24 h of ablation.

3.3.2.1 Overall network functionality is stable after laser-induced ablation

To investigate how a single-neurite/soma ablation is affecting the overall neuronal network firing activity, the calcium fluctuations of all detected cells in the field were analyzed using the method described earlier in 2.2.3. Regardless of the cell location, calcium concentration was plotted for all neurons with time as F/F0 ratio, where F is the intensity of fluorescence at any given time and F0 is the mean intensity of fluorescence before ablation. Figure 3.21A illustrates that the cultures of neurons were dynamically active before ablation with an activity percentage over than 95% of the cells. Upon ablation, neither neurite ablation nor soma ablation caused any observed change in activity percentage. Still more, the percentage of active cells kept stable for 24 hours after ablation. When we looked at connectivity of active neurons before ablation, we found that neurons had rhythmic Ca^{2+} peaks where more than 85% of cells participated in these peaks simultaneously (Figure 3.21B). Despite of losing a cell or a single cellular connection, the overall connectivity percentage did not remarkably decrease after ablation or after 24 hours later. Moreover, there were no significant decrease in the frequency of synchronized peaks (Figure 3.21C), or any increase in random signals rate and time with ablation (Figure 3.21D). These outcomes suggested that the global network functionality is constant with ablation, however a closer look to the firing behavior of each ring surrounding ablation point is necessary.

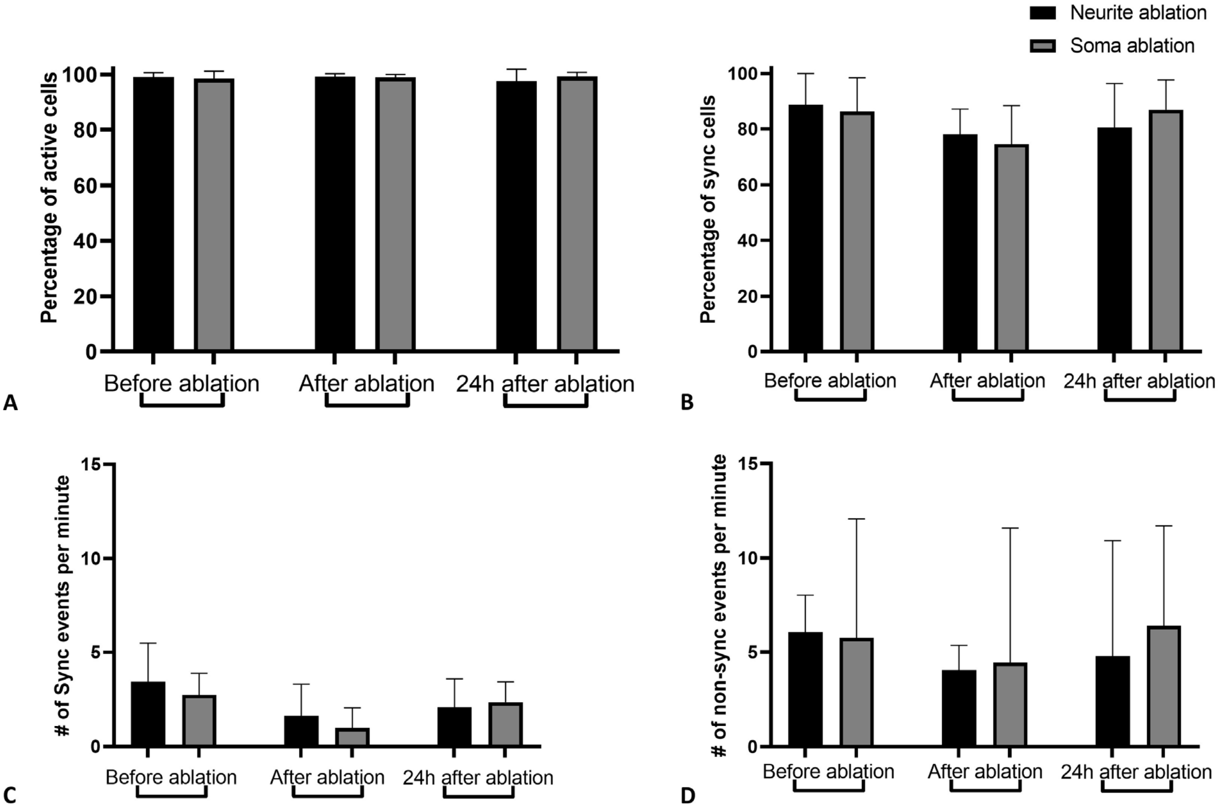

Figure 3.21 Analysis of overall spiking activity in neurons before and after ablation
Global Ca^{2+} activity behavior was analyzed before, directly after ablation and 24 hours later. The plots are showing an unchanging percentages of active cells (A) and synchronizing cells (B) after neurite and soma ablation. The spiking frequencies of synchronized (C) and unsynchronized peaks (D) were represented as number of peaks per minute. The values of the graphs represent the average, and the error bars are the standard deviation (N = 11).

3.3.2.2 Neuronal connectivity upon ablation is distance-dependent

To spot the influence of laser ablation with a detailed evaluation of cellular connectivity, we used the rings analysis method as explained in section 2.2.6.3.d. To measure signals similarities, the calcium signals of every ring (as shown in figure 3.22A, B, C) were cross correlated with each other ring and the maximum of each cross correlation was plotted. These plots define identical signals with a correlation coefficient of 1 and if they are completely different then the correlation coefficient will be 0. The degree of similarity in the correlation plots is ranging from purple to yellow to represent gradual connectivity from 0 to 1, respectively. The degree of connectivity in neuronal network before ablation was very high between all the rings up to 200 µm with a similarity coefficient between 0.8 and 1 (Figure 3.22D, G). Once the laser ablation was applied to a single spot, the correlation between the close rings and the further rings was reduced (Figure 3.22E, H). The first ring nearby the ablation-point, the area of the most affected cells, had a dark blue correlation coefficient of 0.3-0.4, while the second ring had a connectivity coefficient of around 0.5. In the same way, the cells in the rest of rings were slightly affected depending on their distance from the ablation point. By monitoring the cultures after 24 h of ablation, the correlation coefficient in the affected rings recovered its values to more than 0.8 and the connectivity was regained (Figure 3.22F, I). These findings also confirmed the distance-dependent effect of single-cell/neurite death and also the time-dependent recovery.

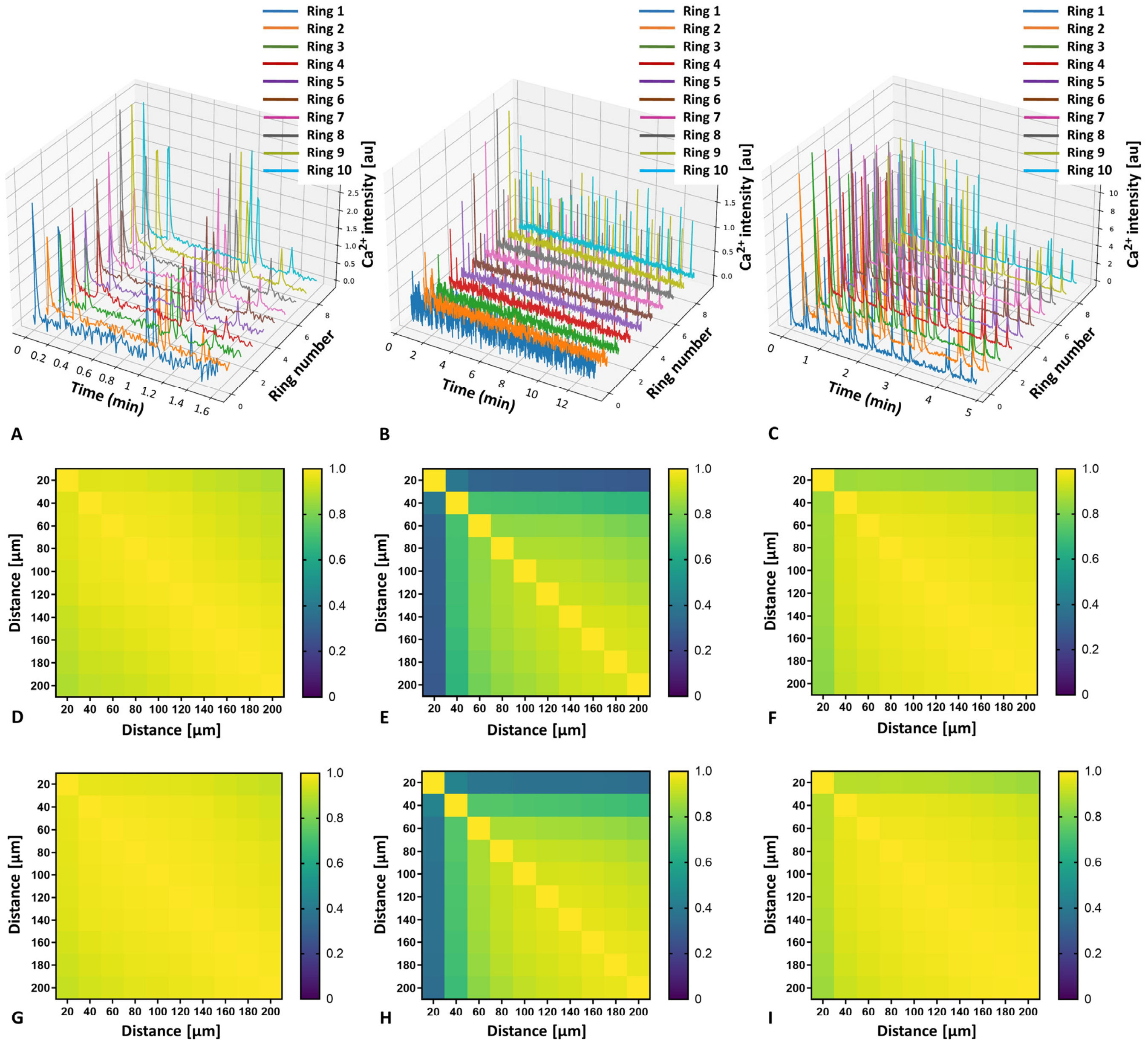

Figure 3.22 Analysis of spiking activity correlation between neurons with ablation
Baseline corrected average gray values of Ca^{2+} signals for ring 1 to 10 (0-200 µm) around an ablated neuron were plotted before (A) and after ablation (B) and 24 hours later (C). The maximum cross correlation analysis of Ca^{2+} signals between all rings was plotted before (D, G), after (E, H), and 24 hours after (F, I) neurite and soma ablation. The degree of similarity in the correlation plots is ranging from purple to yellow to represent gradual correlation coefficient from 0 to 1. The values of graphs represent the average, N = 11.

3.3.3 Functional synaptic proteins remain unaffected upon ablation

To assess the impact of a minimal laser ablation on synapsis formation, double immunolabeling for pre- and post-synaptic markers was used (Figure 3.23A). Colocalization of presynaptic marker, synaptophysin, and postsynaptic marker, PSD-95, was calculated to focus on mature synapses. The cortical neurons used for laser ablation experiments were 9 days old and fixed directly after laser ablation to be labeled later with immunostaining. Another group of samples was only fixed 24 hours after ablation (DIV 10) to measure the long-term effect on synapsis marker densities. The quantification of average gray values (described in section 2.2.8.4) of the presynaptic marker in each ring showed a constant level after neurite/soma ablation (Figure 3.23B, C). Moreover, when gray values of each ring was compared with the values detected after 24 hours, they were in the same range. In the same way, the assessment of postsynaptic marker revealed that the gray values were in the same range in all the rings after being exposed to laser ablation and after 24 hours as well (Figure 3.23D, E). The evaluation of mature synapses integrity up on ablation, illustrated in figures 3.23F and G, revealed a slight decrease in the first ring. However, this reduction in the calculated gray values was not significant.

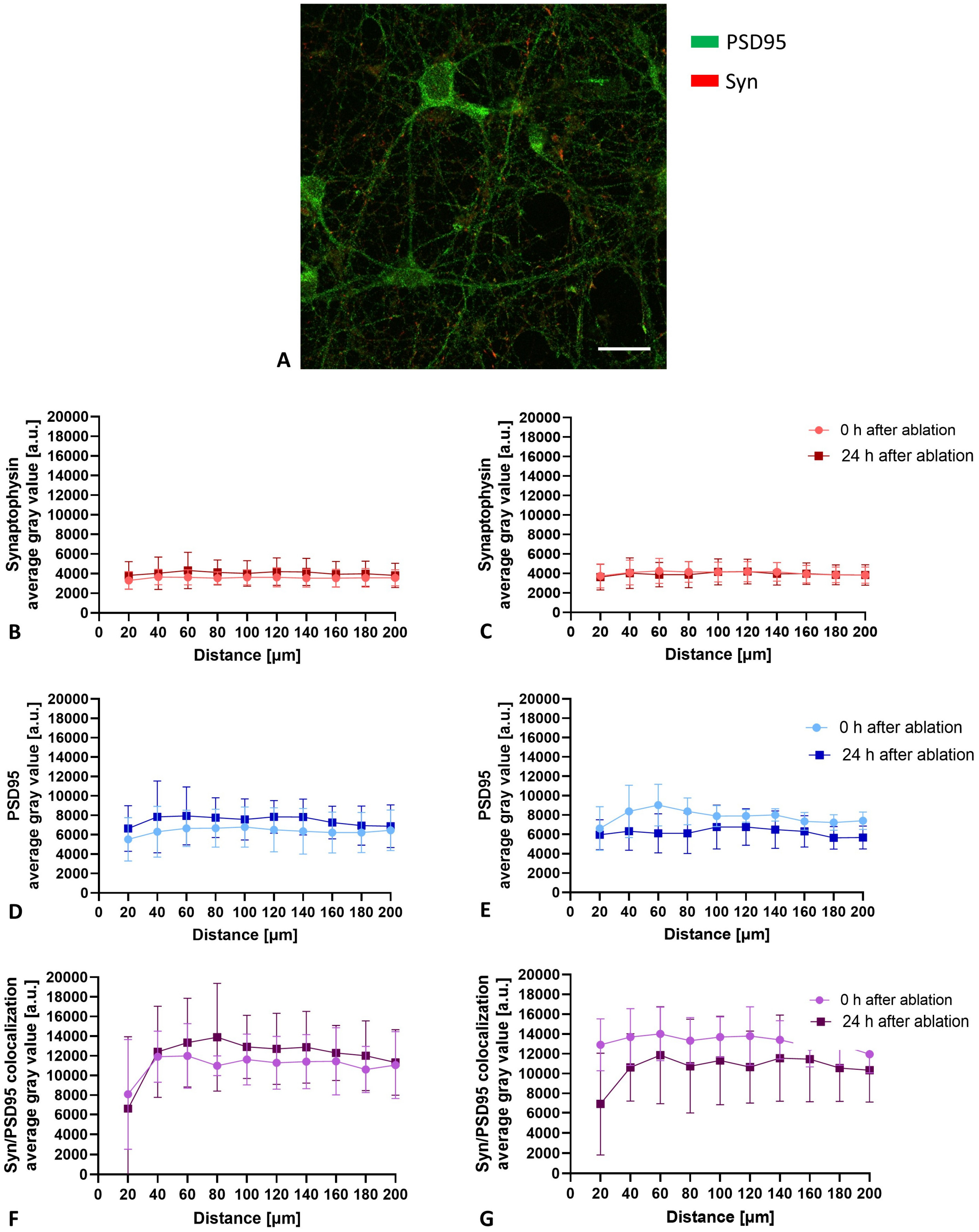

Figure 3.23 Analysis of synaptic proteins in neurons with ablation

Cortical neurons were stained against synaptophysin and PSD-95, pre-synapses are indicated in red while post-synapses are indicated in green (A). Scale bar = 20 μm. From the analysis of immunofluorescence imaging, the average gray values of synaptophysin channel were measured for each ring and plotted for neurite (B) and soma (C) ablated cultures directly after ablation and when measured after 24 hours. In the same way, the average gray values of PSD-95 channel were plotted in each ring surrounding neurite (D) and soma (E) ablation point. Average gray values of synaptophysin and PSD-95 colocalization were plotted to estimate mature synapsis integrity in the short and long term after neurite (F) and soma (G) ablation. The graphs represent the average values, N = 5.

3.3.4 Cytoskeletal proteins remain stable upon laser-induced ablation

To examine the influence of laser ablation on neuronal cytoskeleton degradation and regeneration, two of the main components of neuronal cytoskeleton were analyzed according to average gray values of immunofluorescent intensity in each ring. Immunofluorescent labeling against actin and tubulin were used to see how networks undergo cytoskeletal adaptation to minimal ablation (Figure 3.24A). After neurite ablation, a slight reduction in both actin and tubulin intensities was detected in the first adjacent rings as an immediate reaction and after 24 hours of ablation, but this decrease is not considered a significant change (Figure 3.24B, D). Similarly, no remarkable changes in intensities of cytoskeletal markers, actin and tubulin, were detected in single soma ablated networks directly after ablation or on the long-term (Figure 3.24C, E).

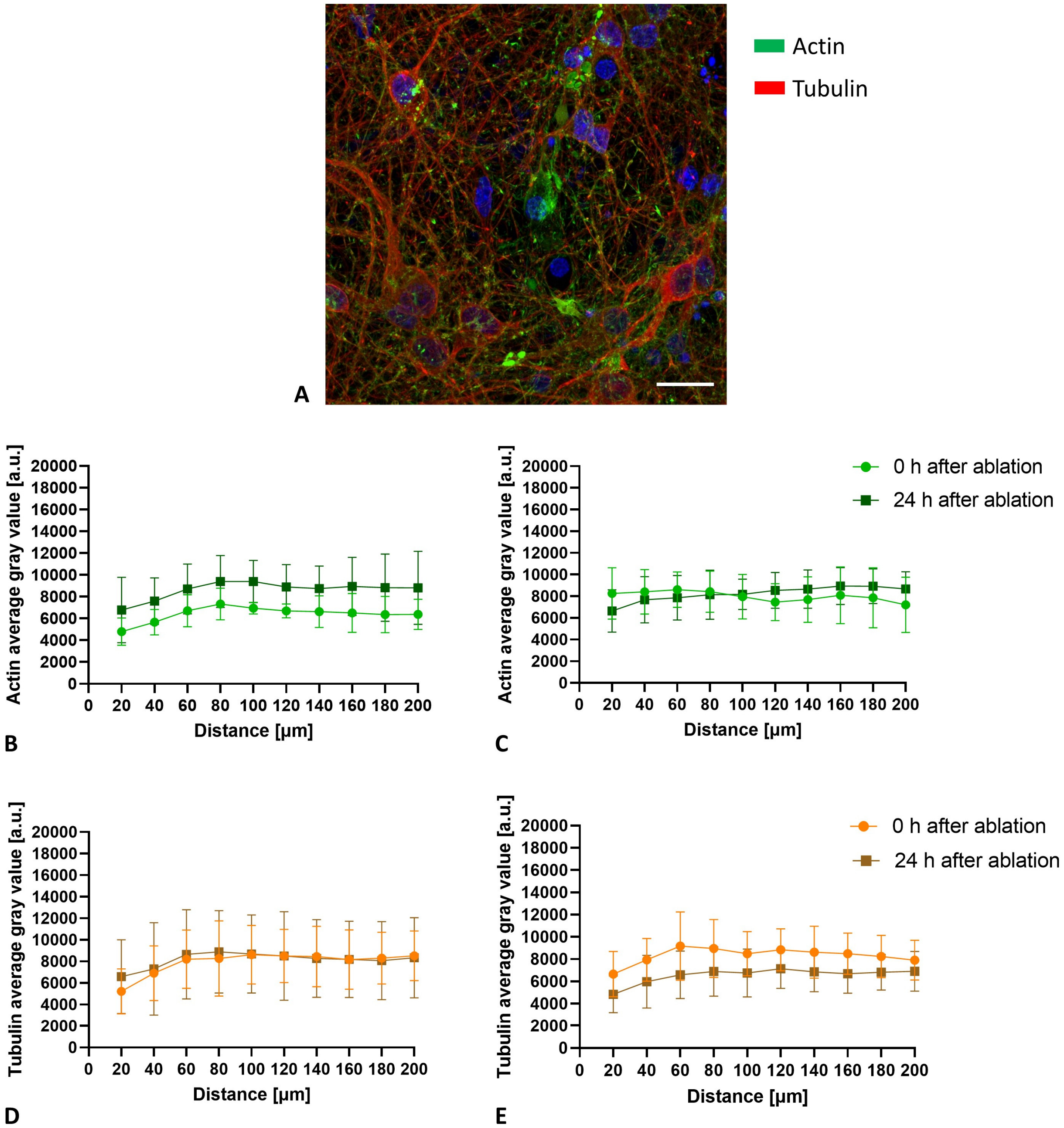

Figure 3.24 Analysis of structural proteins in neurons with ablation
Cortical neurons were stained against actin and tubulin. Actin is indicated in green and tubulin is indicated in red while nuclei is in blue (A). Scale bar = 20 µm. From the analysis of immunofluorescence imaging, the average gray values of actin channel were measured for each ring and plotted for neurite (B) and soma (C) ablated cultures directly after ablation and when measured after 24 hours. In the same way, the average gray values of tubulin channel were plotted in each ring surrounding neurite (D) and soma (E) ablation point. The graphs represent the average values, N = 6.

4 **Discussion**

Like other cell types, brain cells are exposed to internal and external mechanical displacements and tension. These forces range from daily life physiological stretches (5-30%) (Bayly et al., 2005; Wedeen and Ponceleti, 2007; Fleming et al., 2011), to higher strain that initiate traumatically brain injuries (Waxweiler et al., 1995; Gamburg et al., 2000). Lately, mechanical forces are gradually more considered as one of the main parameters in growth and pathology of neurons (Wozniak and Chen, 2009; Franze and Guck, 2010). Yet, few studies have been made to understand mechanical strain influence on short and long term functionality of cortical neurons in terms of active synapses and action potentials. Here, in this thesis, the in vitro functional behavior of neuronal monocultures and co-cultures with astrocytes was investigated. The cellular responses to different modes of mechanical forces were explored and discussed.

4.1 Neurons are equipped to bear mechanical loads

The development of cortical spines begins within the first week after birth in rats and the number continue to increase during the first month (Wise et al., 1979; Nimchinsky et al., 2002; Yuste and Bonhoeffer, 2004), together with the establishing of synapses and functional circuits (Stern, et al., 2001; Bureau, et al., 2004). Preliminary optimizing experiments of cultured embryo cortical neurons revealed that neurons activity in vitro is cell growth and density dependent, as low cell concentrations at 7-9 DIV show slow and random neuronal firings while cultures with higher cell concentrations have faster firings with a network synchrony behavior. To identify activity responses to the different stretching types, live-cell imaging of calcium fluctuations and stress markers staining were performed without strain and after strain.

4.1.1 Robust action potentials and synapsis under stretching

Ca^{2+}, a cellular second messenger, is engaged in the signaling of several functions in cell. $[Ca^{2+}]i$ balance is firmly maintained in cells by pumps, ion channels and associated transport proteins (Carafoli, 2002; Bagur & Hajnóczky, 2017). Combining mechanical stretching with live-calcium imaging, enabled us to detect the behavior of neurons upon stretching. Many previous studies proved that mechanical deformations applied physiologically on cortical neurons can improve axonal growth and formation of new branches (Lamoureux et al., 2002; Pfister et al., 2004; Abraham et al., 2019). Our results show that probably this continuously repeated stretching is not sufficient to enhance communication between cells in culture. Obviously, from our trial of mild stretching of single cells at early developmental stages there was no noteworthy differences between early-stage cyclically stretched and unstretched neurons by the number of active cells, firing frequency, synchronous firing beaks or any change in number of formed synapses.

Remarkably, regular cyclic stretching do not interfere with neuronal function when applied on the network level at stages of early development and without any changes in calcium fluctuations, connectivity between cells or synapses formation. These results are in line with previous reports from Loverde and Pfister (Loverde and Pfister, 2015), showing that axonal growth induced by slow stretching did not alter electrical motion of sensory neurons. These results proposes that normal axonal lengthening induced by cyclic stretching is different than traumatic axon injury. At low strain amplitude, it is likely that the cell membrane go through an adaptive mode, which is limiting the changes in its mechanical state.

Moreover, neuronal network can functionally adapt to mild and harsh (15-30%) periodic stretching without loss in neuronal communication when strain is performed after network formation level, which is simulating tension of regular body movements. Cultured neuronal networks verified to be robust even when mechanical tension is focused on aligned neurites. These results show that the process of growth by stretching is not associated with transportation of calcium signals between neuronal cells.

The experiments of rapid deformation and slow static stretch with extreme amplitude suggests that functional tolerance to injuries have high threshold and that connections between neurons in network are stronger than expected with a high capability to restore disconnections. Despite that result, other studies describing the effect of numerous strain rates on neural injury vary. Most reports indicate that non-developmental strain rates as high as 30 s^{-1} (Magou et al., 2015) and as low as 0.008 s^{-1} (Shi and Whitebone, 2006) induce a damaging effect on neural activity. Latest computational and experimental studies revealed that the damage of ion channel is an important reason to explain the reduction in action potentials caused by neuron strain (Kwong et al., 2019). In addition, it is widely linked with increased membrane permeability to large molecules (Slemmer et al., 2002; Prado et al., 2005).

Experimental results imply that the mechanical stretch effect on neuronal functionality depends on both the rate and magnitude of applied deformation. Moreover, the onset of loss in electrical connectivity between cortical neurons occurs directly during stretch and recovered within 24 hours even if stress is not removed. Many axonal regeneration pathways are discovered, such as triggering a conserved kinase cascade including the dual leucine zipper kinase (DLK). However, the route of repair is not fully understood yet and additional investigations are required.

4.1.2 Secondary neuronal response is limited upon stretching

Following the immediate results of primary brain injury induced by forces applied to tissues, other outcomes are secondary and continue to develop gradually after hours, days, or weeks later. Secondary conditions after injury can dramatically affect community participation, and quality of life (Westgren and Levi, 1998). Secondary injury reaction could cause neuroinflammatory response, oxidative stress, disruption of the blood-brain-barrier (BBB), excitotoxicity, and cell death (Chesnut et al., 1993). The major goal of therapeutic measures is based on establishing recommendations and guidelines to prevent secondary damage and reduce morbidity and mortality. Thus, it is essential to explore some secondary complications triggered after stretch-induced injuries. Directly after traumatic brain injury, an inflammatory response can be stimulated in the nervous system by regulating and secreting cytokines including IL-6, IL-8 and TNFα. The largest released quantities are from IL-6 and it was the main inducer of the acute phase reaction (Lu et al., 2017). The complex role of the IL-6 comes from being a pro- as well as an anti-inflammatory factor, because it can play both a protective and pathological role in neural tissues (Spooren et al., 2011). Previously tested mRNA levels of IL-6 in the region of traumatic brain injury have shown a considerable rise of 20-folds in the period of 6-122 hours after injury (Frugier et al., 2010; Perez-Barcena et al., 2011). However, the low expression of inflammatory marker in our experiments proposes that the applied deformations were not adequate to induce inflammation to *in vitro* monocultured neurons. This may be explained by the lack of astrocytes and their secretions which are responsible for controlling and exerting immune reactions in the brain (Cordiglieri and Farina, 2010). Despite that none of the different applied stretches initiated inflammation within 24 hours in neuronal networks, our findings in autophagy marker revealed that the type of mechanical force performed onto the neurons could significantly change both the mechanism and severity of the neuronal response to stress. Particularly, cyclic mild stretch causes higher stress for neurons than one cycle of harsh stretch in terms of detected LC3B protein accumulations to autophagosomes. In spite of the loss of neurons activity and connectivity immediately after severe stretching, none of the stretch profiles resulted in cell death within 24 hours of stretch. These outcomes suggest that changes that appeared directly after stretch had been recovered. This could be explained by the findings of Zhao and his colleagues pointing out that neuronal death is impacted by astrocyte death in rat model of TBI (Zhao et al., 2003). Also, the development of secondary conditions is affected by time since injury (Noreau et al., 2000), functional capacity and age (Middleton et al., 2004). Further investigations on secondary responses could be done after a longer period, as many inflammatory molecules peak at day 7 or after.

4.2 The role of astrocytes in neuronal signaling

Neurons are the most known and studied cell type in nervous tissues, however, at least half of the brain and spinal cord cells in humans consist of astrocytes. Astrocytes are vital for CNS health and functioning (Sofroniew and Vinters, 2010) because they are important for synapse formation, maturation, maintenance (Allen and Eroglu, 2017) and support (Bush et al., 1999). The functions of astrocytes includes emission of extracellular matrix proteins and growth factors, neurotransmitters recycling, and ion concentrations regulation (Perea et al., 2009; Clarke and Barres, 2013; Allen, 2014; Chung et al., 2015; Khakh and Sofroniew, 2015). While the molecular level of neuron-astrocyte interactions is mostly understood, the role of neuron-astrocyte communication on network dynamics are still poorly understood. Hence, using *in vitro* co-culture models that permit cell-cell interactions is a superior way for simulating the original *in vivo* physiological environments and for getting more representative brain injury responses.

4.2.1 Co-culture with astrocytes enhance low-density neuronal connectivity

From our initial experiments, we noticed an independent slow calcium signals in monocultures of astrocytes. These detected calcium signals highlight how astrocytes act as independent signaling units but with slower and fewer active peaks compared with signals of neurons. This is established by the interconnection of astrocytes with each other by gap junctions, particular channels which permit ions and nutrients to diffuse between networks of astrocytes (Pannasch and Rouach, 2013). Several studies have tested the interaction between neurons and astrocytes using in vitro co-culture systems. Some of these studies reported the effect of astrocytes on differentiation of stem cells (Ehret et al., 2015; Schutte et al., 2018), the effect on synapses formation (Pyka et al., 2011; Chung et al., 2015), and their influence during diseases (Park et al., 2001; Kidambi et al., 2008; Kunze et al., 2013). Since more functions of astrocytes were revealed lately, the importance of co-cultures of neurons and astrocytes became more obvious. We assessed here the cumulative effect of co-culturing on the connectivity of low-density individual cells and on well-connected networks by quantifying changes in spiking activity. Remarkably, neurons at very low density display repetitive synchronous spiking activity when astrocytes are present in co-culture compared with few random signals in monocultures of neurons. Our experiments showed a supportive effect of astrocytes to low-density cultures of neurons that turned them into functionally connected and active networks. These outcomes are in line with the findings of Aebersold and his colleages, reporting that adding astrocytes to cultures can significantly improve cells viability and spontaneous spiking (Aebersold et al., 2018). *In vivo*, neuronal synapses are not just composed of pre and postsynaptic neurons as in our in *vitro* pure neurons model, but in many cases synapses are also contacted by astrocyte process that play an important role in regulating synapsis and neuronal circuits activity (Araque et al., 2014). However, we found that when both cell types are present together in high cell densities they have less connectivity compared with monocultured neurons.

Additionally, we detected that the construction of cells in co-culture control their calcium fluctuation behavior. Specifically, when astrocytes and neurons are seeded in two different layers neurons have more frequent harmonized spikes than when the cells are mixed. This can imply that the astrocyte-secreted proteins play a major role in neurons activity and not only the direct connection. Moreover, we detected that the stiffness surrounding neurons *in vitro* influences their construction in culture. In vivo, astrocytes can provide mechanical support to neurons by embedding and protecting them in a soft compliant environment, since astrocytes are two times softer than neurons (Lu et al., 2006). From fluorescence microscopy observation we found that neurons in monoculture prefer to grow away from stiff surface than astrocytes do. Also, neurons have a tendency to grow on top of astrocytes when both are mixed in co-culture. These findings are supported by other *in vitro* studies and with the natural behavior of neurons *in vivo*, where neurons prefer softer surfaces which direct outgrowth and branching of neurites (Lo et al., 2000; Balgude et al., 2001; Georges and Janmey, 2005).

4.2.2 Cells in co-cultures are viable and robust against mechanical strain

Astrocytes are not only a softer surface to grow around but they are also considered protectors for neurons, because astrocytes are well known to be more resistant to injury and to regulate neuroprotection as well as neurodegradation (Ding et al., 2021). And this could be the explanation to our results revealing that the functionality of astrocytes in monocultures are resistant to severe uniaxial stretch. However, co-cultures of neurons and astrocytes lose their activity with extreme stretching injury and are able to recover the activity within 24 hours, but cellular connectivity takes 72 hours to fully regain. Astrocytes and neurons appeared to be very robust to harsh stretching. Besides its neuronal protection feature, astrocyte is a crucial element in secondary neuronal damage and repair inhibition mainly owing to its function in both the regulation of neuroinflammation and formation of glial scar after CNS injury (Liddelow and Barres, 2017; Adams and Gallo, 2018). Despite the temporary loss of activity in co-culture, none of the cell cultures types had an observed statistical difference in cell viability after mechanical strain, approving that no neuronal death occurs at noticeable levels in our experimental conditions.

Astrocyte cells are critical to the function of neurons, and adding astrocytes to neuron in cultures can enhance their quality in vitro. These results could improve our vision of mechanical injury and cell response and probably will support tissue engineering efforts to avoid nervous system injury and aid nerve repair. These conclusions could be taken further to explore cells behavior under strain in 3D cultures for a deeper understanding of the relation between neurons and astrocytes in a similar environment of the brain.

4.3 Characterization of cellular response following single-cell/Neurite death in neuronal network in vitro

The nervous tissue function depends on the functional connectivity between its component cells. Due to the intercellular communication, injury or death of the cells could be transferred to other connected cells to stimulate a response in the tissue. After a neuronal injury, the fate of the neuronal tissue and disease development can be assigned to the adaptation of cells with time (Miller and Zachary, 2017). Neuronal disconnection is not only limited to accidental head penetrating injuries, but also the technological evolution and nanoscience offer new tools to make nano surgical injuries at a one molecule scale (Leary et al., 2006). The efficient application of nanosurgery in medical practice necessitates the identification of the crucial principles to precisely evaluate the physiological consequences. Despite the wide advantages of neuro-surgery procedure at single cell level, which provides minimal structural change and fast clinical recovery in a pathological tissue (Chang et al., 2010), it is still necessary to overcome several challenges to understand its physiological consequences. A pervious study showed that the insertion of a micropipette tip to primary astrocytes cultures is enough to cause a circular intercellular calcium wave that spreads well away from the initial area of contact (Murphy et al., 1993). However, there is a lack in studies exploring how small and randomly placed nano-interruption to a living neuronal circuit could alter the short and long term activity of the network. Hence, studying the response of connected neuronal cells to cell death or a disconnection in nervous tissues is necessary to be aware of the pathophysiology of brain injury. The outcomes from this research work demonstrate the influence of laser-induced single-cell or single-neurite death on surrounding neurons in cultured neuronal network reached from monitoring changes in intracellular Ca^{2+} concentrations ($[Ca^{2+}]i$). The impact of directed ablation of single spot in neuronal networks, associated signals and reaction of nearby cells over time are thoroughly addressed in the following sections.

4.3.1 Neuronal Ca^{2+} propagates to adjacent cells in response to single ablation

The maintenance of Ca^{2+} homeostasis is critical for the nervous system to function properly. Calcium ion is an essential factor for neurotransmission (Berridge, 1998) and plays a major role in different neuronal gene expression (Bading et al., 1993; Finkbeiner and Greenberg, 1998). It is important for activity-dependent synaptic plasticity, and considered to be the cellular associate for memory and learning (Bliss and Collingridge, 1993; Lamont and Weber, 2012). It is well understood that alterations in the intensities of intracellular Ca^{2+} or disrupted signaling could cause several neurodegenerative pathologies such as Huntington's, Parkinson's, Alzheimer's disease (Wojda et al., 2008; Nakamura and Lipton, 2010), epilepsy and migraine (Cain and Snutch, 2011). It is found that calcium influx regulates the transcription of brain-derived neurotrophic factor (BDNF) gene by the path of calcium entry to cell and by the pattern of phosphorylation induced on the transcription factor cAMP-response element binding protein (CREB) (West et al., 2001). Our purpose in this study was to monitor spatial and temporal $[Ca^{2+}]$ changes in a well-established neuronal network response during and following a minimally invasive surgery. Such minimal invasive surgery was experimentally resembled by using a pulsed ablation laser that allowed to set nano-cut precisely within neuronal networks.

This work revealed a distance-dependent increase of Ca^{2+} intensity in neurons nearby the ablation spot over time, showing a flow of Ca^{2+} along the neurons initiated from the ablated point. A gradual recovery of $[Ca^{2+}]i$ was detected in a time range of about 10 minutes post ablation. However, the recovery in the closest cells around the spot of ablation (20 µm away) was in 65% of single neuron-ablated samples but none of the neurite-ablated samples recovered for 15 mins after ablation. Previous studies of uniaxial or biaxial stretching of cultured neurons revealed that a rise in $[Ca^{2+}]i$ is observed in regions of unstretched neurons (Lusardi et al., 2004; Choo et al., 2013). This propagated signal shows a transmission of the signal to the surrounding cells. The amplification of $[Ca^{2+}]i$ in surrounding neurons can be explained by the intracellular regulation of calcium ion by various regulatory mechanisms. The level of extracellular glutamate increase dramatically after brain injury (Faden et al., 1989; Katayama et al., 1990; Palmer et al., 1994), which stimulates a selection of receptors on neurons and the Ca^{2+}-permeable ion channels are one of them. Depolarization and K+ efflux after injury activates the release of excitatory amino acid which triggers NMDA receptors (Katayama et al., 1990) to form a pore where Ca^{2+} can pass in the cell. Moreover, stimulation of voltage-gated calcium channels (VGCCs) or leakage from broken cell membranes, can cause a huge rise of calcium in cells following injury (Young, 1992). The long-term elevation in intracellular calcium concentration and extracellular leakage of solutions can activate a cascade of events leading to local inflammation and secondary neuronal damage and eventually to cell death (Trump and Berezesky, 1995; Wojda et al., 2008; Lau and Tymianski, 2010). The recovery of calcium intensity could be explained by $[Ca^{2+}]i$ lowering mechanisms including balanced systems of Ca^{2+} extrusion through plasma membrane pumps including the plasma membrane Ca^{2+}-ATPase (PMCA) and Na^{+}/Ca^{2+} exchangers (Garcia and Strehler, 1999; Brittain et al., 2012). In addition, elevated Ca^{2+} could be buffered by cytoplasmic Ca^{2+} binding proteins such as calbindin and parvalbumin, to be then uptaken and stored by several intracellular organelles as the endoplasmic reticulum (Baimbridge et al., 1992).

4.3.2 Neuronal network overall connectivity is stable after cell/neurite removal

Combining the procedure of single spot ablation with long-term functional imaging in a single-cell microscopic resolution allowed us to assess the global activity and connectivity of the network, with its mean firing rate. The increased intercellular Ca^{2+} temporarily disturbed the rhythmic firing behavior of the nearby cells. However, we observed an overall stable network activity in terms of network burst synchrony and frequency to 24 hours after the single ablation. Therefore, we could speculate that exposing a neuronal population to a minimal change did not cause any instability in the functional signal fluctuation of the network but only immediate distractions to the local network activity and functional connectivity. Other in vitro studies confirm that neurons drop a significant amount of connectivity instantly after an injury (Patel et al., 2012). Molecular studies of the brain after traumatic injury suggest that synaptogenesis occurs, causing an increase in neuron Ca^{+2} activity (Hall and Lifshitz, 2010). The possibility of localized effect is most probably to happen in cortical areas, because local communities of neurons are physically adjacent to each other. However, a challenging experiment could be tested on distant brain areas, communicating through the white matter tracts or on peripheral nervous system in vivo.

Loss of synapsis formation is an early stage in the pathogenesis of Alzheimer's disease that is related to cognitive decline (Scheff and Price, 2003; Scheff et al., 2007). For a closer look to investigate the molecular level of synaptic connectivity, synapses visualization and counting were performed by labeling synapse-specific constituents in pre- and postsynaptic compartments (Biederer and Scheiffele, 2007). A dual labeling approach is ideal, in which the overlap of a pre- and postsynaptic marker is a more reliable display for accurate synapse density. Synaptophysin, is existing on almost all presynaptic vesicles, and is significant for regulating the kinetics of synaptic vesicle endocytosis (Kwon and Chapman, 2011). PSD-95, a main scaffold protein in excitatory synapses, represents synaptic efficacy and spine size in post synaptic compartments (Cane et al., 2014). No changes were observed in key synaptic proteins upon ablation. Despite the lower colocalization of pre- and post-synaptic markers in the closest cells around the ablation spot, change in synapsis formation was not significant enough to argue for potential effects that could cause a pathology in vivo. In our experiments we selected the ablated points randomly, but the effect of ablation is also cell-type and location dependent. Disruption of a neuron in a functional hub can impact the complete network dynamics because this type of neurons are responsible to maintain synchrony (Bonifazi et al., 2009). It is possible to target the impact of ablating high functionally connected cells by using transgenic mice that express a red fluorescent protein on particular neuronal subpopulations such as GABAergic cells (Bonifazi et al., 2009).

4.3.3 Cytoskeletal stabilization to minimal neuronal dissection

The cytoskeletal proteins are important to develop and maintain the function of the nervous system by transmitting chemical and electrical signals between neurons. Numerous neurodegenerative pathologies encompass the disturbance of cytoskeletal proteins expression, dynamics and stability. Actin and tubulin networks are two of the most abundant components of neuronal structure. These structures are crucial during the development and for the procedure of regeneration of axons after injury (Blanquie and Bradke, 2018). High levels of actin and tubulin at the injury site are necessary for the transport of injury signals such as membrane depolarization, mRNA translation, cytokine-mediated STAT3 activation (Abe and Cavalli, 2008) and pro-regenerative program activation (Song et al., 2015).

High concentrations of calcium can stimulate enzymes as calpain and calcineurin, which can stop neuronal Ca^{+2} efflux and degradate axonal cytoskeletal proteins (Johnson et al., 2012). Here, we checked for changes in the expression of cytoskeletal proteins in and around a nano-cut in neuronal network to assess cellular survival and regeneration capability. Upon ablation of subcellular compartment within the neuronal network, there was no remarkable change in structural compartments intensities in the area surrounding the ablation point up to 24 hours after ablation.

In summary, the laser ablation method permits to selectively disturb subcellular compartments of neurons in culture in a highly reproducible way. The long-term imaging of neurons activity, revealed that the network reaction is distance-dependent and recovery is time-dependent. The molecular level reaction was limited and had an insufficient amount.

5 **Conclusion**

Over the past years, public awareness was raised towards the consequences of traumatic brain injury and concussion. The scope of this thesis was focusing on understanding how the function of neurons respond to slight repetitive forces, severe rapid insults and cell death. By combining in vitro deformation models together with recently developed optical and computational technologies, it allowed examining the effect of a wide range of mechanical deformations on recorded network activity and analysis of integrated cellular function. This research work revealed diverse mechanoresponsive reactions for different straining modes, which was discussed based on intracellular calcium influx and adaptability.

Our in vitro examinations revealed that cyclic stretch is functionally tolerable in neurons at different developmental stages. Remarkably, neuronal networks connectivity is very strong against a variety of moderate mechanical strains and can adapt to long-term cyclic deformations. Additionally, severe deformation can cause immediate but temporary disconnections without signs of apoptosis or inflammation. Neuronal networks can restore their connectivity within a short period of time. This work highlighted the difference between physiological motion and stretch-induced injury in terms of threshold parameters and functional response. Generally, the amplitude and type of mechanical insult applied on the neurons would change the severity of the neuronal response to injury. While it is challenging to maintain a sensitive cell type as neurons in culture for a long time, monitoring cellular mechanoresponse after a longer time is needed.

Furthermore, this work pointed out that the presence of astrocytes in culture can improve low-density neurons communication, however, without a major effect on the mechanoresponse of neuron networks to injury. The role of other neural cells in response to a mechanical stimulus need to be widely investigated to understand cell-type-specific differences.

Our work also characterized the influence of a neuronal-compartment death on connected cells in a network based on intracellular Ca^{2+} concentrations. Destabilizing an active neuronal network by single-cell disconnection caused an amplified calcium intensity which temporarily affected the activity and synchrony of surrounding neurons. The connectivity of neighboring cells recovered along with declining calcium intensity within few minutes, proposing an adaptation behavior of neurons to minimal surgery disconnection. Moreover, the recovery is time and cell-component dependent. Additional studies should aim to study the molecular pathways regulating mechanotransduction and adaptation processes in order to expand the knowledge of mechanical biology of cells in the CNS.

However, it is important to note that in vitro models drastically decrease the complexity of 3D environment of the brain into a simple monolayer of cells. Experimental monocultures ignore all the other different types of cells and their secretions in surrounding area that modulate both physiologic and pathologic neuronal processes. Complete understanding of the CNS remain one of the main challenges in medicine. We highlight the significance of considering both the mechanical and electrochemical activity in neurons and the need for further studies on this complex topic.

6 **References**

Abagnale, G., Steger, M., Nguyen, V. H., Hersch, N., Sechi, A., Joussen, S., Denecke, B., Merkel, R., Hoffmann, B., Dreser, A., Schnakenberg, U., Gillner, A., & Wagner, W. (2015). Surface topography enhances differentiation of mesenchymal stem cells towards osteogenic and adipogenic lineages. Biomaterials, 61, 316–326. https://doi.org/10.1016/j.biomaterials.2015.05.030

Abe, N., & Cavalli, V. (2008). Nerve injury signaling. Current opinion in neurobiology, 18(3), 276–283. https://doi.org/10.1016/j.conb.2008.06.005

Abraham, J. A., Linnartz, C., Dreissen, G., Springer, R., Blaschke, S., Rueger, M. A., Fink, G. R., Hoffmann, B., & Merkel, R. (2019). Directing Neuronal Outgrowth and Network Formation of Rat Cortical Neurons by Cyclic Substrate Stretch. Langmuir: the ACS journal of surfaces and colloids, 35(23), 7423–7431. https://doi.org/10.1021/acs.langmuir.8b02003

Adams, K. L., & Gallo, V. (2018). The diversity and disparity of the glial scar. Nature neuroscience, 21(1), 9–15. https://doi.org/10.1038/s41593-017-0033-9

Aebersold, M. J., Thompson-Steckel, G., Joutang, A., Schneider, M., Burchert, C., Forró, C., Weydert, S., Han, H., & Vörös, J. (2018). Simple and Inexpensive Paper-Based Astrocyte Co-culture to Improve Survival of Low-Density Neuronal Networks. Frontiers in neuroscience, 12, 94. https://doi.org/10.3389/fnins.2018.00094

Alexander M. P. (1995). Mild traumatic brain injury: pathophysiology, natural history, and clinical management. Neurology, 45(7), 1253–1260. https://doi.org/10.1212/wnl.45.7.1253

Allen N. J. (2014). Astrocyte regulation of synaptic behavior. Annual review of cell and developmental biology, 30, 439–463. https://doi.org/10.1146/annurev-cellbio-100913-013053

Allen, N. J., & Eroglu, C. (2017). Cell Biology of Astrocyte-Synapse Interactions. Neuron, 96(3), 697–708. https://doi.org/10.1016/j.neuron.2017.09.056

Araque, A., & Navarrete, M. (2010). Glial cells in neuronal network function. Philosophical transactions of the Royal Society of London. Series B, Biological sciences, 365(1551), 2375–2381. https://doi.org/10.1098/rstb.2009.0313

Araque, A., Carmignoto, G., Haydon, P. G., Oliet, S. H., Robitaille, R., & Volterra, A. (2014). Gliotransmitters travel in time and space. Neuron, 81(4), 728–739. https://doi.org/10.1016/j.neuron.2014.02.007

Bading, H., Ginty, D. D., & Greenberg, M. E. (1993). Regulation of gene expression in hippocampal neurons by distinct calcium signaling pathways. Science (New York, N.Y.), 260(5105), 181–186. https://doi.org/10.1126/science.8097060

Baek, J., Cho, S. Y., Kang, H., Ahn, H., Jung, W. B., Cho, Y., Lee, E., Cho, S. W., Jung, H. T., & Im, S. G. (2018). Distinct Mechanosensing of Human Neural Stem Cells on Extremely Limited Anisotropic Cellular Contact. ACS applied materials & interfaces, 10(40), 33891–33900. https://doi.org/10.1021/acsami.8b10171

Bagur, R., & Hajnóczky, G. (2017). Intracellular Ca^{2+} Sensing: Its Role in Calcium Homeostasis and Signaling. Molecular cell, 66(6), 780–788. https://doi.org/10.1016/j.molcel.2017.05.028

Baimbridge, K. G., Celio, M. R., & Rogers, J. H. (1992). Calcium-binding proteins in the nervous system. Trends in neurosciences, 15(8), 303–308. https://doi.org/10.1016/0166-2236(92)90081-i

Bain, A. C., & Meaney, D. F. (2000). Tissue-level thresholds for axonal damage in an experimental model of central nervous system white matter injury. Journal of biomechanical engineering, 122(6), 615–622. https://doi.org/10.1115/1.1324667

Balgude, A. P., Yu, X., Szymanski, A., & Bellamkonda, R. V. (2001). Agarose gel stiffness determines rate of DRG neurite extension in 3D cultures. Biomaterials, 22(10), 1077–1084. https://doi.org/10.1016/s0142-9612(00)00350-1

Bayly, P. V., Cohen, T. S., Leister, E. P., Ajo, D., Leuthardt, E. C., & Genin, G. M. (2005). Deformation of the human brain induced by mild acceleration. Journal of neurotrauma, 22(8), 845–856. https://doi.org/10.1089/neu.2005.22.845

Berridge M. J. (1998). Neuronal calcium signaling. Neuron, 21(1), 13–26. https://doi.org/10.1016/s0896-6273(00)80510-3

Berridge, M. J., Lipp, P., & Bootman, M. D. (2000). The versatility and universality of calcium signalling. Nature reviews. Molecular cell biology, 1(1), 11–21. https://doi.org/10.1038/35036035

Biederer, T., & Scheiffele, P. (2007). Mixed-culture assays for analyzing neuronal synapse formation. Nature protocols, 2(3), 670–676. https://doi.org/10.1038/nprot.2007.92

Blanquie, O., & Bradke, F. (2018). Cytoskeleton dynamics in axon regeneration. Current opinion in neurobiology, 51, 60–69. https://doi.org/10.1016/j.conb.2018.02.024

Blaschke, S., Vay, S. U., Pallast, N., Rabenstein, M., Abraham, J. A., Linnartz, C., Hoffmann, M., Hersch, N., Merkel, R., Hoffmann, B., Fink, G. R., & Rueger, M. A. (2019). Substrate elasticity induces quiescence and promotes neurogenesis of primary neural stem cells-A biophysical in vitro model of the physiological cerebral milieu. Journal of tissue engineering and regenerative medicine, 13(6), 960–972. https://doi.org/10.1002/term.2838

Blennow, K., Hardy, J., & Zetterberg, H. (2012). The neuropathology and neurobiology of traumatic brain injury. Neuron, 76(5), 886–899. https://doi.org/10.1016/j.neuron.2012.11.021

Bliss, T. V., & Collingridge, G. L. (1993). A synaptic model of memory: long-term potentiation in the hippocampus. Nature, 361(6407), 31–39. https://doi.org/10.1038/361031a0

Boelens, H. F., Eilers, P. H., & Hankemeier, T. (2005). Sign constraints improve the detection of differences between complex spectral data sets: LC− IR as an example. Analytical chemistry, 77(24), 7998-8007.

Bonifazi, P., Goldin, M., Picardo, M. A., Jorquera, I., Cattani, A., Bianconi, G., Represa, A., Ben-Ari, Y., & Cossart, R. (2009). GABAergic hub neurons orchestrate synchrony in developing hippocampal networks. Science (New York, N.Y.), 326(5958), 1419–1424. https://doi.org/10.1126/science.1175509

Brittain, M. K., Brustovetsky, T., Sheets, P. L., Brittain, J. M., Khanna, R., Cummins, T. R., & Brustovetsky, N. (2012). Delayed calcium dysregulation in neurons requires both the NMDA receptor and the reverse Na+/Ca2+ exchanger. Neurobiology of disease, 46(1), 109–117. https://doi.org/10.1016/j.nbd.2011.12.051

Bullock, R., Maxwell, W. L., Graham, D. I., Teasdale, G. M., & Adams, J. H. (1991). Glial swelling following human cerebral contusion: an ultrastructural study. Journal of neurology, neurosurgery, and psychiatry, 54(5), 427–434. https://doi.org/10.1136/jnnp.54.5.427

Bureau, I., Shepherd, G. M., & Svoboda, K. (2004). Precise development of functional and anatomical columns in the neocortex. Neuron, 42(5), 789–801. https://doi.org/10.1016/j.neuron.2004.05.002

Bush, T. G., Puvanachandra, N., Horner, C. H., Polito, A., Ostenfeld, T., Svendsen, C. N., Mucke, L., Johnson, M. H., & Sofroniew, M. V. (1999). Leukocyte infiltration, neuronal degeneration, and neurite outgrowth after ablation of scar-forming, reactive astrocytes in adult transgenic mice. Neuron, 23(2), 297–308. https://doi.org/10.1016/s0896-6273(00)80781-3

Cain, S. M., & Snutch, T. P. (2011). Voltage-gated calcium channels and disease. BioFactors (Oxford, England), 37(3), 197–205. https://doi.org/10.1002/biof.158

Cane, M., Maco, B., Knott, G., & Holtmaat, A. (2014). The relationship between PSD-95 clustering and spine stability in vivo. The Journal of neuroscience : the official journal of the Society for Neuroscience, 34(6), 2075–2086. https://doi.org/10.1523/JNEUROSCI.3353-13.2014

Carafoli E. (2002). Calcium signaling: a tale for all seasons. Proceedings of the National Academy of Sciences of the United States of America, 99(3), 1115–1122. https://doi.org/10.1073/pnas.032427999

Carafoli, E., & Krebs, J. (2016). Why Calcium? How Calcium Became the Best Communicator. The Journal of biological chemistry, 291(40), 20849–20857. https://doi.org/10.1074/jbc.R116.735894

Chang, W. C., Hawkes, E., Keller, C. G., & Sretavan, D. W. (2010). Axon repair: surgical application at a subcellular scale. Wiley interdisciplinary reviews. Nanomedicine and nanobiotechnology, 2(2), 151–161. https://doi.org/10.1002/wnan.76

Chen, Y., & Swanson, R. A. (2003). Astrocytes and brain injury. Journal of cerebral blood flow and metabolism : official journal of the International Society of Cerebral Blood Flow and Metabolism, 23(2), 137–149. https://doi.org/10.1097/01.WCB.0000044631.80210.3C

Chesnut, R. M., Marshall, L. F., Klauber, M. R., Blunt, B. A., Baldwin, N., Eisenberg, H. M., Jane, J. A., Marmarou, A., & Foulkes, M. A. (1993). The role of secondary brain injury in determining outcome from severe head injury. The Journal of trauma, 34(2), 216–222. https://doi.org/10.1097/00005373-199302000-00006

Choo, A. M., Miller, W. J., Chen, Y. C., Nibley, P., Patel, T. P., Goletiani, C., Morrison, B., 3rd, Kutzing, M. K., Firestein, B. L., Sul, J. Y., Haydon, P. G., & Meaney, D. F. (2013). Antagonism of purinergic signalling improves recovery from traumatic brain injury. Brain : a journal of neurology, 136(Pt 1), 65–80. https://doi.org/10.1093/brain/aws286

Christopherson, K. S., Ullian, E. M., Stokes, C. C., Mullowney, C. E., Hell, J. W., Agah, A., Lawler, J., Mosher, D. F., Bornstein, P., & Barres, B. A. (2005). Thrombospondins are astrocyte-secreted proteins that promote CNS synaptogenesis. Cell, 120(3), 421–433. https://doi.org/10.1016/j.cell.2004.12.020

Chung, W. S., Allen, N. J., & Eroglu, C. (2015). Astrocytes Control Synapse Formation, Function, and Elimination. Cold Spring Harbor perspectives in biology, 7(9), a020370. https://doi.org/10.1101/cshperspect.a020370

Clarke, L. E., & Barres, B. A. (2013). Emerging roles of astrocytes in neural circuit development. Nature reviews. Neuroscience, 14(5), 311–321. https://doi.org/10.1038/nrn3484

Colón-Ramos D. A. (2009). Synapse formation in developing neural circuits. Current topics in developmental biology, 87, 53–79. https://doi.org/10.1016/S0070-2153(09)01202-2

Cordiglieri, C., & Farina, C. (2010). Astrocytes exert and control immune responses in the brain. Current Immunology Reviews, 6(3), 150-159.

Coutinho, V., & Knöpfel, T. (2002). Metabotropic glutamate receptors: electrical and chemical signaling properties. The Neuroscientist : a review journal bringing neurobiology, neurology and psychiatry, 8(6), 551–561. https://doi.org/10.1177/1073858402238514

Dagg, A.I., & Foster, J.B. (1982). The Giraffe, its biology, behaviour, and ecology. Appendix E Updated Supplementary Material for Reprint Edition. Van Nostrand Reinhold Publishers. U.S.A.

Davalos, D., Grutzendler, J., Yang, G., Kim, J. V., Zuo, Y., Jung, S., Littman, D. R., Dustin, M. L., & Gan, W. B. (2005). ATP mediates rapid microglial response to local brain injury in vivo. Nature neuroscience, 8(6), 752–758. https://doi.org/10.1038/nn1472

De Vincentiis, S., Falconieri, A., Mainardi, M., Cappello, V., Scribano, V., Bizzarri, R., Storti, B., Dente, L., Costa, M., & Raffa, V. (2020). Extremely Low Forces Induce Extreme Axon Growth. The Journal of neuroscience : the official journal of the Society for Neuroscience, 40(26), 4997–5007. https://doi.org/10.1523/JNEUROSCI.3075-19.2020

Dhandapani, S., Manju, D., Sharma, B., & Mahapatra, A. (2012). Prognostic significance of age in traumatic brain injury. Journal of neurosciences in rural practice, 3(2), 131–135. https://doi.org/10.4103/0976-3147.98208

Ding, Z. B., Song, L. J., Wang, Q., Kumar, G., Yan, Y. Q., & Ma, C. G. (2021). Astrocytes: a double-edged sword in neurodegenerative diseases. Neural regeneration research, 16(9), 1702–1710. https://doi.org/10.4103/1673-5374.306064

Drew, P. J., Shih, A. Y., & Kleinfeld, D. (2011). Fluctuating and sensory-induced vasodynamics in rodent cortex extend arteriole capacity. Proceedings of the National Academy of Sciences of the United States of America, 108(20), 8473–8478. https://doi.org/10.1073/pnas.1100428108

Drewes, C., Sagberg, L. M., Jakola, A. S., & Solheim, O. (2018). Perioperative and Postoperative Quality of Life in Patients with Glioma-A Longitudinal Cohort Study. World neurosurgery, 117, e465–e474. https://doi.org/10.1016/j.wneu.2018.06.052

Ehret, F., Vogler, S., & Kempermann, G. (2015). A co-culture model of the hippocampal neurogenic niche reveals differential effects of astrocytes, endothelial cells and pericytes on proliferation and differentiation of adult murine precursor cells. Stem cell research, 15(3), 514–521. https://doi.org/10.1016/j.scr.2015.09.010

Eilers, P. H. (2003). A perfect smoother. Analytical chemistry, 75(14), 3631-3636.

Eilers, P., and Boelens, H. (2005). Baseline correction with asymmetric least squares smoothing. Leiden University Medical Centre Report, 1(1): p. 5.

Engler, A. J., Sen, S., Sweeney, H. L., & Discher, D. E. (2006). Matrix elasticity directs stem cell lineage specification. Cell, 126(4), 677–689. https://doi.org/10.1016/j.cell.2006.06.044

Estrada, J. B., Cramer III, H. C., Scimone, M. T., Buyukozturk, S., & Franck, C. (2021). Neural cell injury pathology due to high-rate mechanical loading. Brain Multiphysics, 2, 100034.

Faden, A. I., Demediuk, P., Panter, S. S., & Vink, R. (1989). The role of excitatory amino acids and NMDA receptors in traumatic brain injury. Science (New York, N.Y.), 244(4906), 798–800. https://doi.org/10.1126/science.2567056

Farhy-Tselnicker, I., & Allen, N. J. (2018). Astrocytes, neurons, synapses: a tripartite view on cortical circuit development. Neural development, 13(1), 7. https://doi.org/10.1186/s13064-018-0104-y

Faust, U., Hampe, N., Rubner, W., Kirchgessner, N., Safran, S., Hoffmann, B., & Merkel, R. (2011). Cyclic stress at mHz frequencies aligns fibroblasts in direction of zero strain. PloS one, 6(12), e28963.

Fields, R. D., & Stevens-Graham, B. (2002). New insights into neuron-glia communication. Science (New York, N.Y.), 298(5593), 556–562. https://doi.org/10.1126/science.298.5593.556

Finkbeiner, S., & Greenberg, M. E. (1998). Ca^{2+} channel-regulated neuronal gene expression. Journal of neurobiology, 37(1), 171–189.

Fleming, S., Thompson, M., Stevens, R., Heneghan, C., Plüddemann, A., Maconochie, I., Tarassenko, L., & Mant, D. (2011). Normal ranges of heart rate and respiratory rate in children from birth to 18 years of age: a systematic review of observational studies. Lancet (London, England), 377(9770), 1011–1018. https://doi.org/10.1016/S0140-6736(10)62226-X

Franze, K., & Guck, J. (2010). The biophysics of neuronal growth. Reports on Progress in Physics, 73(9), 094601.

Franze, K., Janmey, P. A., & Guck, J. (2013). Mechanics in neuronal development and repair. Annual review of biomedical engineering, 15, 227–251. https://doi.org/10.1146/annurev-bioeng-071811-150045

Frugier, T., Morganti-Kossmann, M. C., O'Reilly, D., & McLean, C. A. (2010). In situ detection of inflammatory mediators in post mortem human brain tissue after traumatic injury. Journal of neurotrauma, 27(3), 497–507. https://doi.org/10.1089/neu.2009.1120

Gamburg, E. S., Regine, W. F., Patchell, R. A., Strottmann, J. M., Mohiuddin, M., & Young, A. B. (2000). The prognostic significance of midline shift at presentation on survival in patients with glioblastoma multiforme. International journal of radiation oncology, biology, physics, 48(5), 1359–1362. https://doi.org/10.1016/s0360-3016(00)01410-3

Garcia, M. L., & Strehler, E. E. (1999). Plasma membrane calcium ATPases as critical regulators of calcium homeostasis during neuronal cell function. Frontiers in bioscience : a journal and virtual library, 4, D869–D882. https://doi.org/10.2741/garcia

Georges, P. C., & Janmey, P. A. (2005). Cell type-specific response to growth on soft materials. Journal of applied physiology (Bethesda, Md. : 1985), 98(4), 1547–1553. https://doi.org/10.1152/japplphysiol.01121.2004

Gopcevic, A., Mazul-Sunko, B., Marout, J., Sekulic, A., Antoljak, N., Siranovic, M., Ivanec, Z., Margaritoni, M., Bekavac-Beslin, M., & Zarkovic, N. (2007). Plasma interleukin-8 as a potential predictor of mortality in adult patients with severe traumatic brain injury. The Tohoku journal of experimental medicine, 211(4), 387–393. https://doi.org/10.1620/tjem.211.387

Grienberger, C., & Konnerth, A. (2012). Imaging calcium in neurons. Neuron, 73(5), 862–885. https://doi.org/10.1016/j.neuron.2012.02.011

Hall, K. D., & Lifshitz, J. (2010). Diffuse traumatic brain injury initially attenuates and later expands activation of the rat somatosensory whisker circuit concomitant with neuroplastic responses. Brain research, 1323, 161–173. https://doi.org/10.1016/j.brainres.2010.01.067

Hayakawa, K., Sato, N., & Obinata, T. (2001). Dynamic reorientation of cultured cells and stress fibers under mechanical stress from periodic stretching. Experimental cell research, 268(1), 104-114.

Herculano-Houzel S. (2009). The human brain in numbers: a linearly scaled-up primate brain. Frontiers in human neuroscience, 3, 31. https://doi.org/10.3389/neuro.09.031.2009

Herculano-Houzel S. (2014). The glia/neuron ratio: how it varies uniformly across brain structures and species and what that means for brain physiology and evolution. Glia, 62(9), 1377–1391. https://doi.org/10.1002/glia.22683

Hersch, N., Wolters, B., Ungvari, Z., Gautam, T., Deshpande, D., Merkel, R., Csiszar, A., Hoffmann, B., & Csiszár, A. (2016). Biotin-conjugated fusogenic liposomes for high-quality cell purification. Journal of biomaterials applications, 30(6), 846–856. https://doi.org/10.1177/0885328215603026

Huang, C., Miyazaki, K., Akaishi, S., Watanabe, A., Hyakusoku, H., & Ogawa, R. (2013). Biological effects of cellular stretch on human dermal fibroblasts. Journal of plastic, reconstructive & aesthetic surgery : JPRAS, 66(12), e351–e361. https://doi.org/10.1016/j.bjps.2013.08.002

Iadecola, C., & Nedergaard, M. (2007). Glial regulation of the cerebral microvasculature. Nature neuroscience, 10(11), 1369–1376. https://doi.org/10.1038/nn2003

Jiang, F. X., Yurke, B., Firestein, B. L., & Langrana, N. A. (2008). Neurite outgrowth on a DNA crosslinked hydrogel with tunable stiffnesses. Annals of biomedical engineering, 36(9), 1565–1579. https://doi.org/10.1007/s10439-008-9530-z

Johnson, M. R., Higgins, J. A., Norman, K. A., Sederberg, P. B., Smith, T. A., & Johnson, M. K. (2013). Foraging for thought: an inhibition-of-return-like effect resulting from directing attention within working memory. Psychological science, 24(7), 1104–1112. https://doi.org/10.1177/0956797612466414

Johnson, V. E., Stewart, W., & Smith, D. H. (2013). Axonal pathology in traumatic brain injury. Experimental neurology, 246, 35–43. https://doi.org/10.1016/j.expneurol.2012.01.013

Kampanis, V., Tolou-Dabbaghian, B., Zhou, L., Roth, W., & Puttagunta, R. (2020). Cyclic Stretch of Either PNS or CNS Located Nerves Can Stimulate Neurite Outgrowth. Cells, 10(1), 32. https://doi.org/10.3390/cells10010032

Kanitz, A., Kalus, M. R., Gurevich, E. L., Ostendorf, A., Barcikowski, S., & Amans, D. (2019). Review on experimental and theoretical investigations of the early stage, femtoseconds to microseconds processes during laser ablation in liquid-phase for the synthesis of colloidal nanoparticles. Plasma Sources Science and Technology, 28(10), 103001. doi:10.1088/1361-6595/ab3dbe

Katayama, Y., Becker, D. P., Tamura, T., & Hovda, D. A. (1990). Massive increases in extracellular potassium and the indiscriminate release of glutamate following concussive brain injury. Journal of neurosurgery, 73(6), 889–900. https://doi.org/10.3171/jns.1990.73.6.0889

Khakh, B. S., & Sofroniew, M. V. (2015). Diversity of astrocyte functions and phenotypes in neural circuits. Nature neuroscience, 18(7), 942–952. https://doi.org/10.1038/nn.4043

Kidambi, S., Lee, I., & Chan, C. (2008). Primary Neuron/Astrocyte Co-Culture on Polyelectrolyte Multilayer Films: A Template for Studying Astrocyte-Mediated Oxidative Stress in Neurons. Advanced functional materials, 18(2), 294–301. https://doi.org/10.1002/adfm.200601237

Klionsky, D. J. (2007). Autophagy: from phenomenology to molecular understanding in less than a decade. Nature reviews Molecular cell biology, 8(11), 931-937.

Kolodkin, A. L., & Tessier-Lavigne, M. (2011). Mechanisms and molecules of neuronal wiring: a primer. Cold Spring Harbor perspectives in biology, 3(6), a001727. https://doi.org/10.1101/cshperspect.a001727

Kunze, A., Lengacher, S., Dirren, E., Aebischer, P., Magistretti, P. J., & Renaud, P. (2013). Astrocyte-neuron co-culture on microchips based on the model of SOD mutation to mimic ALS. Integrative biology : quantitative biosciences from nano to macro, 5(7), 964–975. https://doi.org/10.1039/c3ib40022k

Kwon, S. E., & Chapman, E. R. (2011). Synaptophysin regulates the kinetics of synaptic vesicle endocytosis in central neurons. Neuron, 70(5), 847–854. https://doi.org/10.1016/j.neuron.2011.04.001

Kwong, M. T., Bianchi, F., Malboubi, M., García-Grajales, J. A., Homsi, L., Thompson, M., ... & Jérusalem, A. (2019). 3D finite element formulation for mechanical–electrophysiological coupling in axonopathy. Computer Methods in Applied Mechanics and Engineering, 346, 1025-1050.

Lamont, M. G., & Weber, J. T. (2012). The role of calcium in synaptic plasticity and motor learning in the cerebellar cortex. Neuroscience and biobehavioral reviews, 36(4), 1153–1162. https://doi.org/10.1016/j.neubiorev.2012.01.005

Lamoureux, P., Ruthel, G., Buxbaum, R. E., & Heidemann, S. R. (2002). Mechanical tension can specify axonal fate in hippocampal neurons. The Journal of cell biology, 159(3), 499–508. https://doi.org/10.1083/jcb.200207174

Lau, A., & Tymianski, M. (2010). Glutamate receptors, neurotoxicity and neurodegeneration. Pflugers Archiv : European journal of physiology, 460(2), 525–542. https://doi.org/10.1007/s00424-010-0809-1

Leary, S. P., Liu, C. Y., & Apuzzo, M. L. (2006). Toward the emergence of nanoneurosurgery: part III--nanomedicine: targeted nanotherapy, nanosurgery, and progress toward the realization of nanoneurosurgery. Neurosurgery, 58(6), 1009–1026. https://doi.org/10.1227/01.NEU.0000217016.79256.16

Li, B., Cao, Y. P., Feng, X. Q., & Gao, H. (2012). Mechanics of morphological instabilities and surface wrinkling in soft materials: a review. Soft Matter, 8(21), 5728-5745.

Liddelow, S. A., & Barres, B. A. (2017). Reactive Astrocytes: Production, Function, and Therapeutic Potential. Immunity, 46(6), 957–967. https://doi.org/10.1016/j.immuni.2017.06.006

Lin, J., Li, X., Yin, J., & Qian, J. (2020). Effect of cyclic stretch on neuron reorientation and axon outgrowth. Frontiers in Bioengineering and Biotechnology, 8, 597867.

Lo, C. M., Wang, H. B., Dembo, M., & Wang, Y. L. (2000). Cell movement is guided by the rigidity of the substrate. Biophysical journal, 79(1), 144–152. https://doi.org/10.1016/S0006-3495(00)76279-5

Loverde, J. R., & Pfister, B. J. (2015). Developmental axon stretch stimulates neuron growth while maintaining normal electrical activity, intracellular calcium flux, and somatic morphology. Frontiers in cellular neuroscience, 9, 308. https://doi.org/10.3389/fncel.2015.00308

Lu, W., Albalawi, F., Beckel, J. M., Lim, J. C., Laties, A. M., & Mitchell, C. H. (2017). The P2X7 receptor links mechanical strain to cytokine IL-6 up-regulation and release in neurons and astrocytes. Journal of neurochemistry, 141(3), 436–448. https://doi.org/10.1111/jnc.13998

Lu, Y. B., Franze, K., Seifert, G., Steinhäuser, C., Kirchhoff, F., Wolburg, H., Guck, J., Janmey, P., Wei, E. Q., Käs, J., & Reichenbach, A. (2006). Viscoelastic properties of individual glial cells and neurons in the CNS. Proceedings of the National Academy of Sciences of the United States of America, 103(47), 17759–17764. https://doi.org/10.1073/pnas.0606150103

Lusardi, T. A., Rangan, J., Sun, D., Smith, D. H., & Meaney, D. F. (2004). A device to study the initiation and propagation of calcium transients in cultured neurons after mechanical stretch. Annals of biomedical engineering, 32(11), 1546–1558. https://doi.org/10.1114/b:abme.0000049038.75368.75

Magou, G. C., Pfister, B. J., & Berlin, J. R. (2015). Effect of acute stretch injury on action potential and network activity of rat neocortical neurons in culture. Brain research, 1624, 525–535. https://doi.org/10.1016/j.brainres.2015.07.056

Maneshi, M. M. , & Hua, S. Z. (2020). Early Cell Response to Mechanical Stimuli during TBI. In (Ed.), Recent Advances in Biomechanics. IntechOpen. https://doi.org/10.5772/intechopen.93295

Maneshi, M. M., Maki, B., Gnanasambandam, R., Belin, S., Popescu, G. K., Sachs, F., & Hua, S. Z. (2017). Mechanical stress activates NMDA receptors in the absence of agonists. Scientific reports, 7, 39610. https://doi.org/10.1038/srep39610

Margulies, S. S., Thibault, L. E., & Gennarelli, T. A. (1990). Physical model simulations of brain injury in the primate. Journal of biomechanics, 23(8), 823–836. https://doi.org/10.1016/0021-9290(90)90029-3

McBeath, R., Pirone, D. M., Nelson, C. M., Bhadriraju, K., & Chen, C. S. (2004). Cell shape, cytoskeletal tension, and RhoA regulate stem cell lineage commitment. Developmental cell, 6(4), 483–495. https://doi.org/10.1016/s1534-5807(04)00075-9

McKee, A. C., Cantu, R. C., Nowinski, C. J., Hedley-Whyte, E. T., Gavett, B. E., Budson, A. E., Santini, V. E., Lee, H. S., Kubilus, C. A., & Stern, R. A. (2009). Chronic traumatic encephalopathy in athletes: progressive tauopathy after repetitive head injury. Journal of neuropathology and experimental neurology, 68(7), 709–735. https://doi.org/10.1097/NEN.0b013e3181a9d503

McKinney, J. S., Willoughby, K. A., Liang, S., & Ellis, E. F. (1996). Stretch-induced injury of cultured neuronal, glial, and endothelial cells. Effect of polyethylene glycol-conjugated superoxide dismutase. Stroke, 27(5), 934–940. https://doi.org/10.1161/01.str.27.5.934

Middleton, J. W., Lim, K., Taylor, L., Soden, R., & Rutkowski, S. (2004). Patterns of morbidity and rehospitalisation following spinal cord injury. Spinal cord, 42(6), 359–367. https://doi.org/10.1038/sj.sc.3101601

Miller, M. A., & Zachary, J. F. (2017). Mechanisms and Morphology of Cellular Injury, Adaptation, and Death. Pathologic Basis of Veterinary Disease, 2–43.e19. https://doi.org/10.1016/B978-0-323-35775-3.00001-1

Molinaro, A. M., Hervey-Jumper, S., Morshed, R. A., Young, J., Han, S. J., Chunduru, P., Zhang, Y., Phillips, J. J., Shai, A., Lafontaine, M., Crane, J., Chandra, A., Flanigan, P., Jahangiri, A., Cioffi, G., Ostrom, Q., Anderson, J. E., Badve, C., Barnholtz-Sloan, J., Sloan, A. E., … Berger, M. S. (2020). Association of Maximal Extent of Resection of Contrast-Enhanced and Non-Contrast-Enhanced Tumor With Survival Within Molecular Subgroups of Patients With Newly Diagnosed Glioblastoma. JAMA oncology, 6(4), 495–503. https://doi.org/10.1001/jamaoncol.2019.6143

Morrison, B., 3rd, Cater, H. L., Benham, C. D., & Sundstrom, L. E. (2006). An in vitro model of traumatic brain injury utilising two-dimensional stretch of organotypic hippocampal slice cultures. Journal of neuroscience methods, 150(2), 192–201. https://doi.org/10.1016

Morsch, M., Radford, R. A., Don, E. K., Lee, A., Hortle, E., Cole, N. J., & Chung, R. S. (2017). Triggering Cell Stress and Death Using Conventional UV Laser Confocal Microscopy. Journal of visualized experiments: JoVE, (120), 54983. https://doi.org/10.3791/54983

Murphy, T. H., Blatter, L. A., Wier, W. G., & Baraban, J. M. (1993). Rapid communication between neurons and astrocytes in primary cortical cultures. The Journal of neuroscience : the official journal of the Society for Neuroscience, 13(6), 2672–2679. https://doi.org/10.1523/JNEUROSCI.13-06-02672.1993

Nakamura, T., & Lipton, S. A. (2010). Preventing Ca^{2+}-mediated nitrosative stress in neurodegenerative diseases: possible pharmacological strategies. Cell calcium, 47(2), 190–197. https://doi.org/10.1016/j.ceca.2009.12.009

Narciso, C., Wu, Q., Brodskiy, P., Garston, G., Baker, R., Fletcher, A., & Zartman, J. (2015). Patterning of wound-induced intercellular Ca(2+) flashes in a developing epithelium. Phys Biol, 12(5), 056005. doi:10.1088/1478-3975/12/5/056005

Niediek, V., Born, S., Hampe, N., Kirchgessner, N., Merkel, R., & Hoffmann, B. (2012). Cyclic stretch induces reorientation of cells in a Src family kinase- and p130Cas-dependent manner. European journal of cell biology, 91(2), 118–128. https://doi.org/10.1016/j.ejcb.2011.10.003

Nimchinsky, E. A., Sabatini, B. L., & Svoboda, K. (2002). Structure and function of dendritic spines. Annual review of physiology, 64, 313–353. https://doi.org/10.1146/annurev.physiol.64.081501.160008

Nimmerjahn, A., Kirchhoff, F., Kerr, J. N., & Helmchen, F. (2004). Sulforhodamine 101 as a specific marker of astroglia in the neocortex in vivo. Nature methods, 1(1), 31–37. https://doi.org/10.1038/nmeth706

Noreau, L., Proulx, P., Gagnon, L., Drolet, M., & Laramée, M. T. (2000). Secondary impairments after spinal cord injury: a population-based study. American journal of physical medicine & rehabilitation, 79(6), 526–535. https://doi.org/10.1097/00002060-200011000-00009

Oberheim, N. A., Takano, T., Han, X., He, W., Lin, J. H., Wang, F., Xu, Q., Wyatt, J. D., Pilcher, W., Ojemann, J. G., Ransom, B. R., Goldman, S. A., & Nedergaard, M. (2009). Uniquely hominid features of adult human astrocytes. The Journal of neuroscience : the official journal of the Society for Neuroscience, 29(10), 3276–3287. https://doi.org/10.1523/JNEUROSCI.4707-08.2009

Orrenius, S., Zhivotovsky, B., & Nicotera, P. (2003). Regulation of cell death: the calcium-apoptosis link. Nature reviews. Molecular cell biology, 4(7), 552–565. https://doi.org/10.1038/nrm1150

Palmer, A. M., Marion, D. W., Botscheller, M. L., Bowen, D. M., & DeKosky, S. T. (1994). Increased transmitter amino acid concentration in human ventricular CSF after brain trauma. Neuroreport, 6(1), 153–156. https://doi.org/10.1097/00001756-199412300-00039

Pannasch, U., & Rouach, N. (2013). Emerging role for astroglial networks in information processing: from synapse to behavior. Trends in neurosciences, 36(7), 405–417. https://doi.org/10.1016/j.tins.2013.04.004

Park, L. C., Zhang, H., & Gibson, G. E. (2001). Co-culture with astrocytes or microglia protects metabolically impaired neurons. Mechanisms of ageing and development, 123(1), 21–27. https://doi.org/10.1016/s0047-6374(01)00336-0

Patel, T. P., Ventre, S. C., & Meaney, D. F. (2012). Dynamic changes in neural circuit topology following mild mechanical injury in vitro. Annals of biomedical engineering, 40(1), 23–36. https://doi.org/10.1007/s10439-011-0390-6

Pelham, R. J., Jr, & Wang, Y. l. (1997). Cell locomotion and focal adhesions are regulated by substrate flexibility. Proceedings of the National Academy of Sciences of the United States of America, 94(25), 13661–13665. https://doi.org/10.1073/pnas.94.25.13661

Perea, G., Navarrete, M., & Araque, A. (2009). Tripartite synapses: astrocytes process and control synaptic information. Trends in neurosciences, 32(8), 421–431. https://doi.org/10.1016/j.tins.2009.05.001

Perez-Barcena, J., Ibáñez, J., Brell, M., Crespí, C., Frontera, G., Llompart-Pou, J. A., Homar, J., & Abadal, J. M. (2011). Lack of correlation among intracerebral cytokines, intracranial pressure, and brain tissue oxygenation in patients with traumatic brain injury and diffuse lesions. Critical care medicine, 39(3), 533–540. https://doi.org/10.1097/CCM.0b013e318205c7a4

Pettus, E. H., Christman, C. W., Giebel, M. L., & Povlishock, J. T. (1994). Traumatically induced altered membrane permeability: its relationship to traumatically induced reactive axonal change. Journal of neurotrauma, 11(5), 507–522. https://doi.org/10.1089/neu.1994.11.507

Petzold, J., & Gentleman, E. (2021). Intrinsic Mechanical Cues and Their Impact on Stem Cells and Embryogenesis. Frontiers in cell and developmental biology, 9, 761871. https://doi.org/10.3389/fcell.2021.761871

Pfister, B. J., Iwata, A., Meaney, D. F., & Smith, D. H. (2004). Extreme stretch growth of integrated axons. The Journal of neuroscience : the official journal of the Society for Neuroscience, 24(36), 7978–7983. https://doi.org/10.1523/JNEUROSCI.1974-04.2004

Pivovarova, N. B., & Andrews, S. B. (2010). Calcium-dependent mitochondrial function and dysfunction in neurons. The FEBS journal, 277(18), 3622–3636. https://doi.org/10.1111/j.1742-4658.2010.07754.x

Potokar, M., Kreft, M., Li, L., Daniel Andersson, J., Pangrsic, T., Chowdhury, H. H., Pekny, M., & Zorec, R. (2007). Cytoskeleton and vesicle mobility in astrocytes. Traffic (Copenhagen, Denmark), 8(1), 12–20. https://doi.org/10.1111/j.1600-0854.2006.00509.x

Prado, G. R., Ross, J. D., DeWeerth, S. P., & LaPlaca, M. C. (2005). Mechanical trauma induces immediate changes in neuronal network activity. Journal of neural engineering, 2(4), 148–158. https://doi.org/10.1088/1741-2560/2/4/011

Pyka, M., Busse, C., Seidenbecher, C., Gundelfinger, E. D., & Faissner, A. (2011). Astrocytes are crucial for survival and maturation of embryonic hippocampal neurons in a neuron-glia cell-insert coculture assay. Synapse (New York, N.Y.), 65(1), 41–53. https://doi.org/10.1002/syn.20816

Qiu, H., Zhu, Y., Sun, Z., Trzeciakowski, J. P., Gansner, M., Depre, C., Resuello, R. R. G., Natividad, F. F., Hunter, W. C., Genin, G. M., Elson, E. L., Vatner, D. E., Meininger, G. A., & Vatner, S. F. (2010). Short communication: vascular smooth muscle cell stiffness as a mechanism for increased aortic stiffness with aging. Circulation Research, 107(5), 615-619.

Ranade, S. S., Qiu, Z., Woo, S. H., Hur, S. S., Murthy, S. E., Cahalan, S. M., Xu, J., Mathur, J., Bandell, M., Coste, B., Li, Y. S., Chien, S., & Patapoutian, A. (2014). Piezo1, a mechanically activated ion channel, is required for vascular development in mice. Proceedings of the National Academy of Sciences of the United States of America, 111(28), 10347–10352. https://doi.org/10.1073/pnas.1409233111

Rossi, D., & Volterra, A. (2009). Astrocytic dysfunction: insights on the role in neurodegeneration. Brain research bulletin, 80(4-5), 224–232. https://doi.org/10.1016/j.brainresbull.2009.07.012

Rzigalinski, B. A., Weber, J. T., Willoughby, K. A., & Ellis, E. F. (1998). Intracellular free calcium dynamics in stretch-injured astrocytes. Journal of neurochemistry, 70(6), 2377–2385. https://doi.org/10.1046/j.1471-4159.1998.70062377.x

Scheff, S. W., & Price, D. A. (2003). Synaptic pathology in Alzheimer's disease: a review of ultrastructural studies. Neurobiology of aging, 24(8), 1029–1046. https://doi.org/10.1016/j.neurobiolaging.2003.08.002

Scheff, S. W., Price, D. A., Schmitt, F. A., DeKosky, S. T., & Mufson, E. J. (2007). Synaptic alterations in CA1 in mild Alzheimer disease and mild cognitive impairment. Neurology, 68(18), 1501–1508. https://doi.org/10.1212/01.wnl.0000260698.46517.8f

Schutte, R. J., Xie, Y., Ng, N. N., Figueroa, P., Pham, A. T., & O'Dowd, D. K. (2018). Astrocyte-enriched feeder layers from cryopreserved cells support differentiation of spontaneously active networks of human iPSC-derived neurons. Journal of neuroscience methods, 294, 91–101. https://doi.org/10.1016/j.jneumeth.2017.07.019

Shcherbatko, A., Ono, F., Mandel, G., & Brehm, P. (1999). Voltage-dependent sodium channel function is regulated through membrane mechanics. Biophysical journal, 77(4), 1945–1959. https://doi.org/10.1016/S0006-3495(99)77036-0

Shi, R., & Whitebone, J. (2006). Conduction deficits and membrane disruption of spinal cord axons as a function of magnitude and rate of strain. Journal of neurophysiology, 95(6), 3384–3390. https://doi.org/10.1152/jn.00350.2005

Slemmer, J. E., Matser, E. J., De Zeeuw, C. I., & Weber, J. T. (2002). Repeated mild injury causes cumulative damage to hippocampal cells. Brain : a journal of neurology, 125(Pt 12), 2699–2709. https://doi.org/10.1093/brain/awf271

Smith D. H. (2009). Stretch growth of integrated axon tracts: extremes and exploitations. Progress in neurobiology, 89(3), 231–239. https://doi.org/10.1016/j.pneurobio.2009.07.006

Smith, D. H., & Stewart, W. (2020). Genetic interplay with soccer ball heading. Nature reviews. Neurology, 16(4), 189–190. https://doi.org/10.1038/s41582-020-0334-6

Sofroniew, M. V., & Vinters, H. V. (2010). Astrocytes: biology and pathology. Acta neuropathologica, 119(1), 7–35. https://doi.org/10.1007/s00401-009-0619-8

Song, W., Cho, Y., Watt, D., & Cavalli, V. (2015). Tubulin-tyrosine Ligase (TTL)-mediated Increase in Tyrosinated α-Tubulin in Injured Axons Is Required for Retrograde Injury Signaling and Axon Regeneration. The Journal of biological chemistry, 290(23), 14765–14775. https://doi.org/10.1074/jbc.M114.622753

Spooren, A., Kolmus, K., Laureys, G., Clinckers, R., De Keyser, J., Haegeman, G., & Gerlo, S. (2011). Interleukin-6, a mental cytokine. Brain research reviews, 67(1-2), 157–183. https://doi.org/10.1016/j.brainresrev.2011.01.002

Sridhar, K. C. (2021). Characterization of signaling events following single-cell death in myocardial cell clusters in vitro [Doctoral dissertation, Rheinische Friedrich-Wilhelms-Universität Bonn]. https://nbn-resolving.org/urn:nbn:de:hbz:5-62394

Stern, E. A., Maravall, M., & Svoboda, K. (2001). Rapid development and plasticity of layer 2/3 maps in rat barrel cortex in vivo. Neuron, 31(2), 305–315. https://doi.org/10.1016/s0896-6273(01)00360-9

Stys, P. K., & Lopachin, R. M. (1998). Mechanisms of calcium and sodium fluxes in anoxic myelinated central nervous system axons. Neuroscience, 82(1), 21–32. https://doi.org/10.1016/s0306-4522(97)00230-3

Taber, K. H., Warden, D. L., & Hurley, R. A. (2006). Blast-related traumatic brain injury: what is known?. The Journal of neuropsychiatry and clinical neurosciences, 18(2), 141–145. https://doi.org/10.1176/jnp.2006.18.2.141

Tang-Schomer, M. D., Patel, A. R., Baas, P. W., & Smith, D. H. (2010). Mechanical breaking of microtubules in axons during dynamic stretch injury underlies delayed elasticity, microtubule disassembly, and axon degeneration. FASEB journal : official publication of the Federation of American Societies for Experimental Biology, 24(5), 1401–1410. https://doi.org/10.1096/fj.09-142844

Tischbirek, C. H., Birkner, A., & Konnerth, A. (2017). In vivo deep two-photon imaging of neural circuits with the fluorescent Ca^{2+} indicator Cal-590. The Journal of physiology, 595(10), 3097–3105. https://doi.org/10.1113/JP272790

Tischbirek, C., Birkner, A., Jia, H., Sakmann, B., & Konnerth, A. (2015). Deep two-photon brain imaging with a red-shifted fluorometric Ca^{2+} indicator. Proceedings of the National Academy of Sciences, 112(36), 11377-11382.

Tojima, T., Hines, J. H., Henley, J. R., & Kamiguchi, H. (2011). Second messengers and membrane trafficking direct and organize growth cone steering. Nature reviews. Neuroscience, 12(4), 191–203. https://doi.org/10.1038/nrn2996

Travis, Z. D., Sherchan, P., Hayes, W. K., & Zhang, J. H. (2019). Surgically-induced brain injury: where are we now?. Chinese neurosurgical journal, 5, 29. https://doi.org/10.1186/s41016-019-0181-8

Trump, B. F., & Berezesky, I. K. (1995). Calcium-mediated cell injury and cell death. FASEB journal : official publication of the Federation of American Societies for Experimental Biology, 9(2), 219–228. https://doi.org/10.1096/fasebj.9.2.7781924

Van Essen D. C. (1997). A tension-based theory of morphogenesis and compact wiring in the central nervous system. Nature, 385(6614), 313–318. https://doi.org/10.1038/385313a0

Vaskovic, J. (n.d.). Action potential. Kenhub. https://www.kenhub.com/en/library/anatomy/action-potential

Venugopal, B., , Mogha, P., , Dhawan, J., , & Majumder, A., (2018). Cell density overrides the effect of substrate stiffness on human mesenchymal stem cells' morphology and proliferation. Biomaterials science, 6(5), 1109–1119. https://doi.org/10.1039/c7bm00853h

Verstraelen, P., Garcia-Diaz Barriga, G., Verschuuren, M., Asselbergh, B., Nuydens, R., Larsen, P. H., Timmermans, J. P., & De Vos, W. H. (2020). Systematic Quantification of Synapses in Primary Neuronal Culture. iScience, 23(9), 101542. https://doi.org/10.1016/j.isci.2020.101542

Waxweiler, R. J., Thurman, D., Sniezek, J., Sosin, D., & O'Neil, J. (1995). Monitoring the impact of traumatic brain injury: a review and update. Journal of neurotrauma, 12(4), 509–516. https://doi.org/10.1089/neu.1995.12.509

Weber, J. T., Rzigalinski, B. A., & Ellis, E. F. (2001). Traumatic injury of cortical neurons causes changes in intracellular calcium stores and capacitative calcium influx. The Journal of biological chemistry, 276(3), 1800–1807. https://doi.org/10.1074/jbc.M009209200

Wedeen, V. J., & Ponceleti, B. (2007). Brain Parenchyma Motion Observed by MRI. eMagRes. DOI: 10.1002/9780470034590.emrstm0043.

Weiss, P. (1941). Nerve patterns: the mechanisms of nerve growth. Growth, 5, 163-203.

Wen, Q., & Chklovskii, D. B. (2005). Segregation of the brain into gray and white matter: a design minimizing conduction delays. PLoS computational biology, 1(7), e78. https://doi.org/10.1371/journal.pcbi.0010078

West, A. E., Chen, W. G., Dalva, M. B., Dolmetsch, R. E., Kornhauser, J. M., Shaywitz, A. J., Takasu, M. A., Tao, X., & Greenberg, M. E. (2001). Calcium regulation of neuronal gene expression. Proceedings of the National Academy of Sciences of the United States of America, 98(20), 11024–11031. https://doi.org/10.1073/pnas.191352298

Westgren, N., & Levi, R. (1998). Quality of life and traumatic spinal cord injury. Archives of physical medicine and rehabilitation, 79(11), 1433–1439. https://doi.org/10.1016/s0003-9993(98)90240-4

Winer, J. P., Janmey, P. A., McCormick, M. E., & Funaki, M. (2009). Bone marrow-derived human mesenchymal stem cells become quiescent on soft substrates but remain responsive to chemical or mechanical stimuli. Tissue engineering. Part A, 15(1), 147–154. https://doi.org/10.1089/ten.tea.2007.0388

Wise, S. P., Fleshman, J. W., Jr, & Jones, E. G. (1979). Maturation of pyramidal cell form in relation to developing afferent and efferent connections of rat somatic sensory cortex. Neuroscience, 4(9), 1275–1297. https://doi.org/10.1016/0306-4522(79)90157-x

Wojda, U., Salinska, E., & Kuznicki, J. (2008). Calcium ions in neuronal degeneration. IUBMB life, 60(9), 575–590. https://doi.org/10.1002/iub.91

Wolf, J. A., Stys, P. K., Lusardi, T., Meaney, D., & Smith, D. H. (2001). Traumatic axonal injury induces calcium influx modulated by tetrodotoxin-sensitive sodium channels. The Journal of neuroscience : the official journal of the Society for Neuroscience, 21(6), 1923–1930. https://doi.org/10.1523/JNEUROSCI.21-06-01923.2001

Wozniak, M. A., & Chen, C. S. (2009). Mechanotransduction in development: a growing role for contractility. Nature reviews. Molecular cell biology, 10(1), 34–43. https://doi.org/10.1038/nrm2592

Young W. (1992). Role of calcium in central nervous system injuries. Journal of neurotrauma, 9 Suppl 1, S9–S25.

Yue, Z., Friedman, L., Komatsu, M., & Tanaka, K. (2009). The cellular pathways of neuronal autophagy and their implication in neurodegenerative diseases. Biochimica et biophysica acta, 1793(9), 1496–1507. https://doi.org/10.1016/j.bbamcr.2009.01.016

Yuste, R., & Bonhoeffer, T. (2004). Genesis of dendritic spines: insights from ultrastructural and imaging studies. Nature reviews. Neuroscience, 5(1), 24–34. https://doi.org/10.1038/nrn1300

Zhao, X., Ahram, A., Berman, R. F., Muizelaar, J. P., & Lyeth, B. G. (2003). Early loss of astrocytes after experimental traumatic brain injury. Glia, 44(2), 140-152.

Zilles, K., Palomero-Gallagher, N., & Amunts, K. (2013). Development of cortical folding during evolution and ontogeny. Trends in neurosciences, 36(5), 275–284. https://doi.org/10.1016/j.tins.2013.01.006

7 Figures

8 **Acknowledgements**

It would not have been possible to complete my doctoral research work without the support, inspiration and encouragement of many people, whom I want to thank here.

First of all, I am sincerely grateful to my supervisor PD. Dr. Bernd Hoffmann at IBI-2: Mechanobiology at Forschungszentrum Jülich for providing the opportunity to be part of this research project at the IBI-2 research group. His guidance, patience and knowledge helped me during all the time of research and writing of this thesis. I could not have imagined having a better mentor and advisor for my Ph.D study. I would further like to thank Prof. Rudolf Merkel for his support and valuable discussions.

I would like to thank and appreciate the other members of my PhD committee, Prof. Dieter Fürst, Prof. Jörg Höhfeld and Dr. Gerhild van Echten-Deckert for their valuable time to evaluate this thesis work.

I am also deeply thankful to Dr. Feras AL-Batta for recommending and accepting me as his PhD student. And for all the committee of the Palestinian-German Science Bridge (PGSB), the Palestine Academy for Science and Technology (PALAST), Juelich Research Center (FZJ) and the German Federal Ministry of Science and Scientific Research BMBF for funding this project and my position.

Further, I would like to thank Prof. Maria Adele Rüger, Prof. Gereon Fink and their team from the University Hospital in Cologne for providing us with primary astrocytes and for their scientific input and feedback.

Data analysis was challenging during the research and I pay my deepest gratitude to Georg Dreissen, Dr. Ronald Springer and Dr. Hanno Scharr for writing algorithms for image processing and providing programs for data evaluation. A special thanks to Jens Konrad for helping with hardware settings and for his innovative improvements in chambers handling.

I am very thankful to Dr. Jella Abraham, Dr. Guillermo Beltramo and Dr. Krishna Sridhar for scientific discussions which provided me with many useful ideas and for helping me at different points during work at Forschungszentrum Jülich. I would like also to thank Dr. Marco Hoffmann, Lukas Loevenich and Sven Gerlach for collaborating with me and for making this a very pleasant project and to Dr. Erik Noetzel-Reiss for proofreading of the thesis. A special thanks also to Sara Al-sherif and Mahmud Shehab for their friendship which made work and life funnier and easier. And to all the past and present colleagues in IBI-2 who welcomed me and provided an excellent work environment.

Finally, genuine gratitude goes to my family for their faith in me and their continuous emotional and financial support through years of study. I thank my parents, Maher and Mona, my dear siblings and my fiancé for loving me, believing in me and supporting me. I would not have finished this thesis without your endless love and encouragement. I dedicate this work to my proud family especially to my parents. I hope that this achievement will complete the dream that you had for me all those years ago when you chose to provide me with the best education you could.

9 **Publications**

Parts of the dissertation are in progress to be published:

- Tarazi, S., Dreissen, G., Abraham, J., Hoffmann, M., Gerlach, S., Loevenich, L., Springer, R., Scharr, H., Rüger, M., Fink, G., Merkel, R. & Hoffmann, B. Functional resistance of neuronal networks against strain.
- Tarazi, S., Dreissen, G., Sridhar, K. C., Merkel, R. & Hoffmann, B. Calcium mediated functional response between neurons upon minimal laser-induced injury.

Other publication:

- Abraham, J. A., Blaschke, S., Tarazi, S., Dreissen, G., Vay, S. U., Schroeter, M., Fink, G. R., Merkel, R., Rueger, M. A., & Hoffmann, B. (2021). NSCs Under Strain-Unraveling the Mechanoprotective Role of Differentiating Astrocytes in a Cyclically Stretched Coculture With Differentiating Neurons. Frontiers in cellular neuroscience, 15, 706585. https://doi.org/10.3389/fncel.2021.706585